Doctoral Dissertation

# Development of a Monochromator with Offset Cylindrical Lenses for Electron Microscopy

Takashi Ogawa

July 2018

Department of Material and Life Science

Graduate School of Engineering

Osaka University

# Contents

# List of Abbreviations and Parameters

| | |
|---|---|
| ACC | Acceleration |
| AVG | Averaged Value |
| CCD | Charge Coupled Device |
| CFE | Cold Field Emitter |
| CL | Cylindrical Lens |
| CoL | Condenser Lens of SEM |
| CPO | Charged Particle Optics |
| Det | through the Lens Detector of SEM |
| EA | Energy Analyzer |
| EB | Electron Beam |
| EELS | Electron Energy Loss Spectroscopy |
| EM | Electron Microscopy |
| ES-AP | Energy Selection Aperture |
| EXT | Extractor of Emitters |
| FE | Falling Edge, Energy Width for Signals from 25 to 75% on High Energy Side |
| FTIR | Fourier-Transform Infrared Spectroscopy |
| FWHM | Full Width at Half Maximum |
| FW50 | Full Width of Diameter Containing 50% of Beam Current |
| GND | Ground Potential |
| HSA | Hemispherical Energy Analyzers |
| HREELS | High-Resolution Electron Energy Loss Spectroscopy |
| IN-AP | Incident Aperture |
| LEEM | Low Energy Electron Microscopy |
| MC | Monochromator |
| MCP | Micro Channel Plate |
| OL | Objective Lens of SEM |
| PE | Pass Energy |

| | |
|---|---|
| PMMA | Polymethyl Methacrylate |
| RE | Rising Edge, Energy Width for Signals from 25 to 75% on the Low Energy Side |
| RFA | Retarding Field Energy Analyzer |
| Scan | Scanner of SEM |
| SCR | Phosphor Screen |
| SD | Standard Deviations |
| SE | Schottky Emitter |
| SEM | Scanning Electron Microscopy |
| SNOM | Scanning Near-Field Optical Microscopy |
| STEM | Scanning Transmission Electron Microscopy |
| TED | Total Energy Distributions |
| TEM | Transmission Electron Microscopy |
| TL | Transfer Lens |
| UV | Ultraviolet |
| UHV | Ultra High Vacuum |
| XHV | Extremely High Vacuum |
| $B_r$ | Reduced Brightness |
| $d$ | Beam Diameter or Contribution from Aberration |
| $dE$, $\delta E$ | Energy Resolution or Energy Spread |
| $D_\kappa$ | Energy Dispersion |
| $f$ | Focal Length |
| $I$ | Current |
| $M$ | Magnification of Optics |
| $V$ | Voltage |
| $x$, $y$ | Beam Positions |
| $Z$ | Z Coordinate of Optical Plane |
| $\alpha$, $\beta$, $\gamma$, $\delta$ | Beam Angles |

# Preface

This study is related to charged particle optics (CPO), which is a branch of applied physics. The CPO handles beam technologies of electrons, ions, and high-energy particles and provides methodology for controlling these trajectories through electrostatic and magnetic fields in specific distributions. The CPO has a long history and covers a broad range of applications; cathode ray tubes, electron microscopes (EMs), focused ion beam tools, energy or mass spectrometers, ion implanters, electron beam (EB) welders, 3D printers, and particle accelerators. By providing the scientific instruments and production equipment to various academic and industrial fields, the CPO has supported science and technologies and contributed to their progress. Therefore, the CPO is considered one of the most significant and fundamental research fields. This study is a part of the CPO, that is, the EB technology for EMs and spectrometers.

The main subject of this study is development of a new monochromator (MC) for EMs. MCs are components of electron optics, which can generate EBs with narrowed energy spreads. There are two types of EMs; scanning electron microscopy (SEM) and (scanning) transmission electron microscopy ((S)TEM). Recently, both of SEM and TEM have adopted low energy conditions for the operation. However, this causes deterioration of the spatial resolution because of chromatic aberration. To solve this issue, advanced EMs adopt MCs to reduce the influence of the chromatic aberration. MCs are beneficial to achieve high image resolutions of the EMs at the low energy conditions. In addition, MCs are useful to improve energy resolutions of electron energy-loss spectroscopy (EELS). Therefore, MCs have been indispensable optical components for advanced EMs and contributed various research in the field of physics, materials science, biology, and nanoelectronics. After continuous efforts of development in two decades, the latest MCs achieved a very high level of the performance. However, structures for the MC became very complicated. Therefore, in this doctoral dissertation, the author will develop a new MC with high performance and simple structure. The MC adopts novel optics using offset cylindrical lenses (CLs). Considering importance of SEM in industry, the application of the MC to SEM will be mainly discussed. This dissertation will summarize series of research results on theory and design of the MC optics, estimation of SEM performance with the MC, and realization of a prototype and evaluations of its performance in a test bench.

This dissertation consists of six chapters. Each chapter will be briefly summarized as follows:

In chapter1, the background and main subject of this study will be discussed. The recent trends of the EMs and adoption of the MCs will be explained. The technologies of the MC will be described through reviewing previous studies on the MCs. The main theme and objectives of this study will be clarified.

In chapter 2, a new MC with multiple offset CLs will be theoretically constituted. Here, the first-order matrix expressions for the offset CL will be adopted, which are derived from ray trace simulations. For a total optical system of the MC, the beam profiles will be presented on the energy selection plane at the middle and the imaging plane at the exit. The energy resolving performance and the mechanical tolerance of the MC will be estimated.

In chapter 3, aberration coefficients of the MC will be derived up to the third order by applying a regression analysis to trajectories. Based on the aberration coefficients, dependencies of the MC performance such as the beam width, energy resolution, and brightness, on the beam current will be clarified. The MC performance will be estimated for various source conditions, such as types of emitters, extraction voltages, and tip radiuses. These characteristics will be important for the MC and its application to EMs.

In chapter 4, applications of the MC to a low voltage SEM will be theoretically investigated. Assuming the ideal SEM optics with high-performance, beam diameters will be calculated with FW50 methods. The improvement of SEM performance by the adoption of the MC will be estimated. Additionally, the SEM performance will be surveyed under various emitter conditions and the optimum current ranges will be estimated for each source.

In chapter 5, the author will construct a prototype of the MC on a test bench and evaluate the performance. The first half optics, which mainly determines energy resolutions, will be evaluated. The optics includes an offset CL and a collimating transfer lens. The energy resolutions will be estimated by comparing total energy spreads of emitters from experiment and theory. In addition, the accuracy of a total measurement system and the lens conditions of the optics will be evaluated.

In chapter 6, the entire MC optics will be evaluated. The test bench of the prototype of the MC includes an additional energy analyzer in the downside. The performance of the MC will be experimentally evaluated by measuring energy distributions and observing beam profiles. These results will assure that this MC has a high

potential for its application to EMs. Furthermore, future perspectives will be discussed.

In conclusion, this study will be summarized.

# Chapter 1 Monochromators for Electron Microscopes

## 1-1 Introduction

In this chapter, the background and main subject of this study will be discussed. Monochromators (MCs) are components of electron optics, which can generate electron beams (EBs) with reduced energy spreads. A recent trend of electron microscopes (EMs) and adoption of MCs will be discussed. MC technologies will be introduced through reviewing previous studies. The main subject and objectives of this study will be clarified. Finally, the outline of this dissertation will be presented.

## 1-2 Recent trend in electron microscopy

An EM is one of the most commonly used instruments for observation and analysis of various materials and devices. There are two types of EMs; scanning electron microscopy (SEM) and (scanning) transmission electron microscopy ((S)TEM). SEM is used for observation of surfaces of specimens in nanometer scales with relatively low-energy conditions of 1~30 keV [1]. (S)TEM is used for observation of specimens in atomic scales with transmitted electron beams at relatively high-energy conditions of 100~300 keV [2]. Recently, observation in low energy conditions becomes a technical trend for both SEM and TEM.

SEM is utilized for industrial applications and academic research. Especially in the semiconductor industry, automated SEMs for wafers or masks, for example, critical dimension SEM, defect-review SEM, and mask SEM, are frequently used for the in-line process monitoring of device production. Conventional operational energy conditions for these SEMs are 800-1500 eV. The adoption of the conventional conditions enables to avoid charge accumulation on the specimens, which causes crucial damages to the devices. The applications also require robustness and stability of the equipment because a continuous operation with a minimum downtime is required. Recently, advanced devices with 5−10 nm nodes begin to require extremely low energy conditions of several 100 eV. Figure 1-1shows results of Monte Carlo simulations by Bunday et al [3, 4]. The scattering process of EBs was simulated for fin-like Si structures in 10 nm pith and 30 nm height. In a conventional condition of 800 eV, EBs were scattered into a large range of the structures. As the beam energy decreases to 150 eV, the EBs were mainly scattered in the top side of the structures and the interaction volume is sufficiently reduced. This is beneficial to enhance a contrast of SEM images because of reduced background. Detailed simulation results confirmed the advantages of

150 and 300 eV beams in terms of their signal sensitivity on the top sides of the Si structures. Progress in the design rules of the semiconductor devices keeps the demands for improvement in SEM instruments. Therefore, operation at extremely low energy conditions becomes essential for the SEM.

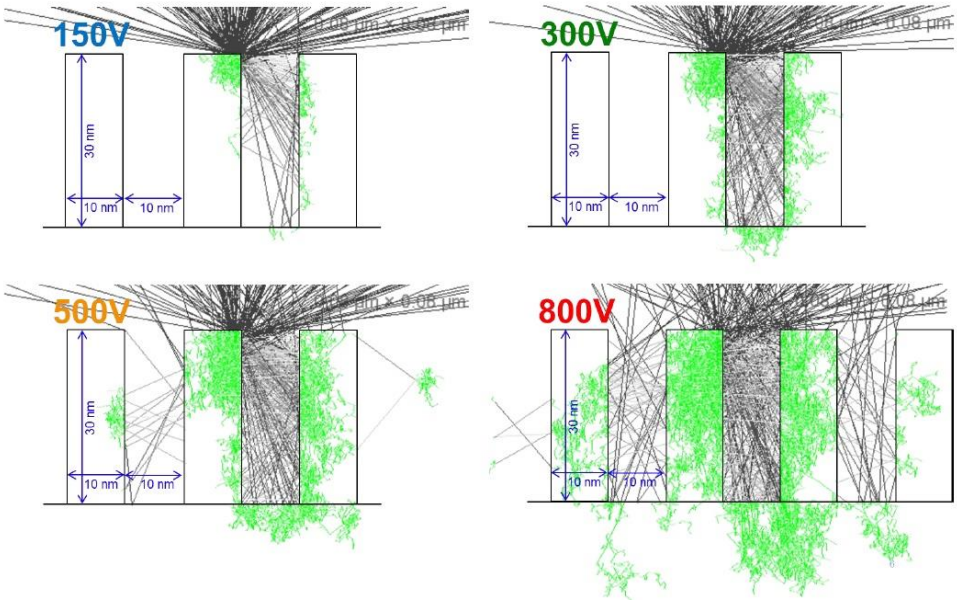


Fig. 1-1 Monte Carlo simulation results for Si structures in 10 nm scales [3].

In academic filed, SEMs for laboratories also began to adopt extremely low energy conditions [5-7]. In special cases, energy levels as low as 20 eV have been used. These extra-low energy conditions are used to reveal sub-surface and nanoscale information about the specimens and enhance chemical and crystalline signals because of the reduced interaction volumes. These SEMs offer numerous benefits for research on nanomaterials including metal-organic frameworks [8], chiral $TiO_2$ nanofibres [9], and zeolite nanosheets [10].

For (S)TEM, observation in lower energy conditions becomes important because it prevents specimens from knock-on damages for light elements materials [11, 12]. Figure 1-2 shows studies by Meyer et al. [12] on knock-on-damages to graphene. TEM images show that the number of defects on graphene that are generated by EBs with a high-energy condition of 100 keV increased as doses of EBs increased. The cross-section of the inelastic scattering for the damage decreases as energy decreases. A threshold energy of the damage exists around 80 keV, which means that the lower energy condition than the threshold enables to observe the graphene without the damage [12]. The advanced (S)TEMs have adopted energy conditions of 20-60 keV. Light elements (Low Z) and two-dimensional (2D) materials such as graphene or carbon nanotubes are very important for recent studies in materials and nano

science. Therefore, low energy observation, which is beneficial for the observation of these materials, becomes the important trend for (S)TEM.

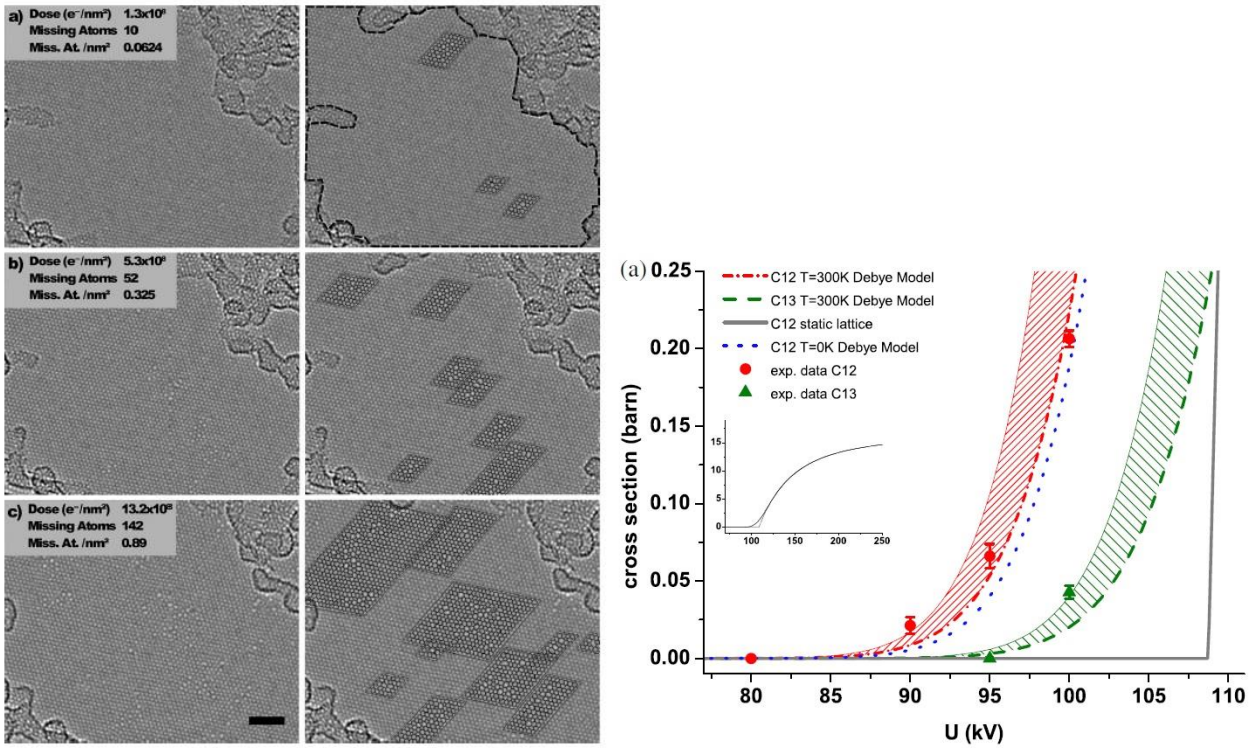


Fig. 1-2 (Left) Knock-on-damages to graphene by high energy EBs at 100 keV and (Right) measured and calculated cross section dependence on the beam energy [12].

## 1-3 Monochromators for electron microscopy

The low energy observation is a recent technology trend for both SEM and TEM. However, there exists a fundamental problem: deterioration of the spatial resolution. This limitation is attributed to chromatic aberration [1, 2], which can be described as

$$d_c = C_c \alpha \delta E_0 / E_0, \tag{1-1}$$

where $d_c$ is the beam diameter decided by the chromatic aberration, $C_c$ is the chromatic aberration coefficient, $\alpha$ is the acceptance angle, $\delta E_0$ is the energy spread of EBs, and $E_0$ is the beam energy. EBs generally suffer the energy spreads through their emission and propagation process. For Schottky emitters (SEs) and cold field emitters (CFEs), typical values of $\delta E_0$ are 600-800 meV and 300 meV, respectively. Figure 1-3 explains the influence of the chromatic

aberration to the beam diameter. Eq. (1-1) suggests that spatial resolutions of the EMs deteriorate severely at the low energy conditions because of its inversely proportional dependence on the energy $E_0$.

To solve this issue, MCs have recently been introduced into the EMs. The MCs can generate monochromatic beams with narrower energy spreads $\delta E_{MC}$ than native ones $\delta E_0$ from emitters. Figure 1-4 illustrates the effect of the MC. The reduced energy spreads can improve spatial resolutions in SEM and (S)TEM especially at low energy conditions based on Eq. (1-1).

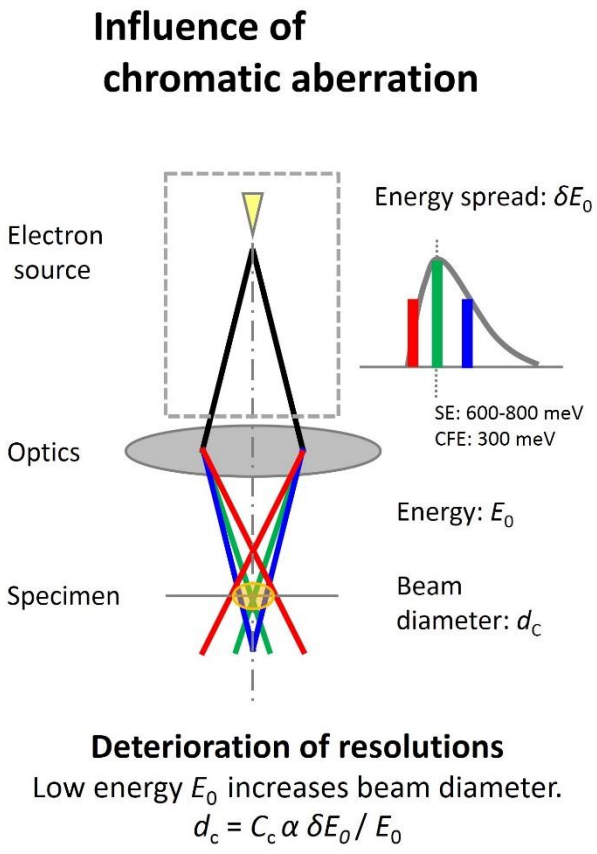


Fig. 1-3 Influence of chromatic aberration.

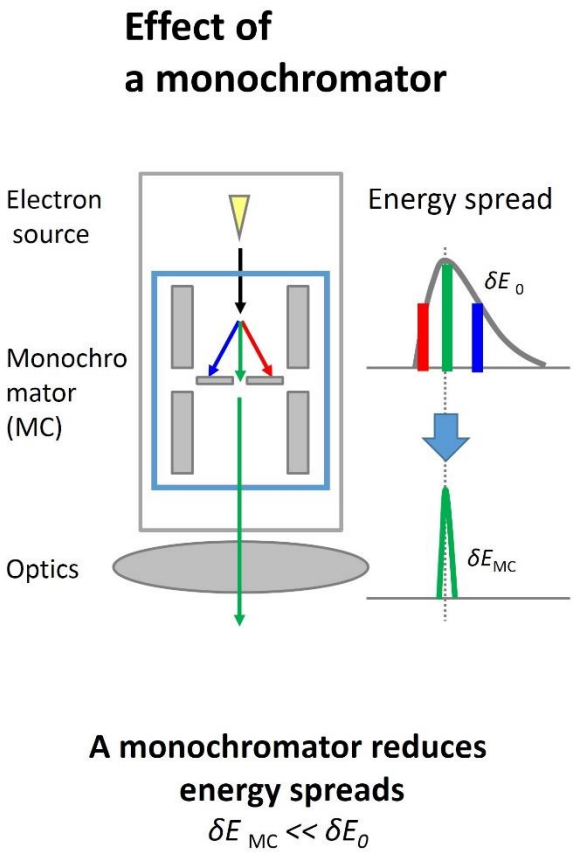


Fig. 1-4 Effect of a monochromator.

The discussion on the recent trend in EMs is summarized. For SEM, low energy conditions of several 100 eV are essential for observation of nano devices with reduced interaction volumes. For (S)TEM, low energy conditions of 20-60 keV are required for observation of low Z and 2D materials such as graphene without knock-on-damages. To overcome the deterioration of spatial resolutions caused by the chromatic aberration in the low energy conditions, MCs have been introduced into EMs. Figure 1-5 shows a schematic of an advanced EM with an MC.

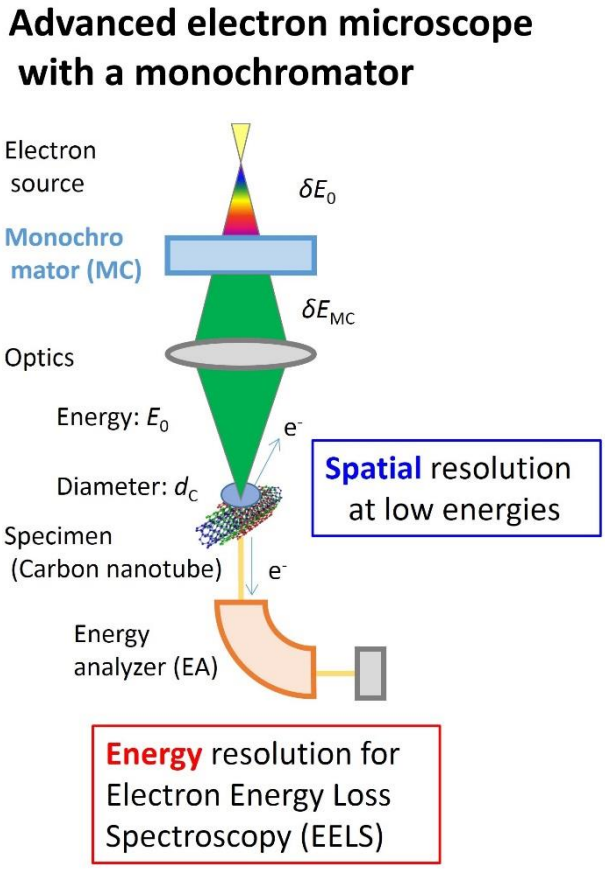


Fig. 1-5 Advanced electron microscope with an MC.

In Fig. 1-5, the advance EM additionally equips an energy analyzer (EA) for electron energy-loss spectroscopy (EELS). The adoption of the MCs for the EMs has opened up new research fields in EELS with improved energy resolutions. The MCs are effective for EELS especially in low loss energy regions because peaks and features that are hidden under broad energy spreads of native EBs become observable in EELS spectra. The improved EELS technique has contributed to new studies on the band gaps of semiconductors [13] and localized plasmons excited in the near-IR energy region [14]. Recently, Krivanek et al. achieved an energy resolution of 10 meV using a probe with a diameter of 1 nm at 60 keV with the magnetic Alfa MC [15-17]. Figure 1-6 shows obtained phonon spectra for h-BN with using the instrument [15]. Furthermore, a vibration spectroscopy study for biogenic guanine crystals was performed [18]. Fig. 1-7 shows the EELS spectrum, which revels vibration modes of C=O and hydrogen bonds, together with the IR spectrum for reference. The mapping of the spatial distribution of phonon signals of MgO nanocubes was successfully conducted [19]. These recent research results show that MCs are essential components in (S)TEM-EELS.

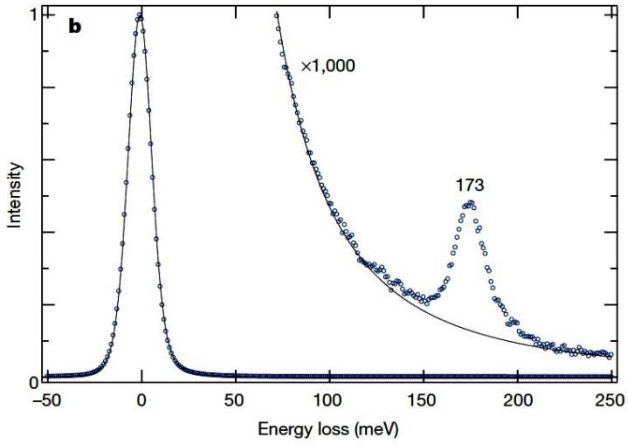


Fig. 1-6 Phonon spectrum of h-BN using MC with magnetic Alfa [15].

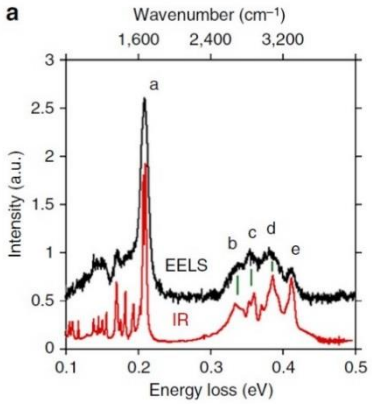


**Table 1 | Assignment of peaks observed by aloof EELS in the infrared region.**

| Peak | Energy (meV) | Frequency ($cm^{-1}$) | Assignment |
|---|---|---|---|
| a | 209 | 1,666 | C=O stretch |
| b | 334 | 2,663 | C-H stretch |
| c | 357 | 2,846 | N-H stretch |
| d | 386 | 3,078 | Symmetric $NH_2$ |
| e | 411 | 3,277 | Antisymmetric $NH_2$ |

EELS, electron energy loss spectroscopy.

Fig. 1-7 Vibration spectrum of biogenic guanine crystals by EELS and IR [18].

As discussed above, the MC technology has been essential in the latest EMs. Thus far, various types of MCs for EMs have been studied. With historical point of view, MCs have developed together with EAs. Therefore, the MC and EA will be reviewed at first. Then, the MCs for (S)TEMs and for SEM will be reviewed in detail.

## 1-4 Review of monochromators and energy analyzers

In principle, MCs and EAs can be considered to be equivalent optical units because both have the capabilities of generating energy dispersions and selecting energies with the use of slits. The difference between the two units is mainly their location and purpose: MCs are located at the pre-stage of specimens to reduce energy spreads of EBs from the initial energy distributions, and EAs are located at the post-stage of the specimen to analyze the EBs from the specimens and generate energy spectra.

MCs and EAs have been commonly used in high-resolution electron energy-loss spectroscopy (HREELS) to obtain phonon and vibration spectra on specimen surfaces with EBs in very low energy conditions of 1–10 eV [20]. Propst and Piper [21] successfully obtained the vibration spectra due to the adsorption of gas species on metal surfaces. This study opened up the new research field of HREELS. Figure 1-8 shows their HREELS instruments, which adopted the identical design of the MCs and EAs. Electrostatic cylindrical deflectors with the deflection angle of 127 degrees were utilized.

In analysis of thin specimens by transmitted electrons with higher energies of several 10 keV, identical optics of MCs and EAs with Wien filters were also used to obtain electronic or vibration spectra [22, 23]. The Wien filter is also known as an E × B, which represents its optical geometry of orthogonal magnetic and electrostatic fields. Figure 1-9 shows the schematic.

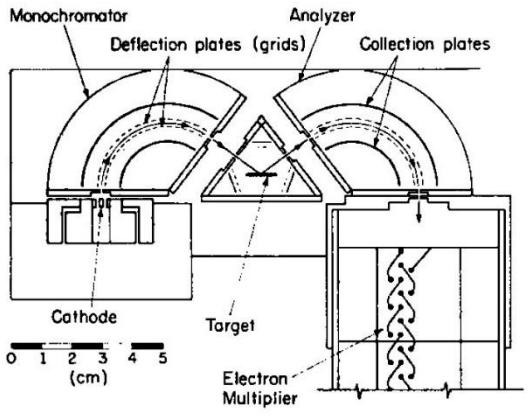


Fig. 1-8 MC and EA with cylindrical deflectors [21].

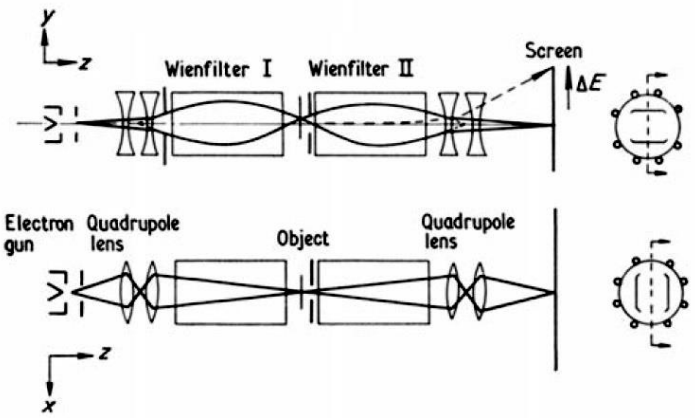


Fig. 1-9 MC and EA with Wien filters [23].

Schröder and Geiger [24] achieved energy resolutions of 4~6 meV at 25 keV and acquired phonon spectra of Si-O and Ge-O as shown in Figure 1-10. The authors adopted the MC in conjunction with a retarding Wien filter; By applying a negative high voltage to the filter to decelerate the EBs, the energy dispersion was increased and the high resolution was achieved. This result should be specially mentioned because it initiated and prompted subsequent studies on integration of the MCs into (S)TEM.

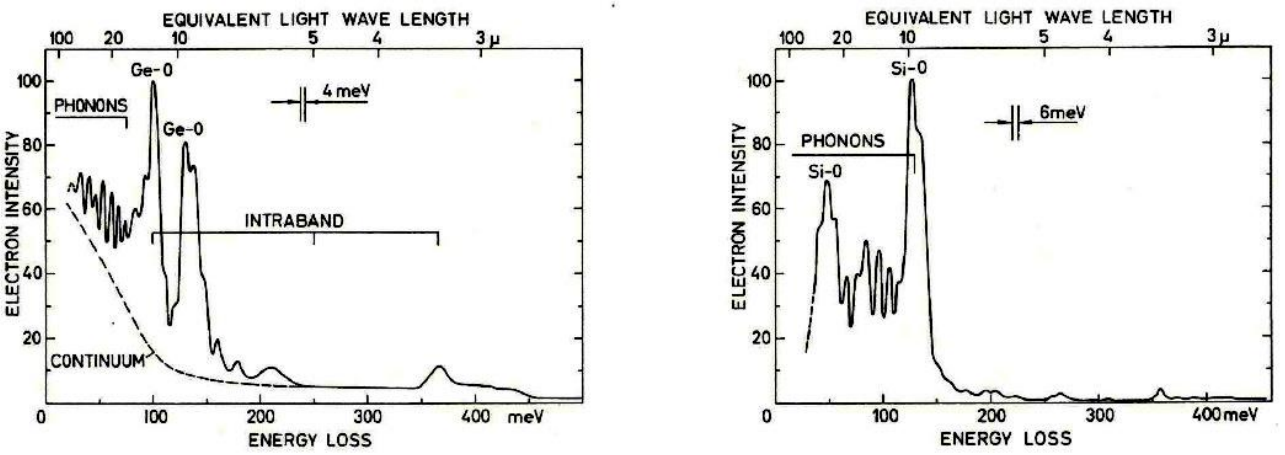


Fig. 1-10 Pioneering phonon study by Schröder and Geiger [24].

Various types of EAs have frequently been used in the field of surface science. For the HREELS instruments described above, EAs with cylindrical deflector type [20, 21] are commonly used. For surface analysis using photoelectrons generated by x-ray or ultraviolet (UV) sources, hemispherical energy analyzers (HSAs) with a deflection angle of 180 degrees are frequently adopted [25]. EAs are also used for the research on electron or ion emitters for measurements of total energy distributions (TEDs). In previous studies of Schottky emitters (SEs), the HSAs [26, 27] and retarding field energy analyzers (RFAs) [28, 29] were adopted.

Möllenstedt [30] developed another type of EAs for TEM-EELS, which utilized an off-axis chromatic aberration of a highly excited cylindrical lens (CL) with rectangular openings in its electrodes (Fig 1-11). Ichinokawa [31] developed a similar EA with a magnetic lens (Fig 1-12). These Möllenstedt EAs were operated mainly at high-energy conditions, which set limits on the energy resolutions of several eV [32].

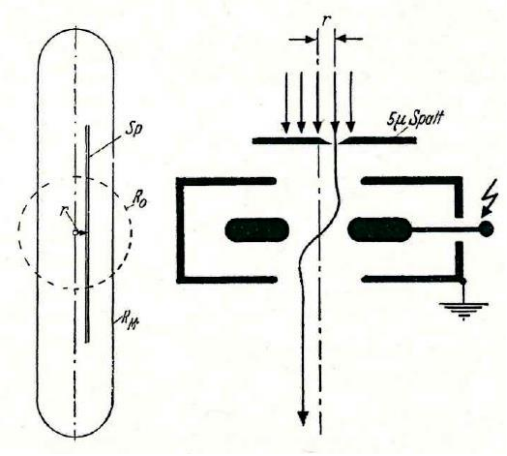


Fig. 1-11 EA with an electrostatic CL [30].

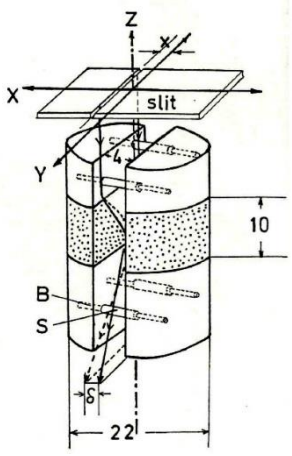


Fig. 1-12 EA with a magnetic CL [31].

## 1-5 Review of monochromators for (S)TEM

Terauchi et al. [33, 34] integrated an MC with the retarding Wien filter type into a TEM and achieved several tens of meV at 60 keV for a spatial area of 100 nm after optimizing the configurations of the filters. However, this design has a technical difficulty related to high voltages to the MC, which are required to be similar levels with the acceleration voltage of 60 kV to generate the retarding effects.

Later, Mook et al. [35, 36] proposed an MC with a thin Wien filter placed in the high-voltage region of an electron gun. This design has successfully solved the high voltage issues in the design by Terauchi. Figure 1-13 shows a schematic and a picture of the MC. Batson [37] achieved an energy resolution of 61 meV at 100 keV in STEM with the MC.

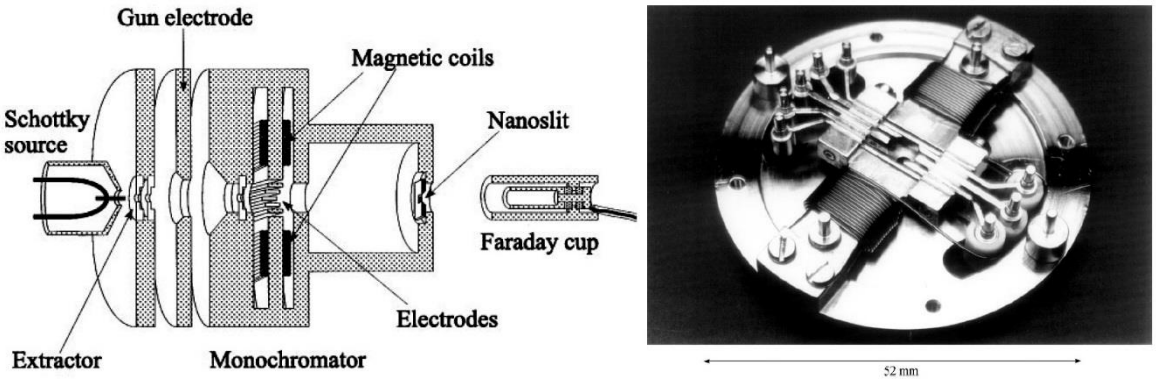


Fig. 1-13 MC with a thin Wien filter at the electron gun [36].

Similarly, various types of gun Wien filters have been proposed and commercialized, as follows: a relatively longer type [38], those with double stage-Wien filters [39-41], and those with quad stage-Wien filters [42]. Figure 1-14 shows simulation results and a picture of the MC with the double stage-Wien filter. The progress related to Wien filters, including their application to MCs, has been reviewed and summarized [43, 44].

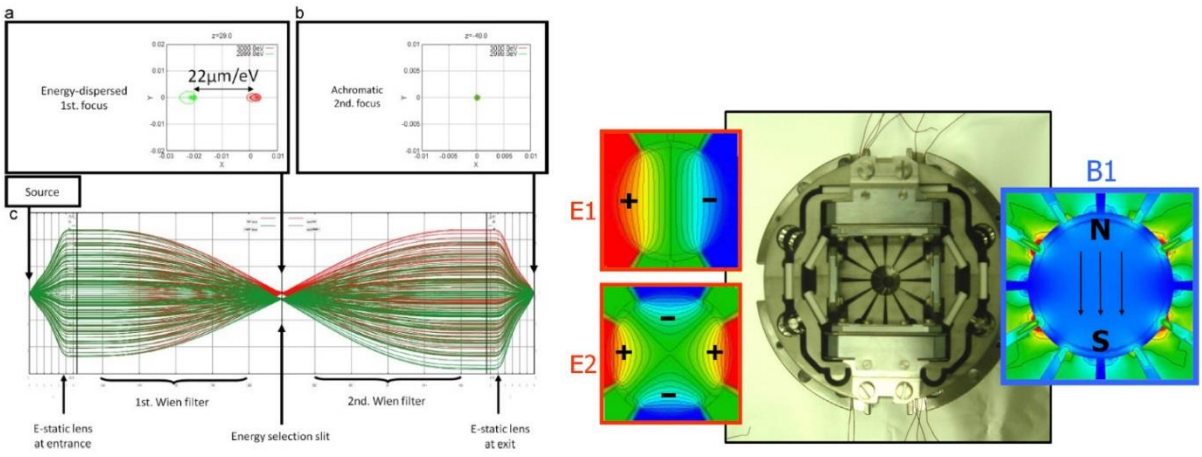


Fig. 1-14 MC with double stage-Wien filter [41].

Rose [45] proposed an electrostatic Ω-shaped MC located in the electron gun region. This MC consists of quad stage toroidal deflectors. The middle plane symmetric configuration and the curvatures of toroidal electrodes can cancel not only the energy dispersion but also all second-order geometric aberrations at the exit plane of the MC. Fig. 1-15 shows a schematic and picture of the MC. An energy resolution of approximately 40 meV at 200 keV was confirmed by TEM with an imaging energy filter [46, 47]. Another electrostatic MC using the quad stage of HSAs with deflection of 180º was also investigated [48].

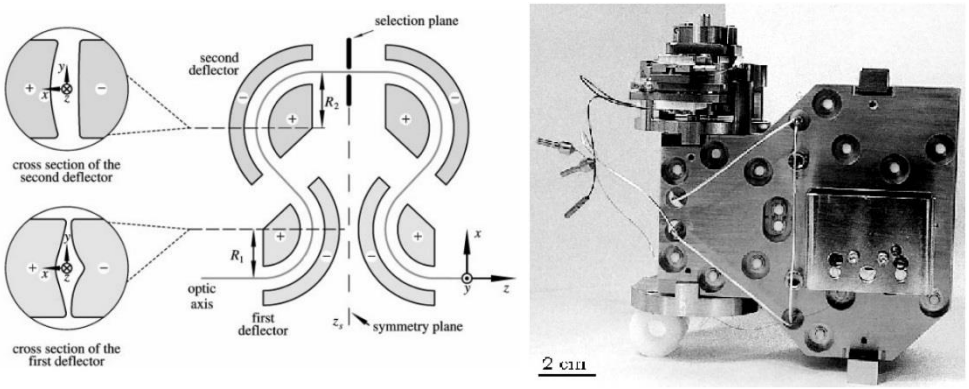


Fig. 1-15 MC with electrostatic Omega [45, 46].

Krivanek et al. [16, 17] proposed an MC with an α-shaped configuration of three magnetic sectors in the ground potential, where numerous multipoles among these sectors increased the energy dispersion and canceled second-order aberrations. Figure 1-16 shows schematics and the first order trajectories of the MC and its application to the STEM-EELS system.

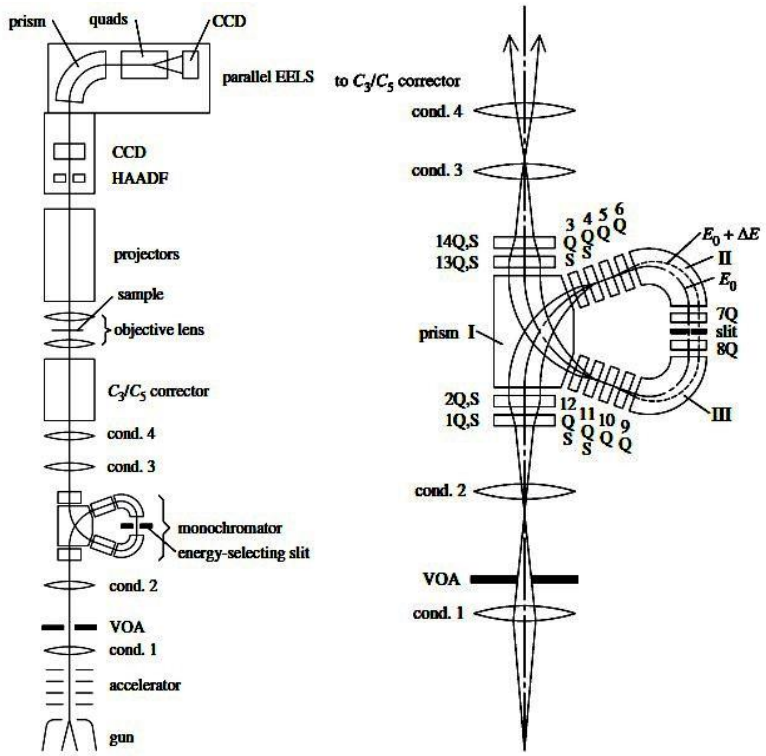


Fig. 1-16 MC with magnetic Alpha [16].

## 1-6 Review of monochromators for SEM

In focused electron and ion beam systems, Troyon [49] has proposed an MC in gun regions, which is a similar optics with the RFA, to improve the probe sizes. Assuming an ideal MC, Barth et al. [50] have estimated the probe sizes with a reduction of the chromatic terms and discussed their improvement in the low-energy region based on FW50 methods. Later, an MC with a modified gun lens was proposed and commercialized [51, 52]. The MC additionally equips two off-axis apertures and a deflector. Figure 1-17 shows schematics to explain the operational principle. Increasing the excitation of the lens enables to vary beam trajectories. By selecting an off-axial portion of an emitted beam with an aperture, energy dispersion occurs due to the off-axial chromatic aberration of the gun lens. By selecting the dispersed beam with another aperture behind the lens, energy filtering is realized. The monochromated beams are deflected back to the optical axis of the microscope by the deflector. The energy resolution of 150 meV is obtained and sub-nm SEM image resolutions are achieved in low-energy regions around 1 keV.

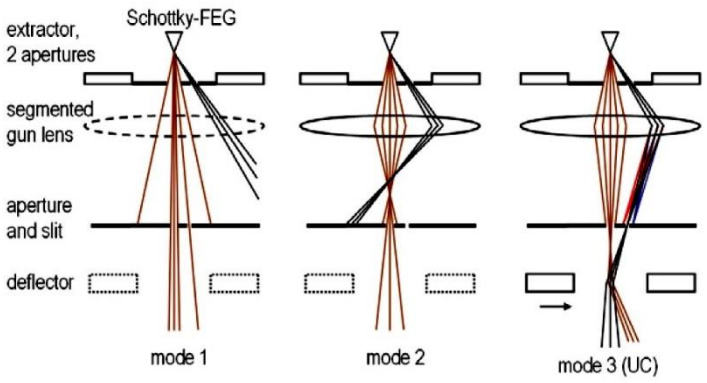


Fig. 1-17 MC with a modified gun lens for SEM [51].

For another type of surface microscopy, low-energy electron microscopy (LEEM), an MC using a combination of a magnetic sector and an electrostatic mirror was reported with a resolution of 100 meV [53]. Figure 1-18 shows a schematic and a picture of the MC.

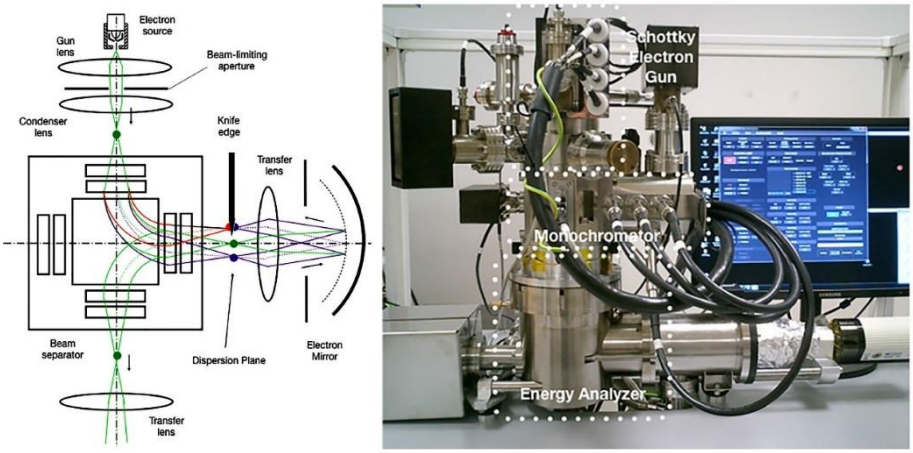


Fig. 1-18 MC with a sector magnet and a mirror for LEEM [53].

## 1-7 Main subject and outline of the study

As shown in the reviews in the previous sections, various types of MCs have been studied. Some of MCs have achieved high levels of performances in energy resolutions. However, instead of that, these MCs need to adopt complicated designs and lose the simplicity. MCs with Wien filters [35-44] adopt multipoles with electromagnetic pieces, which are divided in the azimuthal direction. The precise alignment of each pole is necessary for the assembling process. The MC with electrostatic Omega [45-47] adopts the toroidal shape of electrodes, which takes

different curvatures in the horizontal and vertical directions. This requires a very high level of machining techniques in three dimensions. The difficulties in manufacturing increase production costs of the instruments. The MC with magnetic Alpha [16, 17] adopts not only main three sector magnets for defining the beam path but also a large number of multipoles (14 quadrupoles and 8 hexapoles) for correcting aberration. A huge number of power supplies with high stabilities and low noise levels are necessary to control these correctors. In addition, the sophisticated calibration procedures with software controls are required. These MCs with complicated designs prevent EMs from robustness and easy operation. Therefore, it is necessary for the development of a new MC with high performance and simple structure. This is the main subject of this study. Figure 1-19 presents the background and main subject of this study.

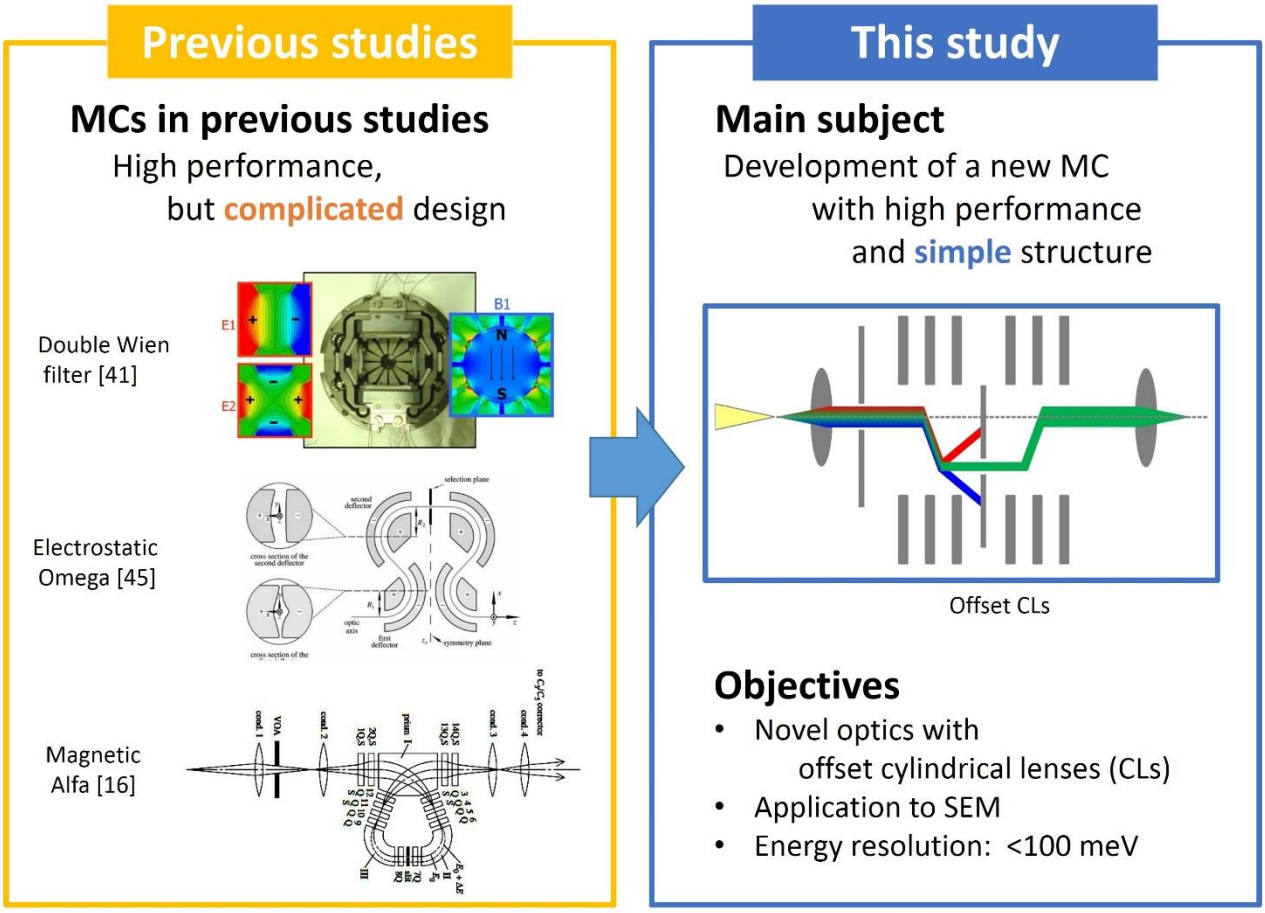


Fig. 1-19 Background and the main subject of this study.

In this study, the author will develop an MC with novel and original optics using offset cylindrical lenses (CLs). The adoption of the CLs enables to realize the MC with high performance and simple structure. This MC can

be used for both SEM and (S)TEM. Considering the importance in industrial fields such as semiconductor devices, SEMs will be choosen as the target application of the MC in this study. In the previous studies on MCs for surface microscopes such as SEM and LEEM, the energy resolutions were 150 meV [52] and 100 meV [53], respectively. Therefore, the target of this study is specified as an energy resolution better than 100 meV.

The MC optics with CLs enables the simple structure. The CLs can be manufactured with easier machining and assembling process. The simple design will result in high robustness and stability of the instruments, which is important for industrial applications. Additionally, this can reduce the total cost of the instrument, which is mandatory for SEM because the selling price is lower than that of TEM.

The MC in this study has another possibility in the application to various research activities. The recent progress in MCs for STEM-EELS has opened new research fields, for example, vibration and phonon spectroscopy in nanometer scales [15, 18, 19]. However, several issues remain; the signal level of the phonon spectrum in Fig. 1-6 is too low, and the peaks related to hydrogen bonds of the vibration spectrum in Fig. 1-7 are not resolved well. It is because the beam energy of 60 keV is too high to acquire the vibration spectra, which cause the low signal levels due to small cross sections of inelastic scatterings. The studies with HREELS in the lower beam energy conditions of 1−10 eV revealed finer structures in the spectra with higher sensitivity [20]. Therefore, there is room for further development of a new MC for low energy microscopes such as SEM to observe vibration and phonon signals with high sensitivity.

As a summary, in this study, the author will develop a new MC with high performance (<100 meV) and simple structure for SEM. The MC adopts novel and original optics with CLs.

In the following chapters, research results on the new MC with CLs will be discussed. Figure 1-20 presents an outline of this dissertation. In chapter 1, the background and the purpose of this study are clarified. The chapters 2-4 are on theoretical studies. The MC performance will be estimated theoretically through investigating its first-order Gaussian optics in chapter 2 and higher-order aberration in chapter 3. Additionally, the contribution of the MC to the SEM performance at low energy conditions will be discussed in chapter 4.

Based on the theory, a prototype of the MC optics will be designed and constructed in a test bench. Two chapters, chapter 5 and 6, are on experimental evaluation. In chapter 5, the first half of the MC optics, which mainly determines the energy resolution, will be evaluated. The electron optics includes the single offset CL and a round transfer lens. The energy resolving performance will be estimated by measuring the TED of the SEs. In chapter 6, the entire MC optics will be evaluated. The energy resolution will be estimated by measuring directly energy spread

of EBs with an additional EA on the downside. In conclusion, the results of this study will be summarized.

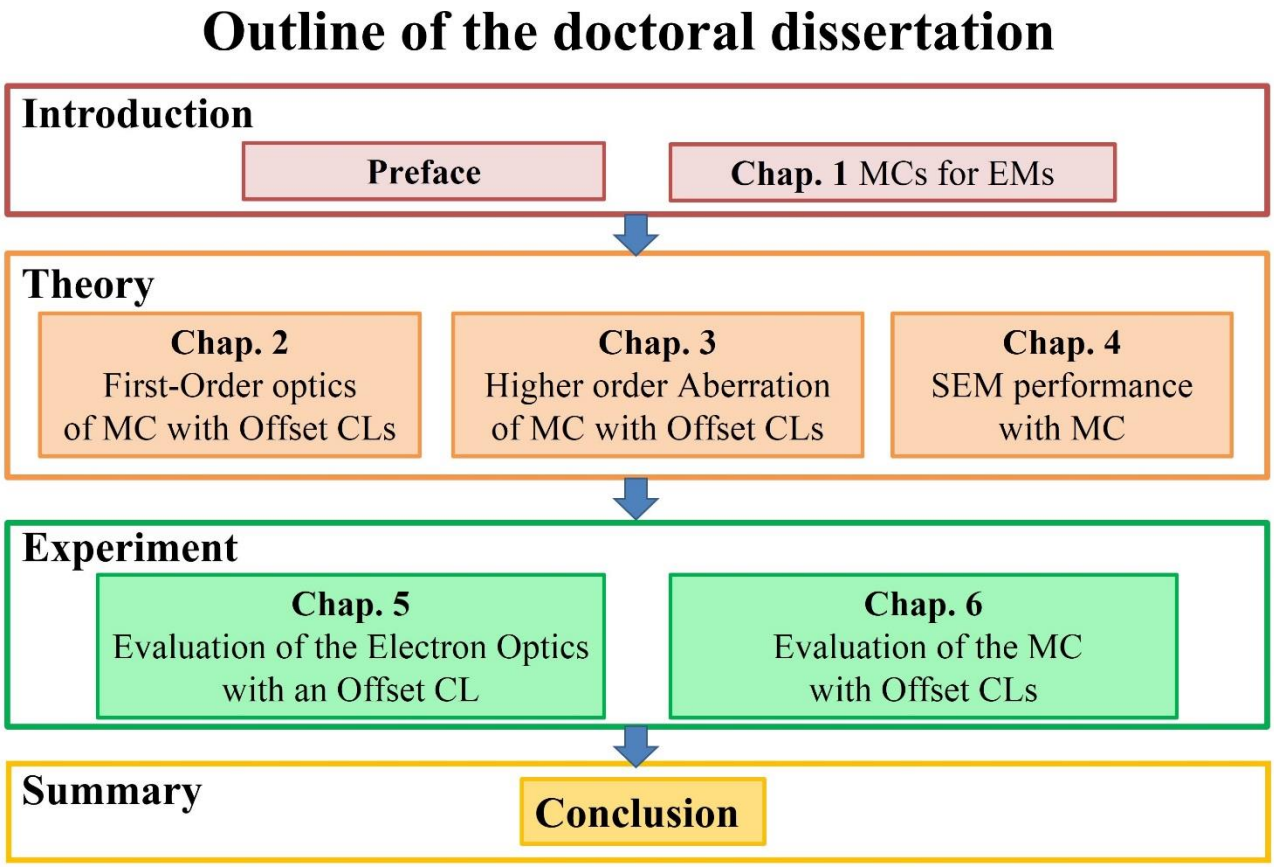


Fig. 1-20 Outline of the dissertation.

## 1-8 Conclusion

In this chapter, the background and main subject of this study were described. One of the recent trends of EMs is the observation in low energy conditions. For SEM, low energy conditions of several 100 eV were proposed for inspection of semiconductor devices with reduced interaction volumes of EBs inside the specimens. For (S)TEM, low energy conditions of 20-60 keV become essential for observation of light elements materials such as graphene without know-on damages on the specimens. The trend of low energy observation prompt advanced EMs to adopt MCs for improvement of spatial resolutions by reducing influence of chromatic aberration. Furthermore, MCs can improve energy resolution in EELS and opened up new study fields. Thus, the MCs are significant optical components for advanced EMs. The technologies of MCs were explained through reviewing previous studies. MCs in previous studies achieved a high-performance level but required complicated structures. Therefore, the main theme

of this study is a development of a new MC with high performance and simple structure. SEM is considered as the application of the MC in this study because of the importance of industrial application. Considering that the energy resolution of MCs for SEM is 150 meV and that for LEEM is 100 meV in previous studies, the target of this study was specified as an energy resolution better than 100 meV. Finally, the outline of this dissertation was explained.

## Reference

[1] L. Reimer, "*Scanning Electron Microscopy*", 2nd ed., (Springer Berlin Heidelberg, Berlin, Heidelberg, 1998).

[2] L. Reimer, H. Kohl, "*Transmission Electron Microscopy*", 5th ed., (Springer New York, New York, 2008).

[3] B. Bunday, A. Cepler, A. Cordes, A. Arceo, Proc. SPIE 9050 (2014) 90500T.

[4] B. Bunday, E. Solecky, A. Vaid, A.F. Bello, X. Dai, Proc. SPIE 10145 (2017) 101450G.

[5] A. E. Vladár and M. T. Postek, "*Handbook of Charged Particle Optics*", 2nd ed., edited by J. Orloff, (CRC Press, Boca Raton, 2009), Chap. 9, 437.

[6] N. Erdman and D. C. Bell, "*Low voltage electron microscopy: Principles and Applications*", edited by D. C. Bell, N. Erdman, (John Wiley & Sons Ltd, West Sussex, 2013), Chap. 2, 31; Chap. 4, 73.

[7] M. Suga, S. Asahina, Y. Sakuda, H. Kazumori, H. Nishiyama, T. Nokuo, V. Alfredsson, T. Kjellman, S. M. Stevens, H. S. Cho, M. Cho, L. Han, S. Che, M. W. Anderson, F. Schüth, H. Deng, O. M. Yaghi, Z. Liu, H. Y. Jeong, A. Stein, K. Sakamoto, R. Ryoo, and O. Terasaki, Prog. Solid State Ch. 42 (2014) 1.

[8] H. Deng, S. Grunder, K. E. Cordova, C. Valente, H. Furukawa, M. Hmadeh, F. Gándara, A. C. Whalley, Z. Liu, S. Asahina, H. Kazumori, M. O'Keeffe, O. Terasaki, J. F. Stoddart, and O. M. Yaghi, Science 336 (2012) 1018.

[9] S. Liu, L. Han, Y. Duan, S. Asahina, O. Terasaki, Y. Cao, B. Liu, L. Ma, J. Zhang, and S. Che, Nat. Commun. 3 (2012) 1215.

[10] X. Zhang, D. Liu, D. Xu, S. Asahina, K. A. Cychosz, K. V. Agrawal, Y. Wahedi, A. Bhan, S. Hashimi, O. Terasaki, M. Thommes, and M. Tsapatsis, Science 336 (2012) 1684.

[11] U. Kaiser, J. Biskupek, J.C. Meyer, J. Leschner, L. Lechner, H. Rose, M. Stöger-Pollach, A.N. Khlobystov, P. Hartel, H. Müller, M. Haider, S. Eyhusen, G. Benner, Ultramicroscopy 111 (2011) 1239.

[12] J.C. Meyer, F. Eder, S. Kurasch, V. Skakalova, J. Kotakoski, H.J. Park, S. Roth, A. Chuvilin, S. Eyhusen,

G. Benner, A.V. Krasheninnikov, U. Kaiser, Phys. Rev. Lett. 108 (2012) 196102.

[13] K. Kimoto, G. Kothleitner, W. Grogger, Y. Matsui, F. Hofer, Micron 36 (2005) 185.

[14] D. Rossouw, M. Couillard, J. Vickery, E. Kumacheva, G.A. Botton, Nano Lett. 11 (2011) 1499.

[15] O.L. Krivanek, T.C. Lovejoy, N. Dellby, T. Aoki, R.W. Carpenter, P. Rez, E. Soignard, J. Zhu, P.E. Batson, M.J. Lagos, R.F. Egerton, P. Crozier, Nature 514 (2014) 209.

[16] O.L. Krivanek, J.P. Ursin, N.J. Bacon, G.J. Corbin, N. Dellby, P. Hrncirik, M.F. Murfitt, C.S. Own, Z.S. Szilagyi, Phil. Trans. R. Soc. A 367 (2009) 3683.

[17] O.L. Krivanek, T.C. Lovejoy, N. Dellby, R.W. Carpenter, Microscopy 62 (1) (2013) 3.

[18] P. Rez, T. Aoki, K. March, D. Gur, O.L. Krivanek, N. Dellby, T.C. Lovejoy, S.G. Wolf, H. Cohen, Nat. Commun. 7 (2016) 10945.

[19] M.J. Lagos, A. Trügler, U. Hohenester, P.E. Batson, Nature 543 (2017) 529.

[20] H. Ibach, D.L. Mills, "*Electron Energy Loss Spectroscopy and Surface Vibrations*", (Academic Press, New York, 1982).

[21] F.M. Propst, T.C. Piper, J. Vac. Sci. Technol. 4 (1967) 53.

[22] H. Boersch, J. Geiger, W. Stickel, Z. Phys. 180 (1964) 415.

[23] W. Andersen, J. Le Poole, J. Phys. E. 3 (1970) 121.

[24] B. Shröder, J. Geiger, Phys. Rev. Lett. 28 (1972).

[25] H. Ibach, "*Physics of Surfaces and Interfaces*", (Springer Berlin Heidelberg, Berlin, 2006).

[26] M.J. Fransen, J.S. Faber, T.L. van Rooy, P.C. Tiemeijer, P. Kruit, J. Vac. Sci. Technol. B. 16 (1998) 2063.

[27] H.S. Kim, M.L. Yu, E. Kratschmer, B.W. Hussey, M.G.R. Thomson, T.H.P. Chang, J. Vac. Sci. Technol. B. 13 (1995) 2468.

[28] L.W. Swanson, J. Vac. Sci. Technol. 12 (1975) 1228.

[29] S. Sakawa, K. Tsunoda, Y. Terui, Surf. Interface Anal. 35 (2003) 11.

[30] G. Möllenstedt, Optik (Stuttg) 5 (1949) 499.

[31] T. Ichinokawa, Jpn. J. Appl. Phys. 7 (8) (1968) 799.

[32] S.L. Cundy, A.J.F. Metherell, M.J. Whelan, J. Sci. Instrum. 43 (1966) 712.

[33] M. Terauchi, R. Kuzuo, F. Satoh, M. Tanaka, K. Tsuno, J. Ohyama, Microsc. Microanal. Microstruct. 2 (1991) 351.

[34] M. Terauchi, M. Tanaka, K. Tsuno, M. Ishida, J. Microscopy 194, 1 (1999) 203.

[35] H.W. Mook, P. Kruit, Nucl. Instr. Meth. A 427 (1999) 109.

[36] H.W. Mook, P. Kruit, Ultramicroscopy 81 (2000) 129.

[37] P.E. Batson, Ultramicroscopy 78 (1999) 33.

[38] P.C. Tiemeijer, Ultramicroscopy 78 (1999) 53.

[39] G. Martínez, K. Tsuno, Ultramicroscopy 93 (2002) 253.

[40] M. Mukai, W. Inami, K. Omoto, T. Kaneyama, T. Tomita, K. Tsuno, M. Terauchi, K. Tsuda, M. Naruse, T. Honda, M. Tanaka, Microsc. Microanal. 12 (Suppl. 2) (2006) 1206CD.

[41] M. Mukai, J.S. Kim, K. Omoto, H. Sawada, A. Kimura, A. Ikeda, J. Zhou, T. Kaneyama, N.P. Young, J.H. Warner, P.D. Nellist, A.I. Kirkland, Ultramicroscopy 140 (2014) 37.

[42] E. Plies, J. Bärtle, Microsc. Microanal. 9 (Suppl. 3) (2003) 28.

[43] E. Plies, K. Marianowski, T. Ohnweiler, Nucl. Instr. Meth. A 654 (2011) 7.

[44] K. Tsuno, D. Ioanoviciu, "The Wien Filter, Advances in Imaging and Electron Physics, Volume 176", (Academic Press, Amsterdam, 2013).

[45] H. Rose, Ultramicroscopy 78 (1999) 13.

[46] S. Uhlemann, M. Haider, Microsc. Microanal. 8 (Suppl. 2) (2002) 584CD.

[47] E. Essers, G. Benner, T. Mandler, S. Meyer, D. Mittmann, M. Schnell, R. Höschen, Ultramicroscopy 110 (2010) 971.

[48] A. Huber, J. Bärtle, E. Plies, Nucl. Instr. Meth. A 519 (2004) 320.

[49] M. Troyon, Microelectron. Eng. 6 (1987) 105.

[50] J.E. Barth, M.D. Nykerk, H.W. Mook, P. Kruit, EUREM 12, Brno, Czech Republic, (2000) 1437.

[51] A. Henstra, J. Chmelik, T. Dingle, A. Mangnus, G. van Veen, Microsc. Microanal., 15 (Suppl. 2) (2009) 168.

[52] R.J. Young, G.N.A. van Veen, A. Henstra, L. Tuma, "*Low Voltage Electron Microscopy: Principles and Applications*", edited by D.C. Bell, N. Erdman, (John Wiley & Sons, West Sussex, 2012), Chap. 3, 57.

[53] M. Mankos, K. Shadman, V. Kolarik, J. Vac. Sci. Technol. B. 34 (2016) 06KP01.

# Chapter 2 First-Order Optics of the Monochromator with Offset Cylindrical Lenses

## 2-1 Introduction

In this chapter, a new MC with offset cylindrical lenses (CLs) will be constituted with a theoretical means. The offset CL can generate energy dispersions similarly with Möllenstedt energy analyzers [1, 2]. First, an optical axis and first-order matrix expressions for a single offset CL will be derived from various ray trace simulations. Next, a new MC with multiple offset CLs will be constituted based on the matrix expressions. Then, the performance and the mechanical tolerance of the MC will be discussed.

## 2-2 Monochromator with offset cylindrical lenses

In this study, the MC with offset CLs is developed. First, the optics of the MC is briefly described. Fig. 2-1 presents a schematic of the MC. The MC takes the middle plane symmetry in its optical configuration at $Z_2$. Each half of the MC contains a CL and a round transfer lens (TL). The CLs are in an offset layout, which means that the center axis of the CLs is offset to the optical axis. This enables the CL to serve as deflection units. The first CL (CL1) deflects electron beams (EBs) and generates energy dispersions, and the subsequent second CL (CL2) deflects the beam back to the original axis. As a result, main beam trajectories also take the middle plane symmetry. The first TL (TL1) collimates EBs from the SE at $Z_0$, and the second TL (TL2) focuses the beams on the exit plane at $Z_4$. An incident aperture at $Z_1$ confines region of the EBs inside the MC. An energy selection aperture on the middle plane at $Z_2$ filters the zero-loss beams from the energy-dispersed beams. As a complete optical component, the MC can achieve a round and stigmatic focus condition on the exit plane. Furthermore, the optics with the middle plane symmetry enables to cancel the energy dispersion and the second order aperture aberration. The following theoretical studies will provide detailed discussion on the MC optics.

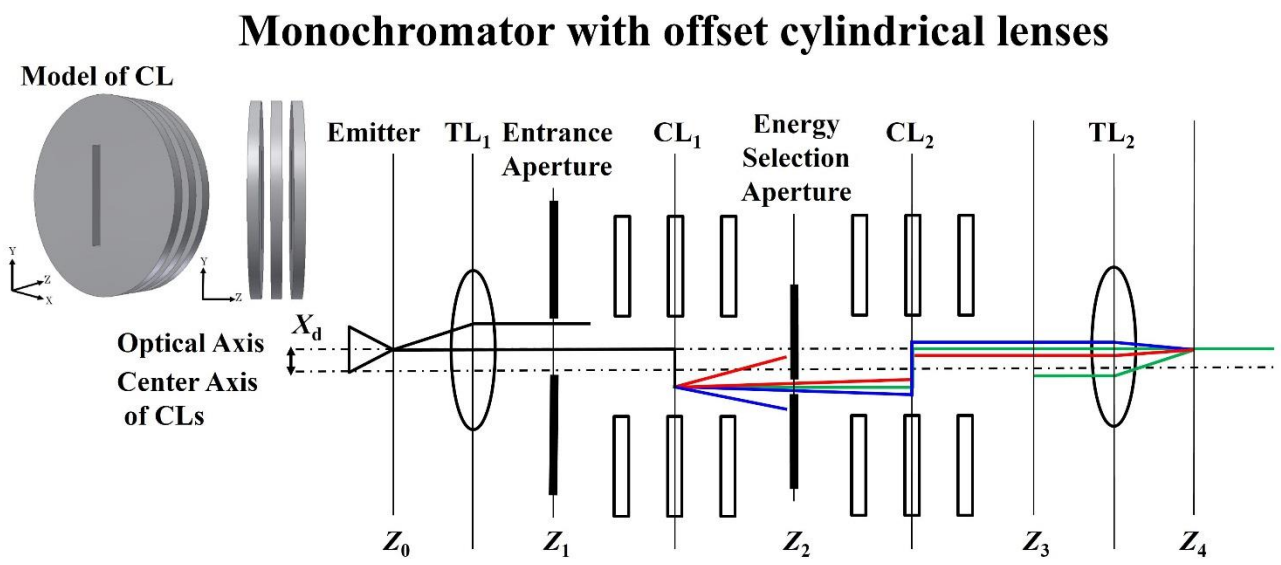


Fig. 2-1 Monochromator with offset cylindrical lenses

Next, the CL is described. The CL is a key component for the MC optics. A model of CL is shown as an inset at the left top side in Fig. 2-1. It consists of three electrodes with rectangular openings in their centers. Applying high voltage to the center electrode creates a stronger focusing effect in the direction of the shorter side of the opening and a weaker focusing effect in the other direction of the longer side. Here, a Cartesian coordinate is introduced as (X, Y, Z). The Z-axis is defined as the travel direction of the charged particles, and it passes through the center of the rectangular openings of the electrodes. The X-axis is adopted as the stronger focusing direction and the Y-axis is chosen as the weaker focusing direction. The detailed dimensions of the lenses are as follows: the thickness of the electrodes is 10 mm, the gap between the electrodes is 10 mm, the shorter side of the opening is 10 mm, and the longer side of the opening is 100 mm. The same parameters are adopted for all three electrodes of the CL and the same geometries are used for each CL in multiple configurations because doing so simplifies the investigations of the MCs.

In the following sections, the new MC with multiple offset CLs will be constituted and the performance of the MC will be estimated.

## 2-3 Method

To investigate the optics of MCs with multiple CLs, it is difficult to use conventional paraxial approximation methods because the optical axis passes through a non-uniform and complicated electric field distribution in the off-

axis region of the CLs. Thus, the author takes a new approach to study this. First, direct ray trace simulations are performed for a single CL to determine its optical axis and paraxial rays. By analyzing the results, the optical parameters and first-order matrix expressions are deduced. Based on the matrix, new optics for an MC with multiple CLs is established. Then, the performances of the MCs are investigated by combined calculations of ray trace and matrix methods, including the contributions from higher order aberrations.

In this study, the simulations are done with a charged-particle optics software (EO-3D, MEBS Ltd), which can calculate 3D electrostatic fields for various electrodes by the finite difference method and trajectories by the ray trace method based on these fields. For the analysis of the trajectories, the regression analysis functions of Microsoft Excel are used.

## 2-4 Results

### 2-4-1 Optical properties of a single offset CL

First, the optical axis of a single offset CL is discussed. Its mathematical expressions are defined as $X_{\text{optical axis}}$ (Z) and $Y_{\text{optical axis}}$ (Z) for the functions of Z in each direction. For an MC using multiple CLs, the optical axis should be parallel to the axis of the microscope at the entrance plane $Z_i$ and the exit plane $Z_j$. The index numbers i and j are natural numbers meaning two subsequent planes along the Z axis. To generate the energy dispersion, the optical axis must be offset from the CL center axis in the X direction, where the CL has strong lens effects, because the ray on the CL center axis has no energy dispersion due to its symmetry. In the Y direction, the optical axis corresponds to the CL axis through an optical path from $Z_i$ to $Z_j$. These conditions are described as follows:

$$X_{optical\ axis}(Z_i) \equiv X_d \neq 0,\ \partial X_{optical\ axis}(Z_i)/\partial Z = \partial X_{optical\ axis}(Z_j)/\partial Z = 0, \quad \text{(2-1a)}$$

$$Y_{optical\ axis}(Z) = 0\ (Z_i \leq Z \leq Z_j). \quad \text{(2-1b)}$$

A number of trajectories are calculated by varying the offset distances to the CL axis. The selected incident energy $E_0$ is 4 keV. The voltages of the center electrode are adjusted in the region where the CL is highly excited. As a result, Fig. 2-2 shows the optical axis satisfying the above conditions for the Z-X plane. In addition, Fig. 2-2 shows two rays which are ± 20 μm offset and parallel to the optical axis at $Z_i$. At this point, $X_{\text{optical axis}}$ (Z) and $Y_{\text{optical axis}}$ (Z)

are redefined as mathematic expressions of the optical axis in Fig. 2-2. By analyzing the trajectory at the exit plane $Z_j$, a relationship is established with an error of 0.1%, as follows:

$$X_{optical\ axis}(Z_j) = -X_{optical\ axis}(Z_i) = -X_{\mathrm{d}}. \tag{2-2}$$

On the X-Z plane, the two offset rays are focused onto the optical axis at the center of the CL and focused again on a plane at a distance of $f_c$. This plane is regarded as the back focal plane, and $f_c$ is interpreted as the focal length of the CL by considering these rays as paraxial rays, similar to conventional optics.

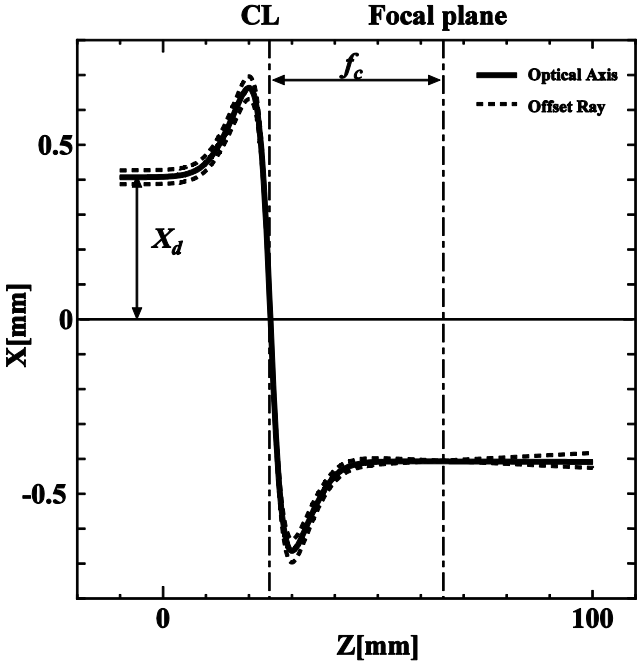


Fig. 2-2 Optical axis and offset rays on the Z-X plane.

These two parameters, the focal length $f_c$ and the offset distance $X_d$, are important in describing the optics of the offset CL and in constituting multiple CLs. To understand these dependencies on the excitation of the CL, several calculations are done to find trajectories that satisfy Eq. (2-1) in a manner similar to Fig. 2-2 for various center voltages of the CL. The series of solutions for the parameters are shown in Fig. 2-3. The horizontal axis corresponds to the ratio of the center electrode voltage $V_{\mathrm{center}}$ to the side electrode voltage $V_{\mathrm{side}}$ for normalization. The reference voltage is the acceleration voltage of −4 kV. By decreasing the center electrode voltage, or highly exciting the CL, the offset distance $X_d$ decreases and the focal length $f_c$ increases. In the following section of this study, $f_c$=40 mm is

chosen, with the other values being $X_d$=0.407 mm and $V_{center}$=−0.248 kV from Fig. 2-3. Based on this relationship, the optics of multiple CLs can be established. For example, two CLs are placed at a distance of $2f_c$=80 mm.

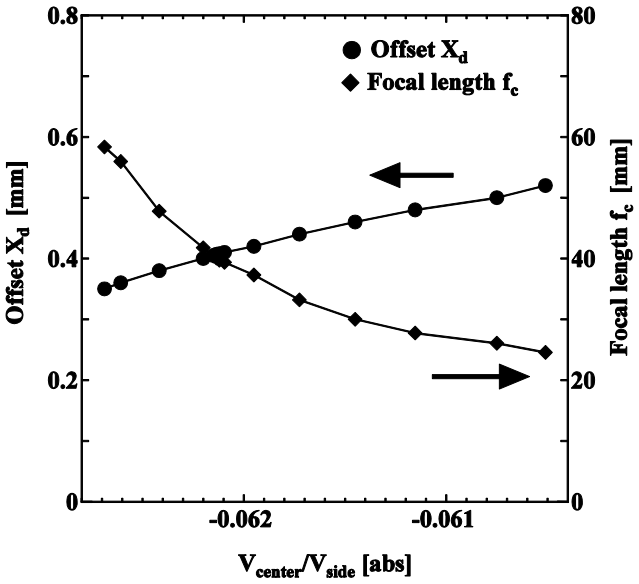


Fig. 2-3 Offset $X_d$ and focal length $f_c$ dependency on the excitation of the CL.

## 2-4-2 First-order matrix expressions of a single offset CL

Here, the optics of a single offset CL is discussed in detail by expressing it in a first-order matrix and deriving its energy dispersion. These mathematic expressions are based on textbooks [3, 4]. The notations are defined as follows: lateral deviations as $x$ and $y$, angles of inclinations as $a$ and $b$, and the deviation of the kinetic energy as $\kappa$. The charged particle transferred from $Z_i$ to $Z_j$ by an optical component can be written using two matrixes, as

$$\begin{pmatrix} x_j \\ a_j \\ \kappa_j \end{pmatrix}_{Z_j} = \begin{pmatrix} (x|x) & (x|a) & (x|\kappa) \\ (a|x) & (a|a) & (a|\kappa) \\ 0 & 0 & 1 \end{pmatrix}_{ij} \begin{pmatrix} x_i \\ a_i \\ \kappa_i \end{pmatrix}_{Z_i} + (higher\ order)\,, \tag{2-3a}$$

$$\begin{pmatrix} y_j \\ b_j \end{pmatrix}_{z_j} = \begin{pmatrix} (y|y) & (y|b) \\ (b|y) & (b|b) \end{pmatrix}_{ij} \begin{pmatrix} y_i \\ b_i \end{pmatrix}_{z_i} + (higher\ order)\,. \tag{2-3b}$$

For a single CL, these matrixes are termed $CLX_{ij}$ and $CLY_{ij}$. A single CL in the geometry is considered as follows: an incident plane in $Z_1$, the center of the CL in $Z_1+f_c$, and the exit plane in $Z_2=Z_1+2f_c$. Its matrixes are described as

$CLX_{12}$ and $CLY_{12}$.

In the conventional theory, the matrixes are derived by means of the paraxial approximation. However, we utilize another method, in which the coefficients of the matrixes are derived by a regression analysis of a number of ray trace results with different initial conditions. To determine the coefficients in the first column of $CLX_{12}$, multiple incident conditions of $(x_1, 0,0,0,0; Z_1)$ are used and regression analysis is applied to the ray trace results of $(x_2, \alpha_2, 0,0,0; Z_2)$ based on third-degree polynomials. Fig. 2-4 shows the results. The derived first-degree coefficients of the polynomials correspond to the first column of $CLX_{12}$. Similarly, all coefficients of the matrixes are derived and summarized in Table 2-1.

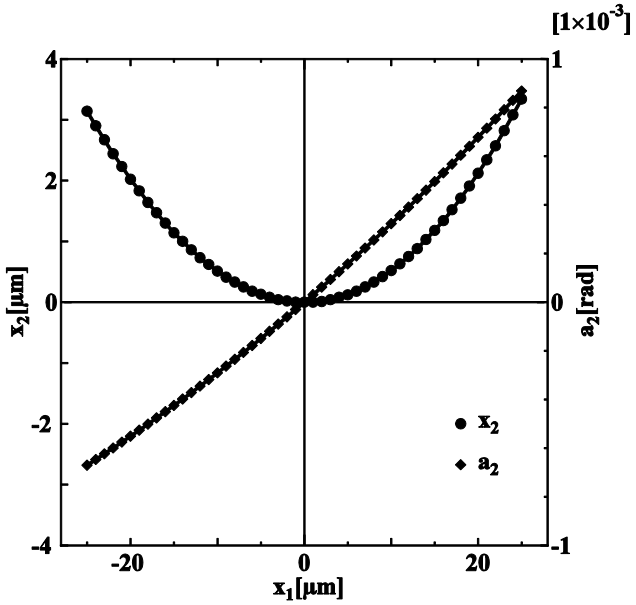


Fig. 2-4 Exiting position $x_2$ and inclined angle $a_2$ dependency on the incident position $x_1$.

Table 2-1 The calculated matrix coefficients of a single CL.

| | | | | | | |
|---|---|---|---|---|---|---|
| $CLX_{12}$ | $(x\|x)$ | $(x\|a)$ | $(x\|\kappa)$ | $(a\|x)$ | $(a\|a)$ | $(a\|\kappa)$ |
| | 0.00 | −32.65 | −93.93 | 0.03 | 0.00 | −2.89 |
| $CLY_{12}$ | $(y\|y)$ | $(y\|b)$ | $(b\|y)$ | $(b\|b)$ | | |
| | 1.00 | 126.85 | 0.00 | 1.01 | | |

The first rows of $CLX_{12}$ and $CLY_{12}$ are in mm, the second rows are in rad, and the third rows are dimensionless. The worst multiple correlation factor value of $R^2$ for ten terms is 99.988%. This value is high enough to support the

reliability of the coefficients. The geometric terms in $CLX_{12}$ suggest that the single offset CL functions as a lens in the X direction. $Z_1$ and $Z_2$ are considered as the front and back focal planes at the distance of the focal length $f_c$ from the center of the CL. For the matrix expression, the value of the focal length must be corrected to $(x|a) = s \cdot f_c$ by a factor $s$=−0.82. From the results of the chromatic terms in $CLX_{12}$, the following relationship is established with an error of 0.3%:

$$(a|\kappa) = -(x|\kappa)/(x|a) = -d/(s \cdot f_c)\,. \tag{2-4}$$

The parameter $d$ is introduced as $d \equiv (x|\kappa)$. In addition, the energy dispersion $D_\kappa$, an important factor for energy filters, can be calculated as $D_k = |(x|\kappa)/E_0| = 23.5\ \mu\text{m/eV}$ for an incident energy $E_0$ of 4 keV. This is a relatively large value compared to previous MCs.

Next, the matrix is discussed in the Y direction. From the form of $CLY_{12}$, the CL can be treated as a drift space in the Y direction. A parallel ray ($y_\beta$) remains parallel. An inclined ray ($y_\delta$) maintains its trajectory in almost all paths, but it is shifted to the off-axis direction without angle variation at the CL center. The total drift distance of the ray is expressed as the sum of the exact geometrical distance $2f_c$ between $Z_1$ and $Z_2$ and an additional distance $t$ by the shift effect of the CL. Thus, $(y|b)$ is described as $2f_c+t$, where $t$=46.85 mm.

From the discussion above, the matrix expressions of the single CL are expressed as follows:

$$CLX_{12} = \begin{pmatrix} 0 & s \cdot f_c & d \\ -1/(s \cdot f_c) & 0 & -d/(s \cdot f_c) \\ 0 & 0 & 1 \end{pmatrix}_{12}, \tag{2-5a}$$

$$CLY_{12} = \begin{pmatrix} 1 & 2f_c + t \\ 0 & 1 \end{pmatrix}_{12}. \tag{2-5b}$$

### 2-4-3 Optics of multiple offset CLs

Here, we consider multiple offset CL optics for constituting MCs. First, we discuss the matrix expression of a CL doublet. Two CLs ($CL_1$ and $CL_2$) are arranged in mid-plane symmetry with $Z_2$. The CLs are equally excited, with the same focal length of $f_c$. The centers of $CL_1$ and $CL_2$ are separated by $2f_c$. $CL_1$ is located at $Z_1+f_c$ as above and $CL_2$ is located at $Z_2+f_c=Z_1+3f_c$. From this configuration, the front focal plane of $CL_2$ corresponds to the back focal plane

of $CL_1$ in $Z_2$. The back focal plane of $CL_2$ is at $Z_3=Z_2+2f_c=Z_1+4f_c$. Therefore, the three planes, $Z_1$, $Z_2$, and $Z_3$, are conjugated optically. In total, the CL doublet constitutes the 4f optics, which is known in the field of light optics [5].

Next, we discuss the optical axis of the CL doublet. Fig. 2-5a shows the result of the ray trace simulation. After passing the CL doublet, the optical axis is coincident to the incident optical axis, as $CL_2$ deflects it at the same amount but in the direction opposite to that of $CL_1$. The following relationships are established with an error of 0.1%:

$$X_{optical\ axis}(Z_3) = -X_{optical\ axis}(Z_2) = X_{optical\ axis}(Z_1)\,, \tag{2-6a}$$

$$\partial X_{optical\ axis}(Z_3)/\partial Z = \partial X_{optical\ axis}(Z_2)/\partial Z = \partial X_{optical\ axis}(Z_1)/\partial Z = 0\,. \tag{2-6b}$$

These equations and Fig. 2-5a show that the optical axis is symmetric to $Z_2$.

Next, we consider four paraxial rays and an energy dispersive ray for the CL doublet. Fig. 2-5 (b) and (c) show the rays in the X and Y directions, respectively. The initial conditions at $Z_1$ are defined as follows: the offset distances of $x_\alpha$ and $y_\beta$ are 1 μm, the inclined angles of $x_\gamma$ and $y_\delta$ are $3.5e^{-5}$ rad, and the energy difference of $x_\kappa$ is $1e^{-6}$. In the X direction, a parallel ray ($x_\alpha$) is focused on $Z_2$ and exits in parallel again at $Z_3$. The ray is asymmetric to $Z_2$. An inclined ray ($x_\gamma$) is collimated at $Z_2$ and is focused on $Z_3$ again. This ray is symmetric to $Z_2$. These symmetric and asymmetric relationships between the two types of rays are important in canceling higher order aberrations [6]. An energy dispersive ray ($x_\kappa$) is non-zero at $Z_2$ and exits parallel to the optical axis and to the ray $x_\alpha$ at $Z_3$. In the Y direction, a parallel ray ($y_\beta$) remains parallel and an inclined ray ($y_\delta$) is shifted to the off-axis direction twice at each CL center.

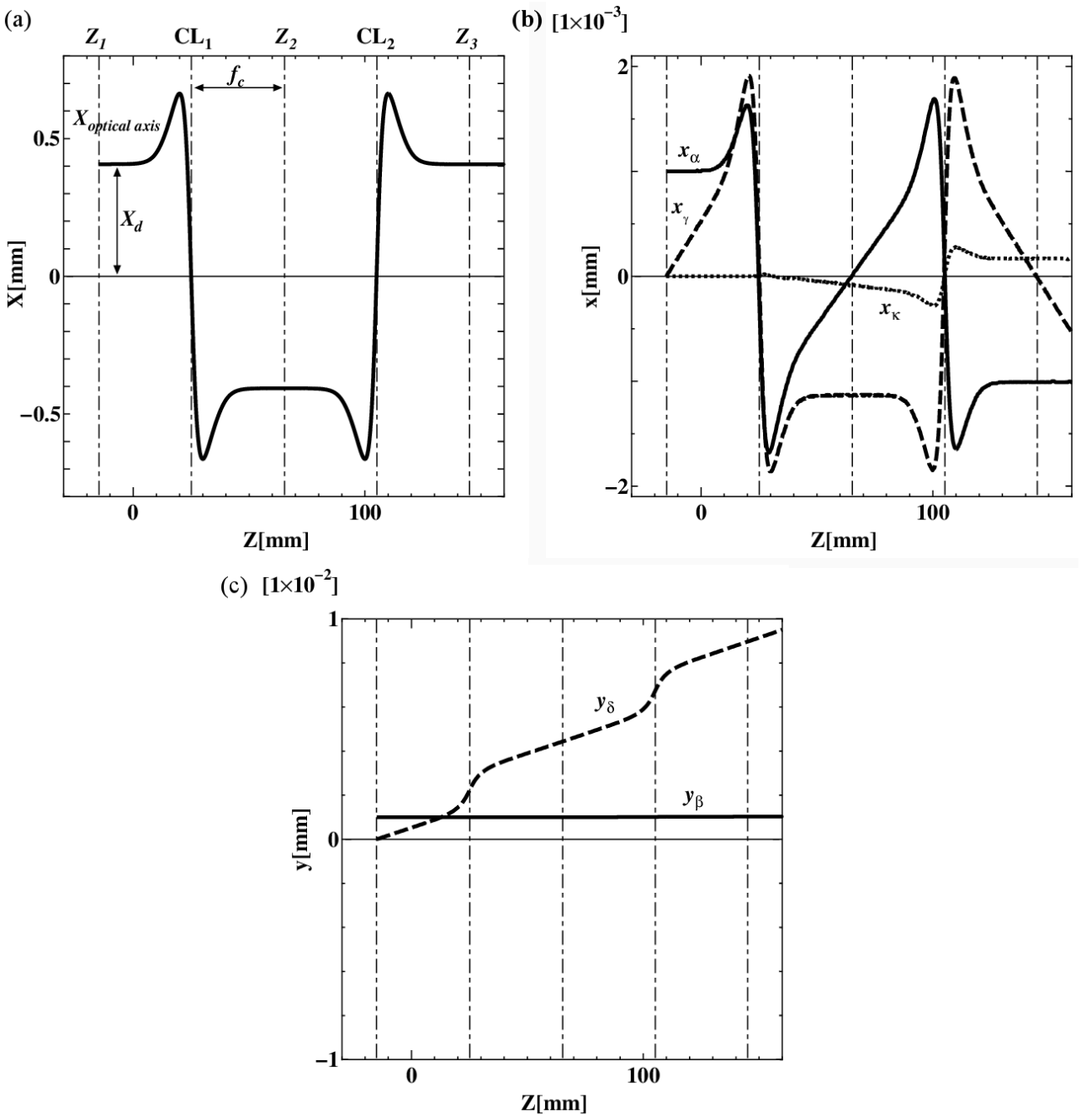


Fig. 2-5 Calculated travesties of (a) optical axis and paraxial rays on (b) the Z-X plane and (c) the Z-Y planes.

The matrix expressions of the CL doublet are derived by multiplication of the first and second CL matrixes, as follows:

$$CLX_{23} \cdot CLX_{12} = \begin{pmatrix} -1 & 0 & -2d \\ 0 & -1 & 0 \\ 0 & 0 & 1 \end{pmatrix}_{13}, \tag{2-7a}$$

$$CLY_{23} \cdot CLY_{12} = \begin{pmatrix} 1 & 4f_c + 2t \\ 0 & 1 \end{pmatrix}_{13}. \quad (2\text{-}7b)$$

The chromatics terms of $CL_2$ have the opposite sign because the deflection direction of $CL_2$ is opposite to that of $CL_1$. To confirm the validity of this, the matrixes of the CL doublet are also derived with the same procedures, as outlined in Table 2-1. The results are shown in Table 2-2.

Table 2-2 Calculated matrix coefficients of the CL doublet.

| $CLX_{23}\,CLX_{12}$ | $(x\|x)$ | $(x\|a)$ | $(x\|\kappa)$ | $(a\|x)$ | $(a\|a)$ | $(a\|\kappa)$ |
|---|---|---|---|---|---|---|
| | −1.00 | −0.02 | 188.14 | 0.00 | −1.00 | 0.00 |
| $CLY_{23}\,CLY_{12}$ | $(y\|y)$ | $(y\|b)$ | $(b\|y)$ | $(b\|b)$ | | |
| | 1.03 | 256.91 | 0 | 1.03 | | |

The multiple correlation factors $R^2$ are high enough to support the reliability of the coefficients. By comparing the values in Table 2-2 with the values from the matrix multiplication in Eqs. (2-7), the maximum error in geometric terms is 2.6%. In chromatic terms, this value is 0.4%. Within these allowable errors, the validity of these matrix expressions is guaranteed.

The matrix in Eq. (2-7a) suggests that the CL doublet serves as a lens with magnification of −1 in the X direction. Eq. (2-7a) shows that the angular dispersion $(a|\kappa)$ vanishes according to the relationship expressed by Eq. (2-4). In the Y direction, Eq. (2-7b) can be interpreted as twice the drift distance of the single CL. In addition, the optics of two CL doublets, CL quadruplets, is investigated as another MC candidate. Its matrix expression can be written as follows:

$$CLX_{45} \cdot CLX_{34} \cdot CLX_{23} \cdot CLX_{12} = \begin{pmatrix} 1 & 0 & 0 \\ 0 & 1 & 0 \\ 0 & 0 & 1 \end{pmatrix}_{15}, \quad (2\text{-}8a)$$

$$CLY_{45} \cdot CLY_{34} \cdot CLY_{23} \cdot CLY_{12} = \begin{pmatrix} 1 & 8f_c + 4t \\ 0 & 1 \end{pmatrix}_{15}. \quad (2\text{-}8b)$$

This matrix shows that the CL quadruplets serves as a lens with magnification of +1 in the X direction. Because both the lateral and angular energy dispersions vanish, this optics is ideal for an MC. However, the total optical length $8f_c$ is too long to locate it in the gun region. Hence, we mainly discuss the MC with the CL doublet.

### 2-4-4 Optical constitution of the monochromator with offset CLs

Here, the new MC is constituted based on the CLs doublet. Fig. 2-1 shows a schematic of its optical configuration. In addition, Fig. 2-6 shows a schematic of the first-order trajectories of the MC. The CL doublet is offset by $X_d$ to the microscope axis in the X direction. From the requirement of an MC to cancel its lateral dispersion, $TL_2$ with a focal length of $f_2$ is located at $Z_3+f_2$. Its front focal plane is coincident to $Z_3$ and its conjugate back focal plane is at $Z_4$. In addition, to construct the conjugate optics with an object-image relationship, another $TL_1$ with a focal length of $f_1$ is located in $Z_1-f_1$. Its back focal plane is coincident to $Z_1$ and its conjugate front focal plane is at $Z_0$. These two transfer lenses are located on the optical axis of the microscope. An emitter of charged particle beams is located at $Z_0$ and emitted rays are collimated by $TL_1$.

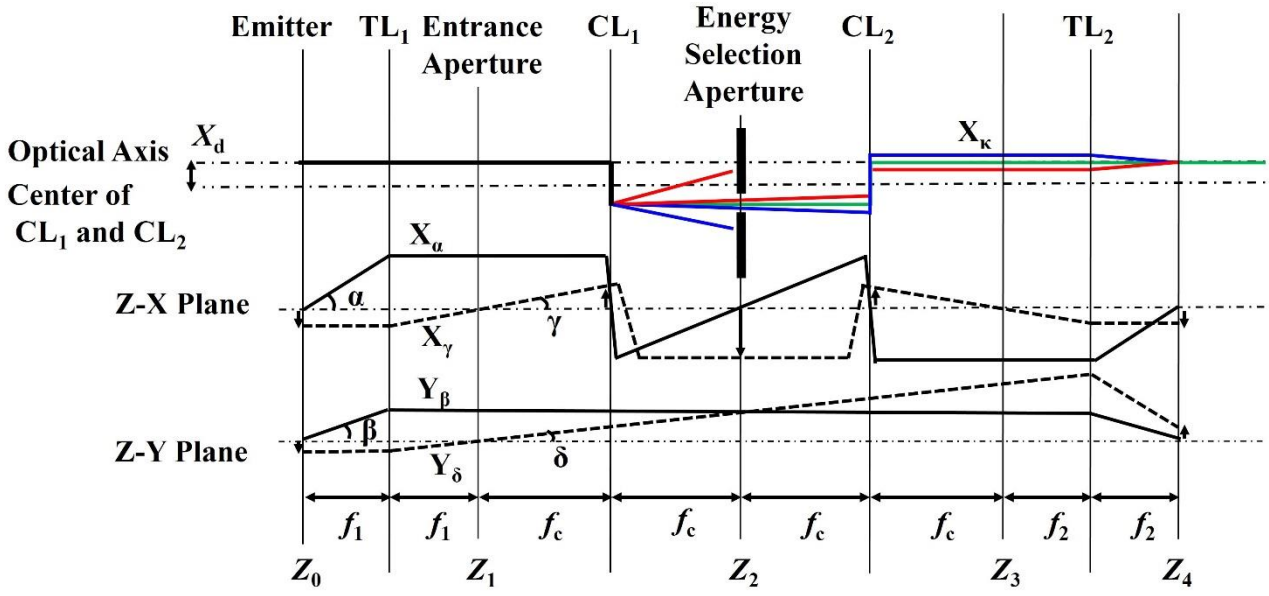


Fig. 2-6 Schematic of the first order trajectories of the MC.

An entrance aperture to define the probe current is placed in $Z_1$. It confines the incident angles without dependency on the incident positions at the emitter. At the same time, it limits lateral deviations from the optical axis at the entrance of the CL doublet. Another aperture for energy selection (ES-AP) is located on the middle plane $Z_2$,

where the energy dispersion $D\kappa$ occurs in the X direction according to $CL_1$. The collimated rays from the emitter are line-focused in the X direction onto the optical axis at $Z_2$. With this aperture, the energy filtering function is realized. The optics is described in the following matrix expressions:

$$TL2_{34} \cdot CLX_{23} \cdot CLX_{12} \cdot TL1_{01} = \begin{pmatrix} f_2/f_1 & 0 & 0 \\ 0 & f_1/f_2 & 2d/f_2 \\ 0 & 0 & 1 \end{pmatrix}_{04}, \tag{2-9a}$$

$$TL2_{34} \cdot CLY_{23} \cdot CLY_{12} \cdot TL1_{01} = \begin{pmatrix} -f_2/f_1 & 0 \\ (4f_c + 2t)/f_1 f_2 & -f_1/f_2 \end{pmatrix}_{04}. \tag{2-9b}$$

By defining the total magnification as $M=f_2/f_1$, these matrixes suggest that the optics serves as a lens which transfers an object in $Z_0$ to its image in $Z_4$ with the magnification of $M$ in the X direction and $-M$ in the Y direction. Furthermore, postulating the optics of a gun MC, it is preferable that the emitter in $Z_0$ is imaged onto the exit plane $Z_4$ with unit magnification, which is achieved by setting $TL_1$ and $TL_2$ at the same excitation. Thus, their focal lengths are expressed as $f_1 = f_2 \equiv f_t$. In the subsequent calculation, a value of $f_t$ is 10 mm. In this condition, the matrixes are written as follows:

$$TL2_{34} \cdot CLX_{23} \cdot CLX_{12} \cdot TL1_{01} = \begin{pmatrix} 1 & 0 & 0 \\ 0 & 1 & 2d/f_t \\ 0 & 0 & 1 \end{pmatrix}_{04}, \tag{2-10a}$$

$$TL2_{34} \cdot CLY_{23} \cdot CLY_{12} \cdot TL1_{01} = \begin{pmatrix} -1 & 0 \\ (4f_c + 2t)/{f_t}^2 & -1 \end{pmatrix}_{04}. \tag{2-10b}$$

This optics transfers an object in $Z_0$ to an image in $Z_4$ stigmatically with the magnification of 1 in the X direction and $-1$ in the Y direction. Additionally, the lateral energy dispersion $(x|\kappa)_{04}$ in the X direction vanishes. Thus, the source image in $Z_4$ can be transferred by the downstream optics of the microscope without energy dispersion. Moreover, this optics is capable of energy filtering on the middle plane $Z_2$, as discussed above. Thus, we conclude that the optics of the CL doublet serves as a MC. After passing through it, charged particle beams with a narrow energy spread and a stigmatic beam shape can be acquired.

From another point of view, the trajectories on the Z-X plane and the Z-Y plane are quite different, as shown

in Fig. 2-6. In this optics, there are three intermediate image planes in the X direction but no image plane in the Y direction. These line-focused images are preferable to reduce electron-electron interactions such as statistical Coulomb effects and Boersch effects, which would occur with a stigmatic focus of a high-intensity beam. Hence, this optical configuration minimizes beam broadening internally.

The two transfer lenses, $TL_1$ and $TL_2$, can also be used to compensate for changes in the emitter's working conditions, such as variations in the extraction voltage, by adjusting their excitations. When the MC is not used, they can also serve as a conventional condenser or as illumination optics.

### 2-4-5 Performance of the new monochromator

In this section, the performance of the new MC is assessed. It includes the contributions of higher order aberrations, in contrast to previous discussions, which were limited to first-order optics. Ray trace calculations are done in the region of two CLs ($Z_1$-$Z_3$), and matrix calculations of the first-order are done in the region from the source to $TL_1$ ($Z_0$-$Z_1$) and in the region from $TL_2$ to the exit plane of the MC ($Z_3$-$Z_4$).

In this study, a Schottky electron emitter is adopted, and the following source parameters are used: a virtual source diameter $d_o$ of 28 nm, an angular current density of 500 μA/sr, and an energy spread of 0.833 eV at the FWHM [7]. In addition, the following initial conditions are adopted: an incident energy $E_0$ of 4 keV, incident currents $I_{in}$ of 100, 300, and 1000 pA, and the number of trajectories of 3000. Every calculation is done under different initial conditions generated randomly within the above conditions. The calculated results provide the beam width on the energy selection plane $Z_2$. Based on the assumption that the width in the X direction corresponds to the energy selection slit width $d_s$, the energy resolution $\delta_\kappa$ is determined by the equation

$$\delta_\kappa = 2d_s/D_k \tag{2-11}$$

with the energy dispersion $D_\kappa$. Assuming that the energy distribution of the emitted electrons is Gaussian with the above energy spread, the proportion of electrons included within the energy range between $E_0$–$\delta_\kappa$/2 and $E_0$+$\delta_\kappa$/2 is calculated. By multiplying this value by the incident current $I_{in}$, the beam current $I_{out}$ at the exit of the MC can be calculated. These calculated results are summarized in Table 2-3. For a relatively large current $I_{out}$ of 50.4 pA, an energy resolution of 34 meV can be achieved. By decreasing the incident current, the energy resolution improves. This MC can achieve an energy resolution below 10 meV. These results suggest the potential of this optics as a high-

performance MC.

Table 2-3 The performance of the MC.

| Condition | Incident current $I_{in}$ (pA) | Exit current $I_{out}$ (pA) | Slit width $d_s$ (nm) | Energy resolution $\delta_K$ (meV) |
|---|---|---|---|---|
| 1 | 100 | 1.7 | 110 | 9.4 |
| 2 | 300 | 7.1 | 180 | 15.4 |
| 3 | 1000 | 50.4 | 390 | 33.5 |

Furthermore, the beam profiles at the incident energy $E_0$ are reconstructed from various trajectories of which the $x$ and $y$ positions are retrieved at specified $Z$ positions. Additional beam profiles are also calculated in two conditions in which these energies deviate from the reference energy $E_0$ by half of the energy resolution (positive and negative, i.e., $E_0+\delta_K/2$ and $E_0-\delta_K/2$). These profiles for condition No. 2 in Table 2-3 are shown in Fig. 2-7.

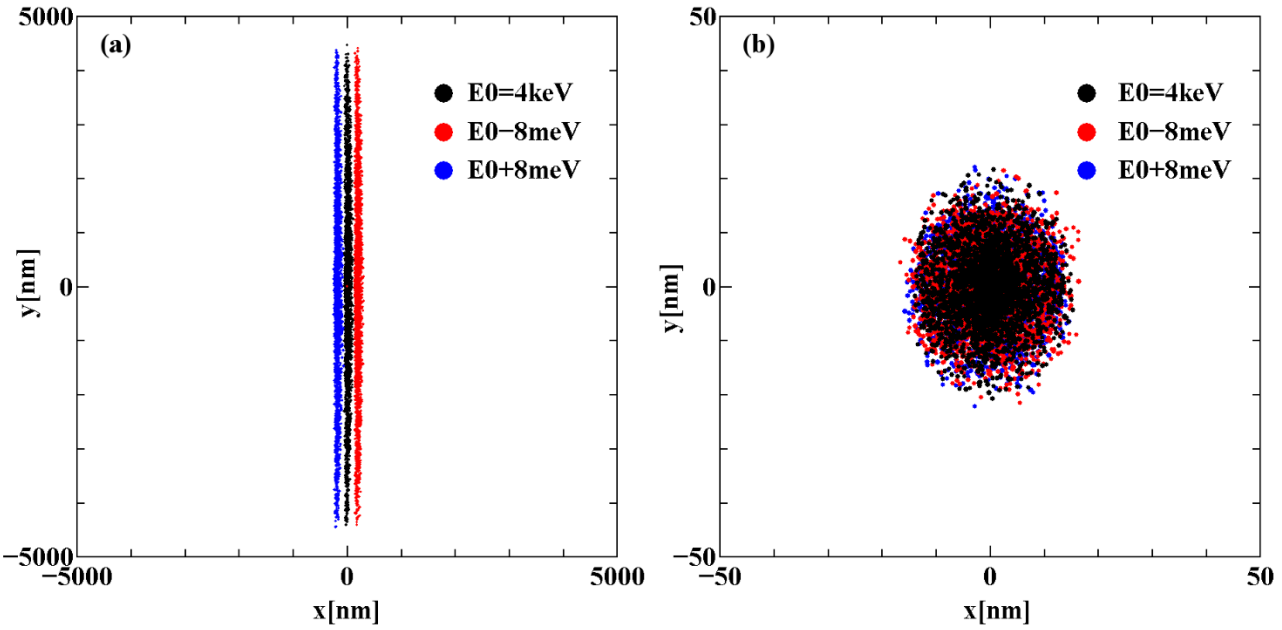


Fig. 2-7 Beam profiles on (a) the middle plane $Z_2$ and (b) the exit plane $Z_4$.

On the middle plane $Z_2$, beams are line-focused and energy-dispersed in the X direction. By inserting a slit

with a width of $d_s$, the energy selection function can be realized. These triangular shapes are caused by second-order aberrations. At the exit plane $Z_4$, beams are focused stigmatically and these distributions are nearly equivalent to the incident source diameter $d_o$. The beam shapes have no triangular asymmetry due to cancellation of the second-order aberrations. In addition, the centers of the beam distributions with different energies are coincident, meaning that the lateral energy dispersion vanishes on the final plane. Three beams show similar but slightly different profiles due to chromatic aberrations. These results show the capability of this optics as an MC more clearly.

### 2-4-6 Mechanical tolerances of the new monochromator

As a guideline for its practical design, the mechanical tolerances of the MC are investigated. These tolerances cause additional parasitic aberrations, increase the beam sizes, and deteriorate the performances such as the energy resolution. As an example, we consider a misalignment of an electrode from the center axis of the MC, which causes a lateral displacement and blurring of the beam. The center electrode of the $CL_1$ is chosen as the misaligned one because it degrades the MC performance more. We simulate the deterioration in beam performances at the two planes of $Z_2$ and $Z_4$ using ten simulation models with X-direction misalignments in 1 μm steps up to 10 μm. The calculated beam condition is No. 2 in Table 2-3, and the other simulation conditions are identical to those above. The calculated lateral displacements show linear dependency on the misalignments. A misalignment of 1 μm results in displacements of 280 nm at $Z_2$ and 800 nm at $Z_4$. The initial adjustment of the offset distance $X_d$ can compensate the displacements partly. Additionally, the misalignments cause asymmetric beam profiles in the +X direction at both at $Z_2$ and $Z_4$. Fig. 2-8 shows the calculated beam widths at the two planes. For a 5 μm misalignment, the beam width becomes twice as large compared to the ideal case at $Z_2$; hence, the energy resolution also worsens by twice as much. At $Z_4$, the beam width doubles for a 7 μm misalignment. Although more accurate assembling is necessary for higher energy resolutions, the results in this section provide quantitative standards for the manufacturing of the MC. We point out that an MC with the CLs still has the advantage of a better assembly process than that of MCs with multipoles, as the CLs consist of plate-shaped electrodes without separations in the azimuth directions.

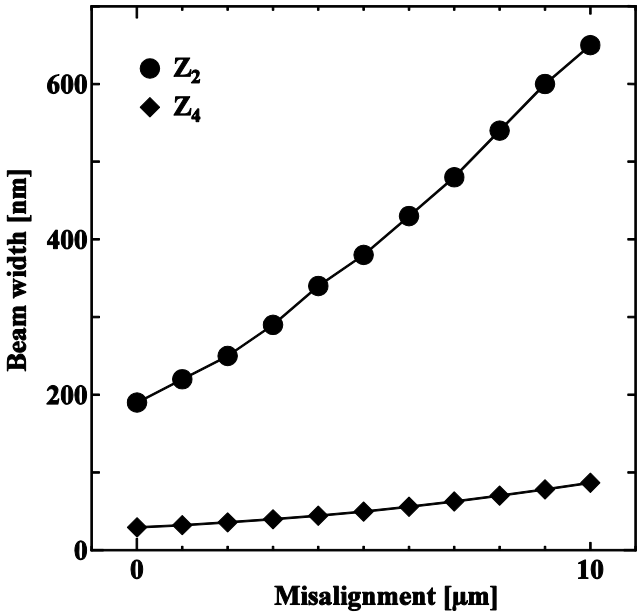


Fig. 2-8 Beam widths dependency on the misalignment of $Z_2$ and $Z_4$.

## 2-5 Advantages of the new monochromator

The advantages of the MC are summarized in this section.

1. A high energy resolution

   Due to its large energy dispersion, high energy resolution is achieved. With the optimum slit, an electron beam with an energy spread below 10 meV is achieved.

2. A simple mechanical configuration without multi-pole optics

   Through the use of CLs for the deflection, the mechanical structures, electronics, and control units can be simplified compared to other MCs with complicated multi-pole optics [8-11].

3. The use of the central part of the beams from the electron source

   In previous MCs using a modified condenser lens, beams from the off-axis region of the electron emitter are used [12, 13]. By using the offset CLs on the emitter axis, this MC enables the use of the central part of the beams from the emitter. This improves the stability of the beam currents and the symmetry of the beam profiles.

4. Pure electrostatic (nonmagnetic) optics

   This MC can be used with an ion beam, as its pure electrostatic optics has no mass dispersion. On the other hand, the mass dispersion causes problems for MCs that rely on magnetic deflection [8-10]. In addition,

the proposed MC more easily achieves a good vacuum condition than magnetic MCs because its electrodes release less outgas than magnetic deflectors with coils. Thus, this MC is suitable for use in an electron gun region requiring UHV or XHV conditions. Furthermore, a quick response and good reproducibility are achieved owing to the small hysteresis effect of the electrostatic lenses. It is also suitable for the rapid turning on and off of the MC.

5. Astigmatic imaging inside the MC

This MC has three images in the X direction but no image in the Y direction. These astigmatic images are favorable for reducing the beam blur caused by electron-electron interactions.

6. Linear optics

This MC can be installed within the microscope's column due to its linear optics. This offers high mechanical stiffness and accurate alignment to other optics. Further, conventional optics can be used simply by turning off the MC and changing the aperture position if higher beam currents are needed.

## 2-6 Conclusion

In this chapter, an optical axis and first-order matrix expressions for a single offset CL are derived from various ray trace simulations. Based on the matrix expressions, a new MC with multiple offset CLs is constituted. The MC shows line focus and energy dispersions in the middle plane and takes a stigmatic and non-dispersive image of the emitter with unit magnification at the exit plane. The energy resolving performance and the mechanical tolerance of the MC are estimated.

## Reference

[1] G. Möllenstedt, Optik 5 (1949) 499.

[2] A.J.F. Metherell, M.J. Whelan, J. Appl. Phys. 37 (4) (1966) 1737.

[3] H. Wollnik, "*Optics of Charged Particles*", (Academic Press, Orlando, 1987).

[4] M. Yavor, "Optics of Charged Particle Analyzers, Advances in Imaging and Electron Physics, Volume 157", (Academic Press, Amsterdam, 2009).

[5] J.W. Goodman, "*Introduction to Fourier Optics*", 3rd ed., (Roberts & Company Publishers, Greenwood Village, 2005).

[6] H. Rose, Optik 51 (1978) 15.

[7] G.A. Schwind, G. Magera, L.W. Swanson, J. Vac. Sci. Tech. B 24 (6) (2006) 2897.

[8] H.W. Mook, P. Kruit, Ultramicroscopy 81 (2000) 129.

[9] P.C. Tiemeijer, Ultramicroscopy 78 (1999) 53.

[10] M. Mukai, W. Inami, K. Omoto, T. Kaneyama, T. Tomita, K. Tsuno, M. Terauchi, K. Tsuda, M. Naruse, T. Honda, M. Tanaka, Microsc. Microanal. 12 (Suppl. 2) (2006) 1206CD.

[11] H. Rose, Ultramicroscopy 78 (1999) 13.

[12] A. Henstra, J. Chmelik, T. Dingle, A. Mangnus, G. van Veen, Microsc. Microanal, 15 (Suppl. 2) (2009) 168.

[13] R.J. Young, G.N.A. van Veen, A. Henstra, L. Tuma, "*Low Voltage Electron Microscopy: Principles and Applications*", edited by D.C. Bell, N. Erdman, (John Wiley & Sons, West Sussex, 2012), 57.

# Chapter 3 Higher Order Aberration of the Monochromator with Offset Cylindrical Lenses

## 3-1 Introduction

In this chapter, theoretical investigation continues and a complementary discussion of the newly proposed monochromator (MC) is offered. Beam profiles will be simulated in an extensive current range by means of a ray trace method. Through a multiple regression analysis, the aberrations of the MC will be derived up to the third order. Next, fundamental performance of the MC, such as the brightness will be estimated, and the results will be applied to various source conditions. The MC and its optics in detail will be discussed in the following sections.

## 3-2 Method

In charged particle optics, aberration coefficients can be derived by the following methods: aberration integrals, differential algebra, and ray tracing. The use of aberration integrals is a traditional and common method, where aberration coefficients are derived by solving aberration integrals with paraxial rays and axial potentials [1]. Berz introduced differential algebra in charged particle optics [2]. Recently, this method has been applied to calculate aberrations in various areas of optics, such as a mirror corrector [3]. Compared with the two methods above, there has been little research on the ray trace method, although Hawkes noted that it can be useful for systems for which the aberration integrals are numerous or very complicated or even unknown [4]. Kasper applied least squares fitting to compute the aberration coefficients by means of a ray trace simulation [5]. Martínez et al. showed that this method has sufficient accuracy on third- and fifth-order aberrations by comparing its results to those of analytical solutions [6]. Van der Stam et al. described a generalized method that can be used in various optical components, including sector magnets [7]. Recently, Lencová et al. developed commercial software that includes the functions of the method [8], and Oral et al. examined its accuracy on the fifth-order aberrations of a two-tube lens [9]. This method became practical only recently because thousands of rays can be calculated in much less time (measured in minutes or even seconds) due to increases in the computation speeds of PCs.

In this chapter, we adopt the ray trace method because the optical axis of the MC passes through a complicated electric field distribution with steep changes in the off-axis region of the CLs. We utilize EO-3D software by MEBS Ltd [10]. This software can compute 3D electrostatic potential distributions for any electrode shapes by the finite

difference method. The accuracy of the potential distributions was confirmed to be 1% or better. The software can derive electron trajectories in the potential distributions by solving the equation of motion directly;

$$\frac{d}{dt}(m\boldsymbol{v}) = -e\boldsymbol{E}, \tag{3-1}$$

where $m$ is the mass of the electron, $\boldsymbol{v}$ is the velocity of the electron, $e$ is the elementary charge, and $\boldsymbol{E}$ is the electrostatic field. With parameters of position ($x$, $y$, $z$) and velocity ($v_x$, $v_y$, $v_z$) of the electron, Eq. (3-1) is considered as six first-order ordinary differential equations. The software solves them with a standard fourth-order Runge-Kutta formula, and the solution algorithm was confirmed to be stable, accurate and reliable.

Our simulation method can be described as follows. Initially, the initial conditions of the positions, angles, and energies are randomly generated within specified ranges. For each initial condition, the ray of an electron beam is simulated by the ray trace method. From the trajectories, a number of positions ($x$ and $y$) of particles are read out at specified $Z$ positions as outputs. As a result, the relationships between the initial conditions and the outputs are acquired. Considering the geometric symmetry of the optics, the types of aberrations are determined. This is done because some coefficients are canceled due to the symmetry. In this study, we adopt the definition of aberrations by Wollnix [11]. By submitting the initial conditions into functions of these aberrations, explanatory variables are calculated. The outputs are considered as response variables. By applying a multiple regression analysis to these variables, the aberration coefficients of the MC are obtained. Here, we use the statistical tools available in Microsoft Excel. Based on statistical significance levels and contribution amounts, the dominant aberration coefficients are selected. This is a brief outline of the method used to calculate the aberrations of the MC.

## 3-3 Results

### 3-3-1 Beam profiles with the MC

In the previous chapter, we proposed a new MC with multiple offset CLs. A CL consists of three electrodes with rectangular openings in the center. In a similar way to our previous chapter, we adopt the ray-tracing method for the CLs in the region of $Z_1$-$Z_3$, which are difficult to be treated in a conventional manner, and utilize first-order matrices for the TLs in the regions of $Z_0$-$Z_1$ and $Z_3$-$Z_4$. For the simulations, the following initial parameters are adopted: incident energy $E_0$, incident currents $I_{in}$, and a number of trajectories $n$. In the succeeding simulations, we

adopt a Schottky electron emitter (SE) with the following source parameters: virtual source diameter $d_0$, angular current density $I'$, FWHM energy spread $\delta E_0$, and reduced brightness $B_r$ [12]. Table 3-1 summarizes these values for the initial conditions and source parameters. We expand the range of the incident currents from those in the previous chapter.

Table 3-1 Simulation conditions.

| Incident energy $E_0$ keV | Incident currents $I_{in}$ nA | Number of trajectories $n$ | Angular current density $I'$ μA/sr | Energy spread $\delta E_0$ eV | Virtual source diameter $d_0$ nm | Reduced Brightness $B_r$ A/m$^2$ sr V |
|---|---|---|---|---|---|---|
| 4 | 0.01, 0.1, 0.3, 1, 3, 10 | 1000, 3000 | 500 | 0.833 | 28 | $1.47 \times 10^8$ |

We simulate the beam profiles by ray trace methods on the above conditions. Fig. 3-1 shows histograms of these beam profiles in two planes. Fig. 3-1 (a) shows those in the X direction on the energy selection plane $Z_2$ and Fig. 3-1 (b) shows those in the X and Y directions on the exit image plane $Z_4$. The incident currents $I_{in}$ are 10 pA and 3 nA. The bin widths of the histograms are 10 nm for (a) and 5 nm for (b). Every simulation is done under an identical condition with regard to the total number of electrons, 1000, for a proper comparison. The Gaussian fittings are also shown as lines in each condition. The lower current condition of 10 pA shows sharp peaks that are well fitted to Gaussian distributions on both planes. Additionally, the two distributions are identical in the X and Y directions at $Z_4$. Therefore, this result denotes the Gaussian and stigmatic imaging of the source at $Z_4$. However, the higher current condition of 3 nA shows dull peaks with broader tails. The histogram at $Z_2$ shows asymmetric distributions in the +X direction, which may arise from second-order aberrations. At $Z_4$, the distributions become symmetric in both the X and Y directions. The histogram in the X direction shows that the center portion of the peak is well fitted to a Gaussian distribution, but its broad tail with a low signal level deviates from the fitting. Given its symmetry, this may stem from third-order aberrations. In the Y direction, the height of the peak is lower than 10 pA, but it is also well fitted to a Gaussian distribution. This may be due to the first-order focusing properties. Here, we roughly estimated these dominant aberrations on the two planes from the shapes of the histograms. In the next sections, these aberrations will be determined precisely and quantitatively.

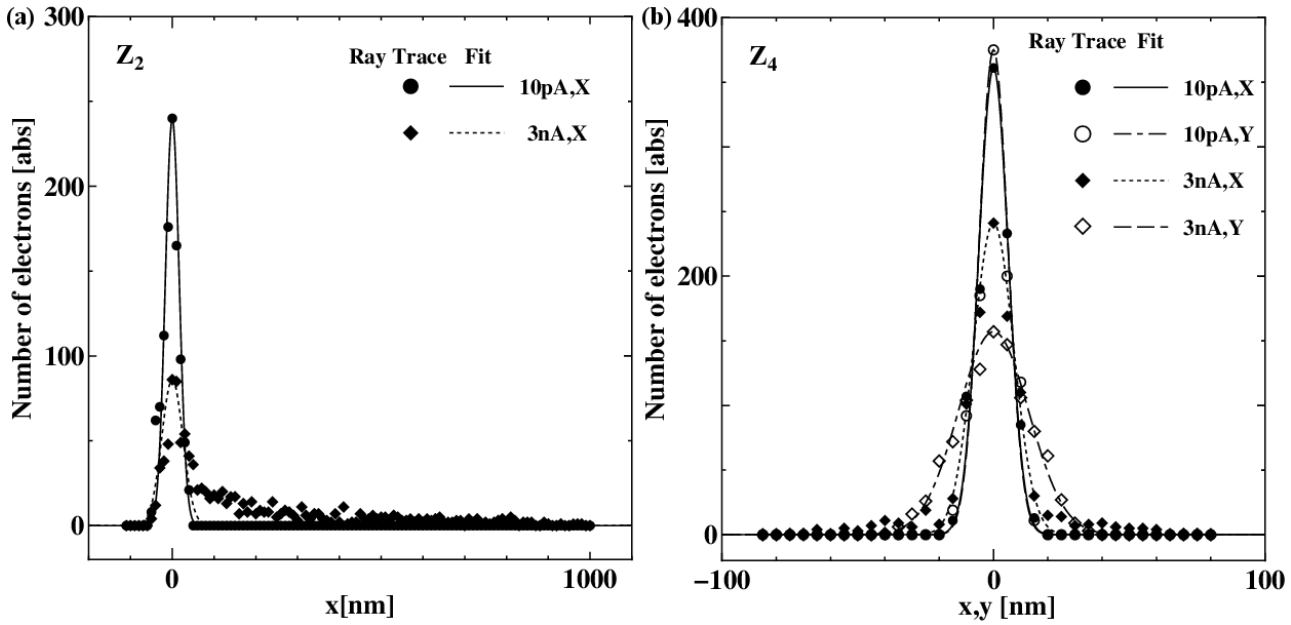


Fig. 3-1 Beam profiles (a) in the X direction at $Z_2$ and (b) in the X and Y directions at $Z_4$.

### 3-3-2 Calculation of aberrations

We derive the aberration coefficients through a multiple regression analysis applied to the results of the ray trace simulations. Initially, we describe the independent variants of $\alpha$, $\beta$, $\gamma$, $\delta$, and $\kappa$, as follows. From Fig. 2-6, the parameters of $\alpha$ and $\beta$ correspond to half angles from the emitter at $Z_0$ in the X and Y direction, respectively. The maximum values of $\alpha$ and $\beta$ are limited by the entrance aperture, which is located on the back focal plane, $Z_1$, of $TL_1$. The ranges of $\alpha$ and $\beta$ are defined by the following equation with the incident current $I_{in}$ into the MC and the angular current density $I'$ of the emitter.

$$\alpha^2 + \beta^2 \leq I_{in}/\pi I'. \tag{3-2}$$

The parameters of $\gamma$ and $\delta$ correspond to the half angles at $Z_1$, and they depend on the lateral positions of the emitter at $Z_0$. The maximum values of $\gamma$ and $\delta$ are defined by the virtual source diameter $d_o$ of the emitter. The ranges of $\gamma$ and $\delta$ are expressed using the following equation with the focal length, $f_1$, of $TL_1$.

$$\gamma^2 + \delta^2 \leq (d_0 /2f_1)^2. \tag{3-3}$$

The parameter $\kappa$ denotes the energy deviation, which is determined by the following equation with the incident energy $E_0$ and an energy difference $\delta E$.

$$\kappa = \delta E / E_0. \tag{3-4}$$

The range of $\kappa$ is determined superposing the energy distribution of the emitter as Gaussian with an FWHM energy spread of $\delta E_0$.

A thousand initial condition sets ($\alpha$, $\beta$, $\gamma$, $\delta$, and $\kappa$) are randomly generated within these ranges of Eqs. (3-2, 3, and 4). The trajectories are then calculated by the ray trace method for these sets. From the trajectories, the particle positions are extracted on two planes, $Z_2$ and $Z_4$, which are written as ($x_2$, $y_2$, $Z_2$) and ($x_4$, $y_4$, $Z_4$). For each plane, a thousand correlations between the initial conditions and the output positions are acquired. By applying a multiple regression analysis to these correlations, the aberration coefficients are derived up to the third order. Considering the geometric symmetry of the optics, types of aberrations are determined. Due to the twofold symmetry in the Y direction of this MC, all aberration coefficients in the X direction should be symmetric, and all coefficients in the Y direction should be asymmetric, with regard to the parameters $\beta$ and $\delta$. Based on the definitions of Wollnik [11], the aberrations of the MC can be written as follows:

$$x = (x|\alpha)\alpha+(x|\gamma)\gamma+(x|\kappa)\kappa+(x|\alpha^2)\alpha^2+\cdots+(x|\kappa^2)\kappa^2+(x|\alpha^3)\alpha^3+\cdots+(x|\kappa^3)\kappa^3, \tag{3-5a}$$

$$y = (y|\beta)\beta+(y|\delta)\delta+(y|\alpha\beta)\alpha\beta+\cdots+(y|\delta\kappa)\delta\kappa+(y|\beta^3)\beta^3+\cdots+(y|\beta\kappa^2)\beta\kappa^2. \tag{3-5b}$$

In this study, our main interest is the dependencies of the MC performance on the incident current $I_{in}$. The dominant contributions to third order aberrations are attributed to increases in the currents, or the incident angles of $\alpha$ and $\beta$. Thus, we take into account third-order aberration coefficients, including $\alpha$, $\beta$, and $\kappa$, and ignore those with $\gamma$ and $\delta$ due to their low levels of influence. By substituting the initial conditions into these aberration functions, for example $\alpha^2$, in Eqs. (3-5), each explanatory variable is calculated. The output positions of $x$ and $y$ are considered as response variables. The aberration coefficients are calculated by the regression analysis function of Microsoft Excel. The detailed analysis procedure is as follows. We define the significance level as 95% and the number of significance as 1000. The aberration coefficients are adopted when they satisfy conditions in which the p-values are less than 5%

and the t-values are greater than 2. The regression analysis is repeated until all coefficients satisfy the above conditions. Furthermore, coefficients whose t-values rank in the top fifth are selected. The t-value denotes the influence of the coefficient on the total beam width. For the analysis, the worst multiple correlation factor is 99.73%. This value is high enough to support the reliability of these coefficients.

The geometric aberrations are acquired under the condition in which the energy divination $\kappa$ is 0, or the energies of all electrons are identical to the incident energy $E_0$. The energy dispersions and chromatic aberrations are obtained, where the FWHM energy spread $\delta E_0$ is 0.833 eV. Applying the above analysis procedure, we calculate the aberration coefficients in six incident current conditions: $I_{in}$ =10, 100, and 300 pA, and 1, 3, and 10 nA. After comparing these results, we select the aberration coefficients for $I_{in}$ of 1 nA, which corresponds to an intermediate value in the current ranges. Table 3-2 summaries the aberration coefficients in the X and Y directions on the two planes, $Z_2$ and $Z_4$.

Table 3-2 The aberration coefficients of the MC at $Z_2$ and $Z_4$.

| Type | Function | Coefficients | | | |
|---|---|---|---|---|---|
| | | $Z_2$ plane | | $Z_4$ plane | |
| | | *X* | *Y* | *X* | *Y* |
| 1st order | (x\|α) | −8.70E−03 | | −2.43E−04 | |
| | (x\|γ) | −3.25E+01 | | −1.00E+01 | |
| | (y\|β) | | 1.00E+01 | | 2.07E−02 |
| | (y\|δ) | | 1.27E+02 | | 1.03E+01 |
| | (x\|κ) | −9.41E+01 | | | |
| 2nd order | (x\|$\alpha^2$) | 5.13E+02 | | 3.60E−01 | |
| | (x\|αγ) | | | 2.03E+03 | |
| | (x\|$\gamma^2$) | −2.15E+06 | | | |
| | (x\|$\beta^2$) | −6.89E+00 | | | |
| | (x\|$\delta^2$) | −2.31E+06 | | | |
| | (y\|αδ) | | | | 1.19E−01 |
| | (x\|ακ) | −2.91E+03 | | 4.23E+03 | |
| | (y\|βκ) | | | | −2.81E−02 |
| | (y\|δκ) | | | | −1.55E+00 |
| | (x\|$\kappa^2$) | 2.36E+03 | | −4.00E+04 | |
| 3rd order | (x\|$\alpha^3$) | | | −2.20E+04 | |
| | (y\|$\beta^3$) | | | | 7.45E−01 |
| | (x\|$\alpha^2\kappa$) | | | 6.04E+05 | |
| | (y\|$\beta\kappa^2$) | | | | −2.55E+00 |
| | (x\|$\kappa^3$) | | | −9.98E+06 | |

It is important to note that a coefficient in Table 3-2, which takes a smaller value, does not always have a little

influence on the total beam widths. It is necessary to consider the amount of aberration, which is given by multiplying the coefficient by the value from the aberration function, for example, as $(x|\alpha^2)\ \alpha^2$. Specifically, coefficients containing $\alpha$ and $\beta$ have smaller values. However, they could contribute greatly to the total beam widths because $\alpha$ and $\beta$ are more than ten times as large as $\gamma$, $\delta$, and $\kappa$.

Next, the beam profiles are reconstructed from the aberration coefficients in Table 3-2 to confirm the accuracy of these values. We calculate beam positions ($x'$, $y'$) at $Z_2$ and $Z_4$ by substituting initial parameters ($\alpha$', $\beta$', $\gamma$', $\delta$', and $\kappa$') into Eqs. (3-5) together with the coefficients of Table 3-2. These parameters, which are defined by the maximum values of Eqs. (3-2, 3, and 4), are expressed as

$$\alpha' = \sqrt{I_{in}/\pi I'}\cos\theta\,, \beta' = \sqrt{I_{in}/\pi I'}\ \sin\theta,$$

$$\gamma' = d_0\cos\varphi/2f_1\ , \delta' = d_0\ \sin\varphi/2f_1\,, and\ \kappa' = \delta E/E_0. \qquad (3\text{-}6)$$

By changing these parameters in ten-degree steps of the azimuth angles of $\theta$ and $\varphi$, a number of positions ($x'$, $y'$) result in beam profiles. Figs. 3-2 (a) and (b) show these beam profiles generated by the geometric aberration coefficients of Table 3-2 as contour lines at $Z_2$ and $Z_4$, respectively. The beam profiles from the ray trace simulation, of which the number of trajectories is 1000, are also shown as dots. The source parameters are identical to the values in Table 3-1. The colors denote different incident currents $I_{in}$, which are 10, 100, 300 pA, 1 and 3 nA. The corresponding incident angles of $\alpha$' and $\beta$' are $8.0e^{-5}$, $2.5e^{-4}$, $4.4e^{-4}$, $8.0e^{-4}$, and $1.4e^{-3}$ rad from Eqs. (3-6). The values of $\gamma'$ and $\delta'$ are $1.4e^{-6}$ rad. The Y scale of Fig. 3-2(a) is 20 times larger than the X scale. In both Fig. 3-2(a) and (b), the beam profiles from the geometric aberration coefficients are coincident with those by the ray tracing method in each current condition. Thus, we confirm the accuracy of the geometric aberrations in Table 3-2. In Fig. 3-2(a), the contours are elliptical at a lower current; they protrude in the +X direction with an increase in the current. The beams, which correspond to the position of the –X region, are folded in the +X direction. These protrusions become more significant at higher current levels. In the Y direction, the beam profiles are symmetric to the Y axis and are enlarged constantly. In Fig. 3-2(b), the beam profiles expand in the Y direction in the lower current regions. For current higher than 1 nA, the beam profiles grow steeply in the X direction. The beam profiles shown in Fig. 3-2 (b) are symmetric with the X direction, in contrast to those in Fig. 3-2 (a).

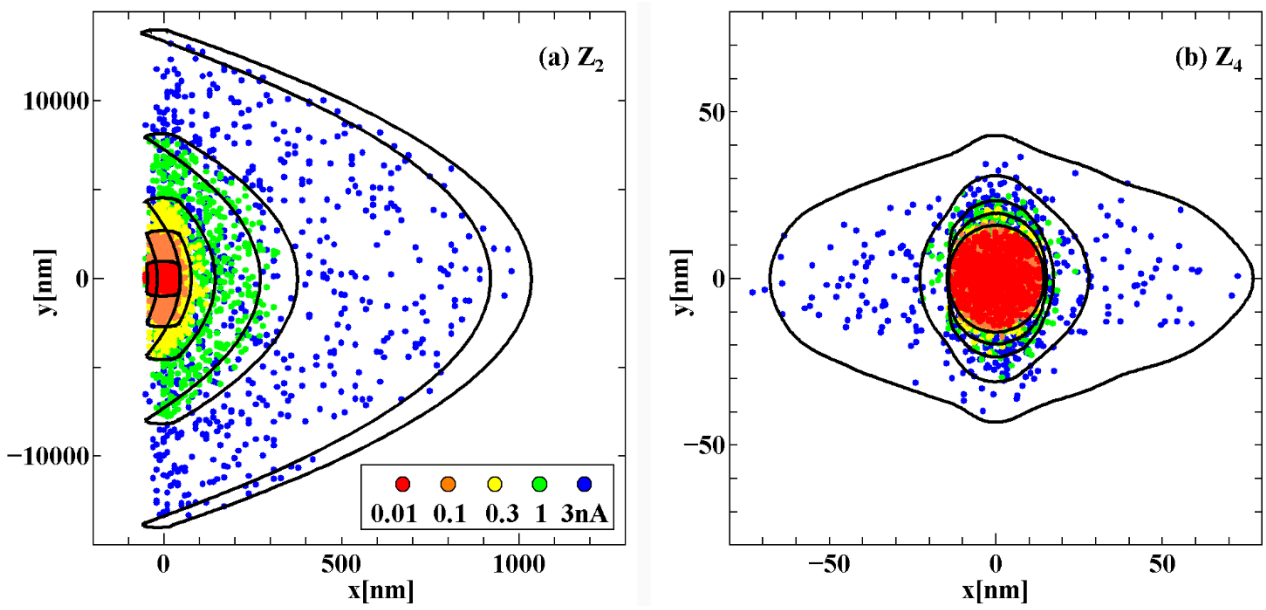


Fig. 3-2 Beam profiles with beam current differences at (a) $Z_2$ and (b) $Z_4$.

Next, we discuss the chromatic aberrations. Figs. 3-3 (a-d) show the beam profiles generated by the chromatic and geometric aberrations in Table 3-2 in contour lines. Fig. 3-3 (a) represents the beam profiles at $Z_2$, and Figs. 3-3 (b-d) show those at $Z_4$. The color differences show three energy conditions, i.e., $E_0$, $E_0$+25 meV, and $E_0$−25 meV, where $E_0$ is 4 keV. The incident current $I_{in}$ is 1 nA. The results of the ray trace simulation are also shown as distributions of dots. The number of trajectories is 3000. The source parameters are described in Table 3-1. Eqs. (3-6) give the initial parameters as follows: $\alpha$', $\beta$'=8.0e$^{-4}$ rad, $\gamma$', $\delta$'=1.4e$^{-6}$ rad, and $\kappa$'=0, +6.3e$^{-6}$, and -6.3e$^{-6}$.

In Figs. 3-3 (a-d), the contours by the chromatic and geometric aberrations are equivalent to those by the ray traces. Hence, the accuracy of the chromatic terms in Table 3-2 is also confirmed. In Fig. 3-3 (a), the lateral shifts of three profiles, caused by the energy dispersion term ($x|\kappa$), are suitably reproduced. In Figs. 3-3 (b-d), the center points of the profiles are around (0, 0); i.e. they correspond to the optical axis. This stems from the fact that ($x|\kappa$) is 0 on the exit image plane $Z_4$, which implies a lateral dispersion-free condition. These three contours change due to chromatic aberrations according to the energy differences. Considering Figs. 3-2 and Figs. 3-3, we confirm the accuracy of the aberration coefficients in Table 3-2.

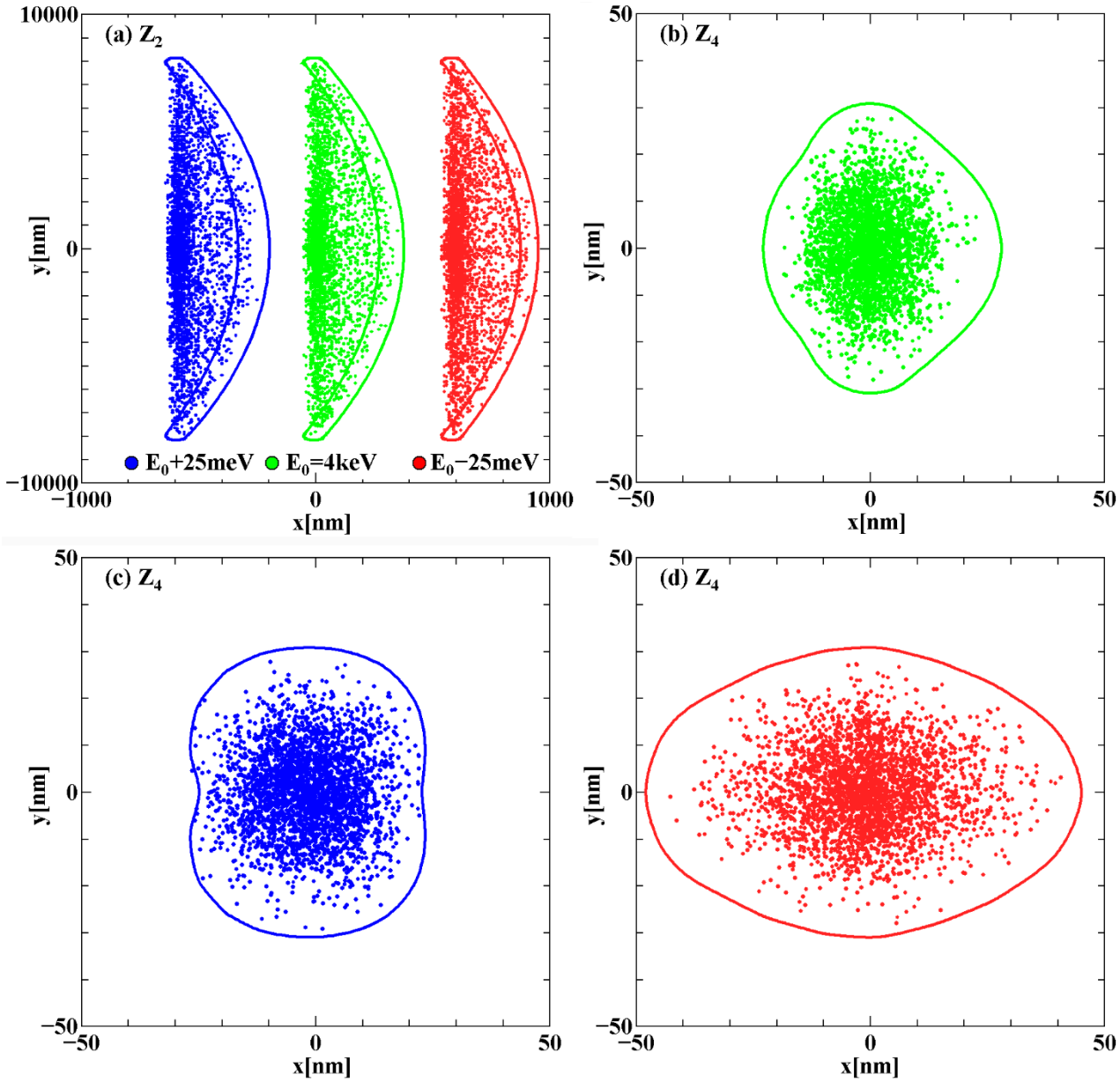


Fig. 3-3 Beam profiles with energy differences at (a) $Z_2$ and (b-d) $Z_4$.

Further investigating the influence of the aberration coefficients on these beam profiles, we calculate the amounts of aberration. Table 3-3 shows the results with an incident current $I_{in}$ of 1 nA and an energy difference $\delta E$ of+25 meV at the two planes of $Z_2$ and $Z_4$. The initial parameters are as follows: $\alpha$', $\beta$'=8.0e$^{-4}$ rad, $\gamma$', $\delta$'=1.4e$^{-6}$ rad, and $\kappa$'=+6.3e$^{-6}$. Table 3-3 shows these amounts of aberrations in the following two positions on each plane. The columns of $+X_{max}$ show the aberration amounts of the X direction in a position where the beam profiles are maximized in the +X direction. The columns of $+Y_{max}$ are similar in the +Y directions. The conditions in Table 3-3 correspond to the contours in blue at $Z_2$ in Fig. 3-3(a), and at $Z_4$ in Fig. 3-3(c). The symbols of S and A in Table 3-3 refer to

symmetry and asymmetry respectively, with regard to the X or Y axis. The symmetric terms contribute to the offset of the beam profile contours, and the asymmetric terms contribute to the widths of the contours. Similarly, we calculate the amounts of aberration in the conditions with energy differences of 0 and −25 meV.

Table 3-3 The amounts of aberration.

| Type | Function | Amounts | | | | | | | |
|---|---|---|---|---|---|---|---|---|---|
| | | $Z_2$ plane | | | | $Z_4$ plane | | | |
| | | $+X_{max}$ | | $+Y_{max}$ | | $+X_{max}$ | | $+Y_{max}$ | |
| 1st order | (x\|α) | 7 | A | | | | | | |
| | (x\|γ) | 46 | A | | | 14 | A | | |
| | (y\|β) | | | 7983 | A | | | 17 | A |
| | (y\|δ) | | | 178 | A | | | 14 | A |
| | (x\|κ) | −588 | S | | | | | | |
| 2nd order | (x\|$\alpha^2$) | 327 | S | | | | | | |
| | (x\|αγ) | | | | | −2 | S | | |
| | (x\|$\gamma^2$) | −4 | S | | | | | | |
| | (x\|$\beta^2$) | | | | | | | | |
| | (x\|$\delta^2$) | | | | | | | | |
| | (y\|αδ) | | | | | | | | |
| | (x\|ακ) | 15 | A | | | 21 | A | | |
| | (y\|βκ) | | | | | | | | |
| | (y\|δκ) | | | | | | | | |
| | (x\|$\kappa^2$) | | | | | −2 | A | | |
| 3rd order | (x\|$\alpha^3$) | | | | | −11 | A | | |
| | (y\|$\beta^3$) | | | | | | | | |
| | (x\|$\alpha^2\kappa$) | | | | | 2 | S | | |
| | (y\|$\beta\kappa^2$) | | | | | | | | |
| | (x\|$\kappa^3$) | | | | | | | | |
| Total | $X_{max}$ or $Y_{max}$ | −199 | | 8161 | | 23 | | 31 | |

First, we discuss the amounts of geometric aberration, as shown in Table 3-3. On the energy-selecting plane of $Z_2$, the magnified Gaussian image of the virtual source ($x|\gamma$) is 46 nm. The second-order aperture aberration ($x|\alpha^2$) shows a much larger value of 327 nm. This term is symmetric with X and causes protrusions in the +X direction in Fig. 3-2 (a) under large current conditions. This term results in asymmetric beam tails in the +X direction. On the exit plane $Z_4$, this term ($x|\alpha^2$) becomes negligible. The symmetric configuration of the optics and potential and the symmetric and asymmetric fundamental rays result in the cancelation of this second-order aperture aberration, which is often used in imaging energy filters [13]. The Gaussian image of the source ($x|\gamma$) is 14 nm, indicating image

formation with a unit magnification at $Z_4$. The third-order aperture aberration ($x|\alpha^3$) is the second largest value of 11 nm in the geometric aberrations; this causes a rapid increase in the X directions, as shown in Fig. 3-2 (b). The term ($x|\alpha\gamma$) causes slight asymmetry of the beam distributions in Fig. 3-2 (b). In the Y direction, the term ($y|\beta$) is dominant at $Z_2$ due to the non-focusing condition. It increases in proportion to $\beta$ with an increase in the incident current. At $Z_4$, ($y|\delta$) term is coincident with ($x|\gamma$), indicating stigmatic imaging of the source with a unit magnification. The term ($y|\beta$), which is the first-order aperture aberration of $\beta$, shows a larger value of 17 nm. This causes an increase in the beam profiles in the Y direction for the low current conditions shown in Fig. 3-2(b).

Next, we discuss the chromatic terms, including the energy deviation of $\kappa$, in Table 3-3. At $Z_2$, the term ($x|\kappa$) has the largest amount of aberration. Because it depends only on $\kappa$, this term causes shifts of the optical axis due to energy deviations, as shown in Fig. 3-3 (a). The largest value indicates that beam distributions with the energy deviations are completely separated. A negative sign indicates that higher energy beams, which are difficult to deflect, are located on the negative side from the optical axis of the zero-loss beams. At $Z_4$, the term ($x|\kappa$) is negligible, which means that this optics exists in a lateral dispersion-free condition, as described above. At $Z_2$, ($x|\alpha\kappa$) is the second largest chromatic aberration value. This is the first-order and first-degree chromatic aberration. Compared to the zero-loss beam of $\kappa$=0, this term enlarges the beam distribution of +25 meV and reduces that of −25 meV. This effect can be observed in the width of the contours on the X-axis, where Y is 0, as shown in Fig. 3-3 (a). Similarly, ($x|\alpha\kappa$) is the largest value at $Z_4$. For the beam distribution of +25 meV, ($x|\alpha\kappa$) shows a sign opposite that of ($x|\alpha^3$). Thus, the width of the beam distribution on the X-axis in Fig. 3-3(c) is reduced against the zero-loss beam in Fig. 3-3(b). Conversely, ($x|\alpha\kappa$) and ($x|\alpha^3$) take the same sign for −25 meV beams. This enlarges the width at the X-axis of Fig. 3-3(d). ($x|\kappa^2$) of the second order and ($x|\alpha^2\kappa$) of the third order are nearly equivalent absolute values, but with opposite signs. Thus, they make little contribution to the total beam widths.

Given the discussion in this section, we derive the aberration coefficients of the energy selection plane $Z_2$ and the exit image plane $Z_4$. The reconstructed aberration figures confirm the accuracy of these coefficients. By estimating the amounts of aberration, we clarify these influences on the beam profiles with various conditions of current and energy deviation.

### 3-3-3 MC Performance

In this section, we evaluate the performance of the MC. Based on the aberration coefficients in Table 3-2, we derive the dependency of the beam widths on the incident currents $I_{in}$. The beam widths in the X and Y directions at

$Z_2$ and $Z_4$ can be expressed as follows:

$$dx_{z2} = 2\,(x|\gamma)_{z2}\,\gamma + (x|\alpha^2)_{z2}\,\alpha^2, \tag{3-7a}$$

$$dy_{z2} = 2\,(y|\delta)_{z2}\,\delta + 2\,(y|\beta)_{z2}\,\beta, \tag{3-7b}$$

$$dx_{z4} = 2\,(x|\gamma)_{z4}\,\gamma + 2\,(x|\alpha^3)_{z4}\,\alpha^3, \tag{3-7c}$$

$$dy_{z4} = 2\,(y|\delta)_{z4}\,\delta + 2\,(y|\beta)_{z4}\,\beta. \tag{3-7d}$$

For simplification, we adopt these definitions of the beam widths as the sums of the Gaussian source images and the geometric aberration terms with the largest contribution in each column in Table 3-3. The coefficient of $(x|\alpha^2)$ is 1 due to its symmetry in the X direction, as discussed above. The other coefficients are 2 due to their asymmetry when calculating the beam widths. For an incident current $I_{in}$, Eqs. (3-6) provide the values of $\alpha$ and $\beta$.

Fig. 3-4 shows the dependency of the beam widths by Eqs. (3-7) on the incident currents $I_{in}$ as lines. The beam widths by ray trace simulation are also shown as dots. The source parameters are identical to the values in Table 3-1. The lines and dots fit well in the entire current range of 10 pA to 10 nA. The inclinations of the curves in Fig. 3-4 show the dominant aberration terms at the incident currents. On the energy selection plane $Z_2$, the inclination of $dx_{z2}$ changes at around 100-300 pA, and the second-order aperture aberration $(x|\alpha^2)_{z2}$ becomes the major factor in the high current region. In the Y direction, $dy_{z2}$ shows larger values due to the non-focusing condition on the plane, and its inclination is constant. On the exit plane $Z_4$, $dx_{z4}$ is constant with a value of 28 nm for currents from 10 pA to 300 pA. However, the inclination changes at 1 nA, and the third-order aberration $(x|\alpha^3)_{z4}$ becomes dominant with high currents. $dy_{z4}$ increases constantly, showing larger values even in low current regions due to the first-order term of $(y|\beta)_{z4}$. $dy_{z4}$ is larger than $dx_{z4}$ for currents lower than 1.5 nA. The graph in Fig. 3-4 clarifies the tendency of the beam widths on the incident beam currents, as well as the main aberration terms at the specified currents.

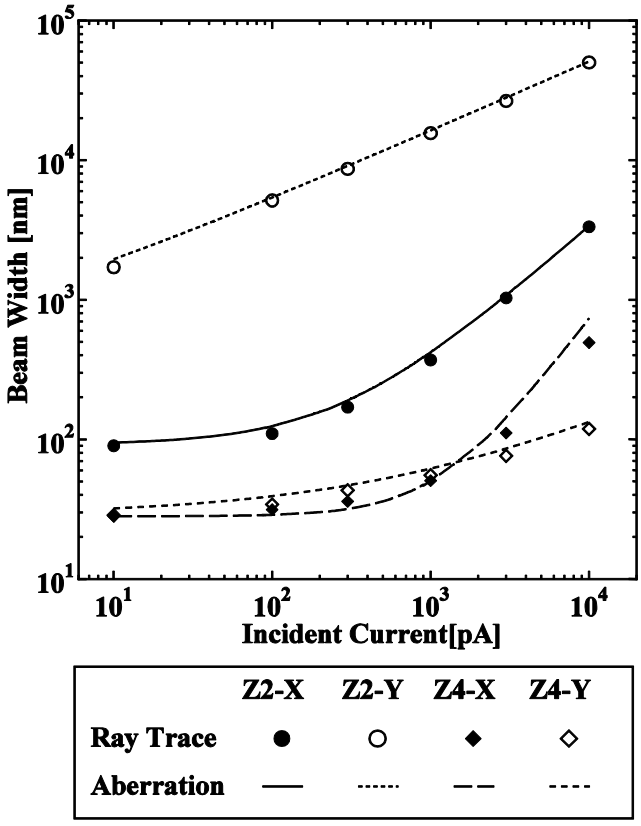


Fig. 3-4 Beam widths dependencies on the incident current in X and Y directions at $Z_2$ and $Z_4$.

Next, we discuss the performance of the MC. The characteristic parameters are the energy dispersion $D_\kappa$, the energy resolution of the MC (or the energy spread of the monochromatic beams at the exit of the MC) $\delta E_{mc}$, the exit current $I_{out}$, and the reduced brightness $B_r$. These are defined by the following equations:

$$D_k = |(x|\kappa)_{Z2}/E_0| = 23.5\ \mu\text{m/eV}, \tag{3-8a}$$

$$\delta E_{mc} = 2\, dx_{z2}/D_k, \tag{3-8b}$$

$$I_{out} = I_{in}/\sqrt{2\pi}\sigma \int_{-\delta E_{mc}/2}^{+\delta E_{mc}/2} exp(-t^2/2\sigma^2)\, dt,\ where\ \sigma = \delta E_0/2\ln(2\sqrt{2}), \tag{3-8c}$$

$$B_r = 4\, I_{out}/\pi\alpha^2 \cdot \pi dx_{z4} dy_{z4} \cdot E_0\,. \tag{3-8d}$$

In Eq. (3-8b), we define the energy resolution $\delta E_{mc}$ as an ideal case such that the width of the energy selection slit is

equivalent to $dx_{z2}$, the beam width at energy selection plane $Z_2$. In Eq. (3-8c), we superpose the energy distribution of the emitter as Gaussian with an FWHM energy spread of $\delta E_0$. Here, $\sigma$ denotes the standard deviation of the corresponding FWHM values. We derive $I_{out}$ of Eq. (3-8c) from the proportion of energy spread $\delta E_{mc}$ to the Gaussian distribution. For the reduced brightness $B_r$ of Eq. (3-8d), we assume that the beam widths include the entire number of electrons on the Gaussian image plane. This is a modest estimation of the brightness. We treat the beam shape as elliptical. Thus, Eq. (3-8d) is expressed with $dx_{z4}$ and $dy_{z4}$. For these beam widths, we take the geometric aberrations of the MC into account, but not the diffraction aberration. It enables to compare the brightness with or without the MC more easily and fairly. For a microscope with the MC, total beam sizes at a specimen, including the diffraction aberration, can be derived by replacing the brightness of the electron source with that of the MC in Eq. (3-8d).

Fig. 3-5 shows the dependencies of these characteristics of the MC on incident current $I_{in}$. The lines show the results generated by the aberrations in Table 3-2. The dots show the results by the ray trace simulation. The lines and dots are in good agreement. The exit current $I_{out}$ increases constantly with incident current $I_{in}$. The energy resolution $\delta E_{mc}$ is constant in the low current region. For current levels that exceed 300 pA, the energy resolution increases in proportional to the incident current. This occurs because the energy resolution is determined by the second-order aperture aberration $(x|\alpha^2)_{z2}\ \alpha^2$ in the higher current region. Moreover, the incident current is proportional to $\alpha^2$. For a practical condition for microscopy observation, the energy resolution is 9.4 meV at an $I_{in}$ of 100 pA and an $I_{out}$ of 1.1 pA. The highest energy resolution of 7.7 meV is achieved at a lower current with $I_{in}$ at 10 pA and $I_{out}$ at 0.09 pA, where the energy-loss spectra are obtained over a longer accumulation time.

Furthermore, Fig. 3-5 presents trends of the reduced brightness $B_r$ from Eq. (3-8d) and the ideal reduced brightness. The latter includes only energy filtering action of the MC but does not contain deterioration caused by the aberrations of the MC. We derive this value with replacing $dx_{z4}\ dy_{z4}$ of Eq. (3-8d) by $d_0^2$. The difference between the two values denotes the loss of the brightness due to the aberrations. The reduced brightness $B_r$ is constant in the lower current region. The brightness suffers the loss from the first-order term of $(y|\beta)_{z4}$. It increases slightly and peaks at a current of 1 nA. As these currents increase, the brightness decreases sharply due to the third-order aberration $(x|\alpha^3)_{z4}$. In the condition with the maximum reduced brightness, the energy resolution is 32 meV and the brightness is $1.6 \times 10^6$ A/sr m$^2$V for $I_{in}$ =1 nA and $I_{out}$ = 36 pA. The graph shown in Fig. 3-5 represents the characteristics of the MC clearly, revealing the aberration terms that limit the performance of the MC.

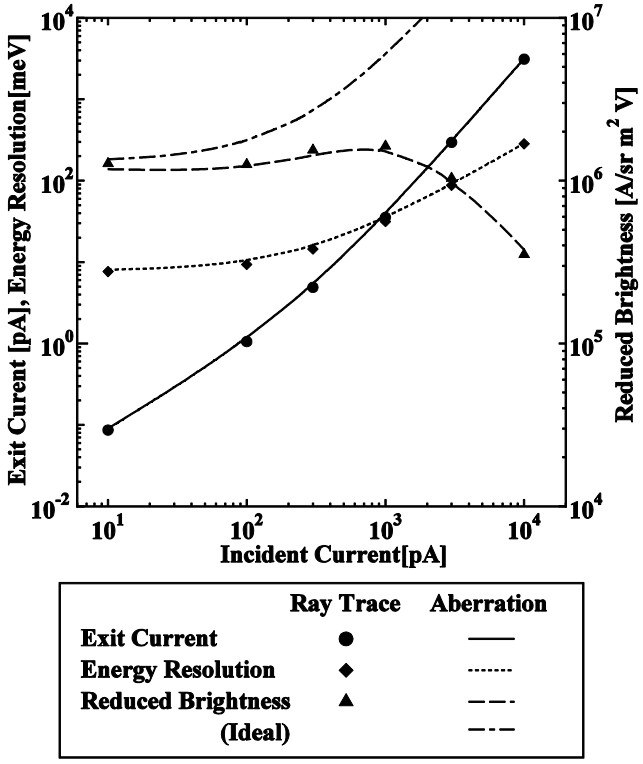


Fig. 3-5 Exit current, energy resolution, and reduced brightness dependencies on incident current.

### 3-3-4 MC performance for various source parameters

The MC characteristic discussed in the previous section is only one solution for one set of source parameters. In actual situations, source parameters change with different applications of microscopes. In addition, the types of emitters are options on microscopes. In previous studies of reference, MCs were utilized together with a Schottky emitter (SE) of ZrO/W (100) and a cold field emitter (CFE) of W (310). Here, we evaluate the MC performance with various source parameters. Table 3-4 summarizes four parameters. No. 1 is for CFE and Nos. 2-4 are for SEs. The previous simulation condition in Table 3-1 corresponds to No. 3 in Table 3-4. The data is cited from Schwind for Nos. 1-3 [12] and from Sakawa for No. 4 [14]. The CFE in No. 1 has the advantages of a smaller virtual source size and energy spread but a disadvantage in its smaller angular current density as compared with the SEs. No. 2 and No. 3 are based on identical SEs with different extraction voltages. No. 2 has a smaller extraction condition, which results in a better energy spread, but a poorer angular current density. No. 2 has the additional advantage of a longer lifetime, typically two years. No. 3 has a higher angular current density due to its higher extraction voltage. No. 4 adopts an SE with a very large tip radius of 4.2 μm, which is eight times larger than those of the conventional SEs in No. 2 and 3. This large tip radius results in a better energy spread due to the reduced Boersch effect in the vicinity of the emitter

surface with an angular current density identical to that of No. 3. The original article by Sakawa did not show the values of the extractor voltage, virtual source size, and brightness. We estimate these values according to Swanson [15]. In No. 4, the large tip radius causes an increase in the virtual source size and a decrease of the brightness.

Table 3-4 The electron source conditions.

| No. | Emitter type | Tip radius $a$ nm | Extraction voltage $V_{ext}$ V | Angular current density $I'$ μA/sr | Energy spread $\delta E_0$ eV | Virtual source diameter $d_0$ nm | Reduced Brightness $B_r$ A/m$^2$ sr V | Ref |
|---|---|---|---|---|---|---|---|---|
| 1 | CFE | 175 | 4300 | 62 | 0.375 | 4 | $1.14 \times 10^9$ | [12] |
| 2 | SE | 550 | 3890 | 220 | 0.700 | 34 | $6.23 \times 10^7$ | [12] |
| 3 | SE | 550 | 5459 | 500 | 0.833 | 28 | $1.47 \times 10^8$ | [12] |
| 4 | SE | 4200 | 14833* | 500 | 0.430 | 130* | $2.55 \times 10^6$* | [14] |

* Estimated values

Next, we evaluate the MC performance levels with these source conditions based on the aberrations in Table 3-2 and Eqs. (3-7 and 3-8). Figs. 3-6 show the energy resolution and reduced brightness dependencies on the exit current in the four source conditions. With regard to the energy resolutions shown in Fig. 3-6 (a), No. 1 with the CFE shows better performance in the low exit current region around 1 pA. This occurs because the virtual source size and energy spread of the CFE are lower than those of the other types. However, this energy resolution degrades rapidly under high current conditions because its low angular current density requires larger acceptance angles for high currents and it causes increased amounts of aberration. In middle current region from 1 to 140 pA, No. 3 provides a better energy resolution. For the high current region above 140 pA, No. 4 shows better characteristics. Considering that a CFE without MCs has an FWHM energy spread of 375 meV and MCs cannot easily be implemented, this No. 4 condition has an advantage in a case in which an energy resolution in an approximate range of 60 meV-150 meV is required. No. 2 shows a trend similar to that of No. 3, which is shifted to a lower current condition. The performance of No. 2 is worse than that of the others throughout the current range. Regarding the reduced brightness in Fig. 3-6 (b), No. 1 with the CFE demonstrates better performance with currents of less than 10 pA. For currents higher than 10 pA, No. 3 shows superior performance. The reduced brightness of No. 2 is lower than that of No. 3 given the difference in their angular current densities. No. 4 shows poorer values than the others do because the size of its virtual source is nearly four times larger than that of No. 3.

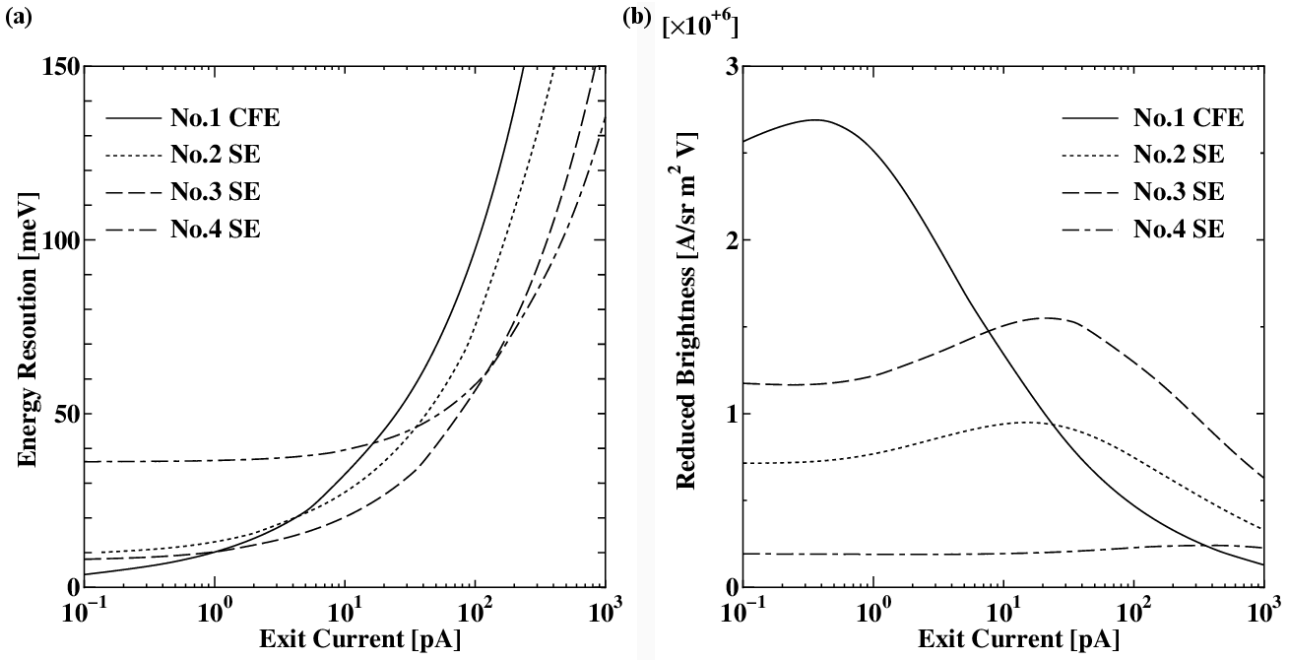


Fig. 3-6 (a) Energy resolution and (b) brightness dependencies on exit current for different source conditions.

Together with Figs. 3-6 (a) and (b), Table 3-5 summarizes the energy resolution with the maximum brightness for each emitter condition.

Table 3-5 The MC performance at the maximum brightness on four source conditions.

| No | Emitter | Exit current | Energy resolution | Reduced brightness |
|---|---|---|---|---|
| | | $I_{out}$ | $\delta E_{mc}$ | $B_r$ |
| | | pA | meV | A/sr m$^2$ V |
| 1 | CFE | 0.3 | 5.6 | 2.7.E+06 |
| 2 | SE | 12 | 29 | 9.5.E+05 |
| 3 | SE | 22 | 27 | 1.6.E+06 |
| 4 | SE | 399 | 92 | 2.5.E+05 |

Table 3-5 provides the typical performance of the MC for the source conditions. Considering the energy resolution and the reduced brightness, suitable emitter conditions for the MC are as follows: For low currents of around 1 pA, No. 1 is favorable. For middle currents between 10 pA and 100 pA, No. 3 is superior. In the higher current region from 200 pA to 1 nA, No. 4 is the desirable condition. No. 2 shows relatively low performance, but it has the advantage of a longer lifetime than the other conditions of SEs. Information on the MC performance for various source conditions is important for understanding these features and considering their applications. It is also essential

to design optics for microscopes downstream of the MC and to estimate the performance of the overall system. It should be noted that aberration coefficients derived in previous sections allow this estimation of the MC performance for different emitter conditions.

## 3-4 Discussion

We discuss the pros and cons of the MC with multiple offset CLs through comparisons with other MCs proposed previously. The discussion in the previous sections reveals that the MC satisfies conditions that require the second-order aperture aberration ($x|\alpha^2$) and the lateral energy dispersion ($x|\kappa$) to be canceled on the exit plane. However, ($x|\alpha^2$) on the midplane, which is not cancelled, limits the energy resolution. In addition, the third-order aperture aberration ($x|\alpha^3$) results in restrictions of the brightness on the exit image plane. Furthermore, the previous chapter shows that the angular energy dispersion ($\alpha|\kappa$) is not canceled at the exit. Table 3-6 summarizes the cancellation of aberrations for this MC together with those of others MCs in the references. It categorizes these MCs into three groups with regard to their aberrations. It also shows energy dispersions and the numbers of power supply modules required by each. Group A includes single-stage MCs. For group A, ($x|\kappa$) is not canceled on the exit plane. Group B includes several multi-stage MCs. For group B, ($x|\kappa$) and ($x|\alpha^2$) are canceled on the exit plane due to its mid-plane symmetry. However, ($\alpha|\kappa$) on the exit plane and ($x|\alpha^2$) on the midplane are not canceled. Group C includes multi-stage MCs equipped with more sophisticated aberration correction methods.

For group C, the aberrations are canceled not only on the exit plane but also on the midplane. The electrostatic Ω-MC utilizes curved surfaces of toroidal electrodes to generate hexapole fields for cancelling ($x|\alpha^2$) on the midplane [16, 17]. The α-MC adopts a number of hexapoles for the cancellation of the aberrations [18, 19]. The MC in this study would belong to group B, as shown in Table 3-6. Hence, it is worse than the sophisticated MCs of group C but better than the single-stage MCs of group A. It has the advantage of being able to prevent rainbow illumination, which can cause issues in TEM observations. A further improvement of the MC can be achieved by adopting additional correctors, similar to the MCs of group C. The cancelation of ($x|\alpha^2$) on the middle plane of $Z_2$ can be realized by two hexapoles at the regions of $Z_1$-$CL_1$ and $CL_2$-$Z_1$. This is often used in sector magnets [11] or in imaging energy filters [25*24]. To cancel both ($x|\kappa$) and ($a|\kappa$) on exit plane $Z_4$, ($a|\kappa$) should be canceled on middle plane $Z_2$, which means that the $x_\kappa$ ray becomes parallel to the optical axis [13]. This condition can be achieved by adopting four offset cylindrical lenses as shown in the previous chapter, or placing two quadrupoles at the regions of $CL_1$-$Z_2$

and $Z_2$-$CL_2$, similar to the α-MC [19].

Table 3-6 Comparison of various MCs.

| No | Name | Type | Cancelation of aberration | | | | | Dispersion (μm/eV at 1keV) | Power supply | | Ref |
|---|---|---|---|---|---|---|---|---|---|---|---|
| | | | Exit plane $Z_4$ | | | Mid plane $Z_2$ | | | Voltage source | Current source | |
| | | | $(x\|\kappa)$ | $(\alpha\|\kappa)$ | $(x\|\alpha^2)$ | $(\alpha\|\kappa)$ | $(x\|\alpha^2)$ | | | | |
| 1 | This study | B | Y | N | Y | N | N | 94 | 2 | | |
| 2 | Wien × 1 | A | N | N | Y | - | - | 3 | 8 | 1 | [20] |
| 3 | Modified gun lens | A | N | N | N | - | - | - | 3+α | | [21] |
| 4 | Wien × 2 | B | Y | N | Y | N | N | 27 | 10 | 2 | [22] |
| 5 | Wien × 4 | B | Y | N | Y | N | N | 16 | 12 | 4 | [23] |
| 6 | Omega | C | Y | Y | Y | Y | Y | 48 | 8 | | [17] |
| 7 | Alpha | C | Y | Y | Y | Y | Y | 600 | | 25 | [19] |

Additionally, Table 3-6 provides the energy dispersions of the MCs. The values in cited articles are converted to those at 1 keV for comparison purposes. The MC in this study shows the second largest energy dispersion due to the strong retarding effect of the CLs. This is one benefit of the MC. The α-MC achieves the largest value because it is equipped with quadruple optics, which magnifies the original dispersion of the sector magnets. Table 3-6 also indicates the number of power supply modules. We estimate the values as accurately as possible from the references. Here, we calculate the voltage sources as twice the number of multipoles. The number of current sources is identical to that of the multipoles. For the MC under study here, the number of power supply modules is the lowest. This is an additional advantage of the MC.

Furthermore, this MC has a simple configuration as a strong point. For CLs, rectangular openings in flat plate electrodes are necessary. Although they require accurate machining, this can be realized by conventional machining tools. The MC has an advantage with regard to its assembly process because CLs consist of flat plate electrodes without separations in the azimuth directions. Compared to this MC, other MCs require complicated configurations. The electrostatic Ω-MC needs eight toroidal electrodes that are curved in three dimensions. The α-MC needs 14 quadrupoles and 8 hexapoles in addition to its 3 main sector magnets.

As disadvantages of the MC of this study, the relatively large aberrations, such as $(x|\alpha^2)$ and $(x|\alpha^3)$, deteriorate its performance somewhat in the high current region. This is caused by the strong retarding effects of the CLs, which generate higher energy dispersions. These retarding effects also make the system weaker against environmental disturbances such as stray magnetic fields. For a practical design, magnetic shields with high permeability should be

implemented outside of the MC. These are often adopted in energy electron analyzers for surface science [26*25].

By categorizing various MCs, we clarify the pros and cons of the proposed MC. This MC shows partially corrected aberrations due to its mid-plane symmetry, and it provides high performance with a simple structure.

## 3-5 Summary

In this chapter, we continue our investigation and offer a complementary discussion on an MC with multiple offset cylindrical lenses, as introduced in previous chapters. By applying a regression analysis to these trajectories, we derive the aberration coefficients of the MC up to the third order. It is evident from the results that the second-order aperture aberration and lateral energy dispersion are cancelled on the exit image plane. This is attributed to the symmetric optics and the optical axis, and to symmetric and asymmetric first-order trajectories. The cancelations of the two types of aberration are crucial for the proposed MC to be used in an electron microscope.

According to the aberration coefficients, we reveal the dependencies of the MC performance, such as the beam width, energy resolution, and brightness, on the beam current. The energy resolution is limited by the second-order aperture aberration on the midplane, and the brightness is limited by the third-order aperture aberration on the exit plane. We estimate the MC performance for various source conditions, such as the types of emitters, the extraction voltages, and the tip radiuses. The optimum conditions of the MC are clarified for these conditions. The quantified characteristics are essential for the practical design of the MC and its application to microscopes.

## Reference

[1] A.B. El-Kareh, J.C.J. El-Kareh, "*Electron Beams, Lenses, and Optics*", (Academic Press, New York, 1970).

[2] M. Berz, Nucl. Instr. Meth. A 258 (3) (1987) 431.

[3] L. Wang, J. Rouse, E. Munro, H. Liu, X. Zhu, Optik 119 (2008) 90.

[4] P.W. Hawkes, "*Handbook of charged particle optics*", 2nd ed., edited by J. Orloff, (CRC Press, Boca Raton, 2009), 219.

[5] E. Kasper, Optik 69 (3) (1985) 117.

[6] G. Martínez, M. Sancho, Nucl. Instr. Meth. A 363 (1995) 198.

[7] M.A.J. van der Stam, P. Kruit, Nucl. Instr. Meth. A 427 (1999) 368.

[8] B. Lencová, J. Zlámal, Physics Procedia 1 (2008) 315.

[9] M. Oral, B. Lencová, Ultramicroscopy 109 (2009) 1365.

[10] J. Rouse, E. Munro, J. Vac. Sci. Tech. B 7 (6) (1989) 1891.

[11] H. Wollnik, "*Optics of Charged Particles*", (Academic Press, London, 1987).

[12] G.A. Schwind, G. Magera, L.W. Swanson, J. Vac. Sci. Tech. B 24 (6) (2006) 2897.

[13] H. Rose, Optik 51 (1978) 15.

[14] S. Sakawa, K. Tsunoda, Y. Terui, Surf. Interface Anal. 35 (2003) 11.

[15] L.W. Swanson, G.A. Schwind, "*Handbook of charged particle optics*", 2nd ed., edited by J. Orloff , (CRC Press, Boca Raton, 2009), Chap.1, 1.

[16] H. Rose, Ultramicroscopy 78 (1999) 13.

[17] S. Uhlemann, M. Haider, Microsc. Microanal. 8 (Suppl. 2) (2002) 584CD.

[18] O.L. Krivanek, J.P. Ursin, N.J. Bacon, G.J. Corbin, N. Dellby, P. Hrncirik, M.F. Murfitt, C.S. Own, Z.S. Szilagyi, Phil. Trans. R. Soc. A 367 (2009) 3683.

[19] O.L. Krivanek, T.C. Lovejoy, N. Dellby, R.W. Carpenter, Microscopy 62 (1) (2013) 3.

[20] H.W. Mook, P. Kruit, Ultramicroscopy 81 (2000) 129.

[21] A. Henstra, J. Chmelik, T. Dingle, A. Mangnus, G. van Veen, Microsc. Microanal, 15 (Suppl. 2) (2009) 168.

[22] G. Martínez, K. Tsuno, Ultramicroscopy 100 (2004) 105.

[23] E. Plies, J. Bärtle, Microsc. Microanal. 9 (Suppl. 3) (2003) 28.

[24] S. Lanio, H. Rose, D. Krahl, Optik 73 (2) (1986) 56.

[25] H. Ibach, D.L. Mills, "*Electron Energy Loss Spectroscopy and Surface Vibrations*", (Academic Press, New York, 1982).

# Chapter 4 SEM Performance with the Monochromator

## 4-1 Introduction

In this chapter, the application of the MC to an SEM will be investigated at extra-low energies. Initially, an SEM model with the MC will be described and then the simulation method will be explained. Then, using the beam widths and the energy resolution at the MC exit, the probe sizes will be estimated for the SEM optics with the MC. Finally, enhancement of the SEM performance with this MC will be discussed for different types of emitters. A detailed discussion of the work will be given in the subsequent sections.

## 4-2 SEM optics using the MC with offset CLs

Figure 4-1 shows a schematic of the SEM optics with the proposed MC. The region between the emitter and $TL_2$ ($Z_0$–$Z_4$) corresponds to the same region in Fig. 2-1. In a subsequent stage of the SEM optics, a condenser lens (CoL), a through-the-lens detector (Det), a scanner (Scan), and an objective lens (OL) are arranged. Electron beams are emitted with an initial energy spread $\delta E_0$ from the emitter. After the beams pass through the MC, they become monochromatic with an energy spread of $\delta E_{mc}$ because of the energy filtering function of the MC, and are then focused at $Z_4$ with magnification $M_0$ of 1. The subsequent CoL and OL elements demagnify and focus the beams on a sample at $Z_6$ with magnification $M$. When we consider that the magnification $M_0$ of the MC is 1, the value of $M$ is equivalent to the total magnification of the SEM optics. Scan, which is a pre-lens double-deflector that consists of coils or electrodes, scans the beams on the sample in a raster mode. Secondary electrons or backscattered electrons, which are generated from the sample by the primary beams, are absorbed into the OL via its immersion magnetic or electrostatic field and are then separated from the primary beams and detected by Det.

The SEM images are then formed by assigning the signals that were detected at each beam position. Other detectors, e.g., a chamber detector, can be used to acquire the SEM images. An energy analysis can also be performed if an energy analyzer is connected to these detectors.

The initial energy $E_0$ of the electron beams is determined using the extraction voltage of the emitter. The beams travel through the SEM optics with pass energy $E_1$ and irradiate the sample with a landing energy $E_2$. These beams, with an incident half-opening angle $\alpha_o$, are convergent on the sample with an acceptance angle $\alpha_i$, which is given by the following relationship:

$$\alpha_i = \frac{\alpha_o}{M}\sqrt{\frac{E_0}{E_2}} \ . \qquad (4\text{-}1)$$

Changing the excitation of the CoL causes a shift in the image position at $Z_5$. Readjustment of the excitation of OL can achieve a different value of magnification $M$ while maintaining the focus on the sample at the same position. This procedure enables adjustment of the acceptance angle $\alpha_i$ to the optimized value given by Eq. (4-1). We postulate that high-performance SEM optics is used by assuming that both the spherical aberration coefficient $C_s$ and the chromatic aberration coefficient $C_c$ are 1 mm. The OL of the SEM is considered to be an immersion lens (either electrostatic or magnetic type) with a short focal length [1, 2]. We discuss the SEM performance based on this model.

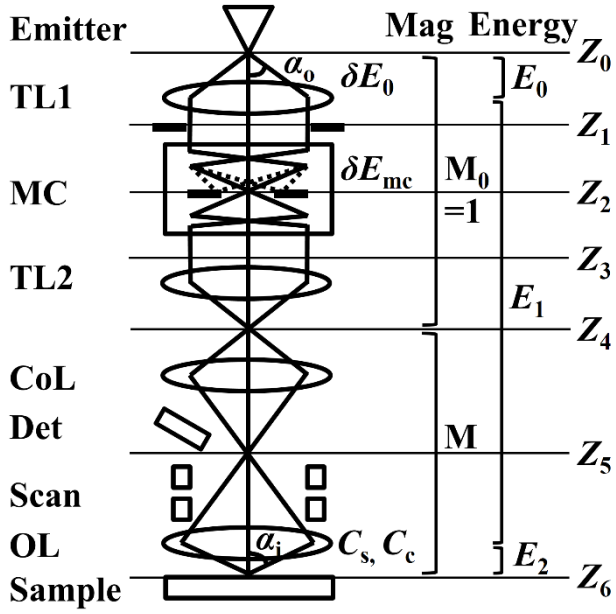


Fig. 4-1 Schematic of the SEM optics.

## 4-3 Method: beam diameter estimation for SEM optics

The SEM performance can be evaluated through derivation of the beam diameter dependence on the probe current. In this study, the analytical algorithm that was proposed by Barth et al. [3, 4] is used to calculate the beam diameters. The authors derived the full-width of a circular diameter that contained 50% of the beam current (FW50) based on a simple root-power-sum algorithm and showed that the calculated values were very close to the values

given by exact calculations such as wave optical calculations and ray-tracing simulations. The total beam diameter $d_{50}$, which was defined as FW50, consists of four individual contributions, which are those of the chromatic aberration $d_c$, the spherical aberration $d_s$, the diffraction aberration $d_A$ (Airy disk), and the Gauss image $d_I$ of the source (current finite brightness). $d_{50}$ is then expressed as follows:

$$d_{50} = \left(d_c^2 + \left((d_s^4 + d_A^4)^{1.3/4} + d_I^{1.3}\right)^{2/1.3}\right)^{1/2}, \tag{4-2a}$$

where

$$d_c = 0.34\, C_c \alpha_i\, \delta E_{z4}/E_2\,, \tag{4-2b}$$

$$d_s = 0.18\, C_s {\alpha_i}^3, \tag{4-2c}$$

$$d_A = 0.54\ \lambda/\alpha_i\,, \tag{4-2d}$$

$$d_I = M d_{z4}\,. \tag{4-2e}$$

In Eq. (4-2b), the contribution of the chromatic aberration ($d_c$) to the total beam diameter is given in terms of the chromatic aberration coefficient $C_c$, the acceptance angle $\alpha_i$, the energy spread $\delta E_{z4}$ of the electron beam on the $Z_4$ plane, and the landing energy $E_2$. The $Z_4$ plane corresponds to the exit plane of the MC and the entrance to the SEM optics, as shown in Fig. 4-1. In Eq. (4-2c), the contribution of the spherical aberration ($d_s$) is expressed using the spherical aberration coefficient $C_s$ and the third power of $\alpha_i$. In Eq. (4-2d), the contribution of the diffraction aberration ($d_A$) is given based on the electron wavelength $\lambda$ and the inverse of $\alpha_i$. Here, $\lambda$ is determined using the landing energy $E_2$ on the sample with the relationship $\lambda = h/\sqrt{2m_0E_2}$, where $h$ is the Planck constant and $m_0$ is the electron rest mass. In Eq. (4-2e), the Gauss image ($d_I$) of the source (current finite brightness) is given by multiplication of the magnification $M$ of the SEM optics and the beam diameter $d_{z4}$ on the $Z_4$ plane. The terms $M$ and $E_2$ were explained in Fig. 4-1, and $\alpha_i$ is given by Eq. (4-1). The numerical values of $C_s$ and $C_c$ were given in the previous section. For a beam with a Gaussian distribution, the beam diameter at the conventional full width at half

maximum (FWHM) is identical to that of FW50. For the aberration-limited beam profile, which shows a sharp peak and a broad tail, the FW50 beam diameter becomes larger than that of the FWHM. Thus, FW50 is considered to be a more accurate and suitable expression for the beam diameters of practical SEMs, which are frequently operated under aberration-dominant conditions. In this study, we evaluate the SEM performance by using the FW50 beam diameters.

## 4-4 Results and discussion

### 4-4-1 SEM performance with the MC

In this section, we estimate the improvements in the performance levels of the SEM when using the MC. Here, we evaluate the SEM optics as shown in Fig. 4-1. We calculate the total beam diameter $d_{50}$ from Eq. (4-2) under two conditions: with the MC, and without the MC.

First, we discuss the SEM with the MC. The following parameters are applied to Eq. (4-2). To the energy spread $\delta E_{z4}$ of Eq. (4-2b), we apply the monochromatic energy spread of the MC, $\delta E_{mc}$, from Eq. (3-8b). The beam size $d_{z4}$ of Eq. (4-2e) is expressed as $d_{z4} = (dx_{z4}+dy_{z4})/2$, where $dx_{z4}$ and $dy_{z4}$ are the beam widths at $Z_4$ that were given in Eq. (3-7c) and Eq. (3-7d), respectively. Here, the $d_{z4}$ term is regarded as the mean value of the beam widths in the X and Y directions. This term includes the aberrations of the MC, as discussed in the previous section. The probe current $I_p$ on the sample is identical to the exit current $I_{out}$ from the MC that was given by Eq. (3-8c).

Second, we consider the SEM without the use of the MC. We assume that the source is imaged at $Z_4$ by the two transfer lenses, $TL_1$ and $TL_2$, with unit magnification, and that the image is free from any aberrations. This is equivalent to the optics where the emitter is located on the $Z_4$ plane that corresponds to the entrance plane of the lens system of the SEM. Therefore, these parameters are identical to those for the initial conditions of the emitter. The following parameters are applied to Eq. (4-2). The energy spread $\delta E_{z4}$ from Eq. (4-2b) is considered to be the FWHM energy spread $\delta E_0$ of the emitter. The beam size $d_{z4}$ from Eq. (4-2e) is identical to the virtual source diameter $d_0$ of the emitter. The probe current $I_p$ is given by $I_p = I_{in} = I'\pi\alpha_o^2$, and the relationship between $\alpha_o$ and $\alpha_i$ is given in Eq. (4-1). The specific values of these parameters were given in the previous section.

We then calculate $d_{50}$ for a probe current $I_p$ using Eq. (4-2a) under the two conditions where the SEM is operating with or without the MC. Figure 4-2 shows the dependence of the $d_{50}$ values on the acceptance angle $\alpha_i$, where the landing energy $E_2$ is 100 eV and the probe current $I_p$ is 1 pA. The contributions from the aberration terms

that are given in Eqs. (4-2 b–d) are also shown. As Fig. 4-2 indicates, the minimum beam diameter is achieved at the optimum value of the acceptance angle $\alpha_i$, which corresponds to the optimum operating condition. This is attributed to the different dependences of the four aberration terms on the acceptance angle $\alpha_i$. Fig. 4-2 clearly shows that the use of the MC improves the total beam diameter dramatically, reducing it from 19.7 nm to 4.4 nm.

For the SEM optics operating without the MC, the minimum beam diameter is achieved when the chromatic aberration and diffraction aberration are balanced; these terms increase in inverse proportion to $E_2$ and $E_2^{0.5}$, respectively.

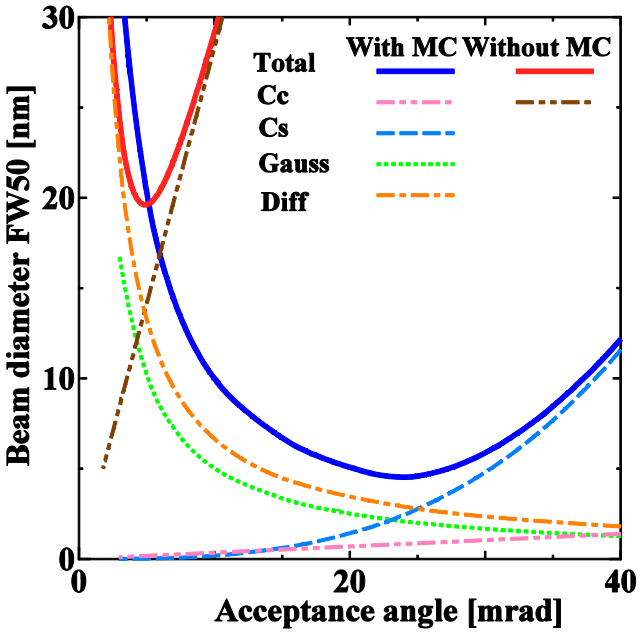


Fig. 4-2 Beam diameter dependence on the acceptance angle with and without the MC.

In the SEM optics operating with the MC, the optimum condition is achieved when the spherical aberration and diffraction aberration are balanced. In this case, the contribution of the chromatic aberration (shown in pink) becomes negligible because the energy spreads of the electron beams have been narrowed by the MC. This enables the use of larger acceptance angles, which thus leads to a significant reduction in the diffraction aberrations. The optimum acceptance-angle $\alpha_i$ increases from 4.8 mrad without the MC to 24 mrad with the MC. This large $\alpha_i$ value leads to an increased contribution from the spherical aberration because of its dependence on $\alpha_i^3$. In contrast, the spherical aberration only has a minor effect when operating without the MC.

Next, we discuss the dependence of the beam diameters on the probe currents, which represent the SEM

performance. In a manner similar to that shown in Fig. 4-2, we derive the minimum beam diameter by varying the acceptance angle $\alpha_i$ for a given probe current $I_p$. The beam diameter dependences on the various probe currents when operating with and without the MC are shown in Fig. 4-3a and Fig. 4-3b, respectively. The optimum acceptance angle ($\alpha_i$) and magnification ($M$) dependences are shown in Fig. 4-3c. The beam landing energy $E_2$ is 100 eV. In the graphs, the values of total beam diameter $d_{50}$ from Eq. (4-2a) and the contributions of the four aberration terms from Eqs. (4-2b–e) are shown. In the low current region, the beam diameters improve dramatically when the MC is used. The SEM with the MC shows superior performance in the middle current region at approximately 160 pA.

When the SEM is operated without using the MC, the chromatic aberration and the diffraction aberration are the dominant factors at low probe currents. As the probe currents increase, the influence of the diffraction aberration decreases. Under high current conditions at approximately 1 nA, the chromatic aberration and the Gauss image then become the major factors. This trend can be explained as follows. When the probe current $I_p$ increases, the incident angle $\alpha_o$ also increases based on the relationship $I_p=I'\pi\alpha_o^2$. If the optical conditions remain constant, then the subsidiary acceptance angle $\alpha_i$ increases in the manner indicated by Eq. (4-1), which could then lead to a considerable increase in the chromatic aberration. When the optics is optimized by increasing the magnification $M$, it is possible to suppress or at least minimize the increase in $\alpha_i$, as shown in Fig. 4-3c. This prevents any increase in the chromatic aberration. However, the larger value of $M$ then causes an increase in the Gauss image, which becomes one of the dominant factors affecting the total beam diameter. The effect of the spherical aberration is negligible because the $\alpha_i$ keeps taking relatively small value.

When the SEM is operated with the MC, the beam diameter dependences on the probe currents can be interpreted in the following manner. The spherical aberration and the diffraction aberration are the two major factors under low probe current conditions, as shown previously. As the probe current increases, the Gauss image increases and then becomes the dominant factor. This behavior is attributed to the third-order aperture aberration $(x|\alpha^3)_{z4}$ of the MC. The increased Gauss image does not allow $M$ to be a large value, as the case without the MC. This results in an increase in $\alpha_i$ with increasing probe current, which subsequently causes increases in both the spherical and chromatic aberration and a decrease in the diffraction aberration. At probe currents of approximately 10 pA, the spherical aberration becomes the second largest term. When the current increases further, then the influence of the chromatic aberration also increases. This is also caused by deterioration of the effectiveness of the MC, which leads to an increase in the energy spread $\delta E_{mc}$, as shown in Fig. 3-6, due to the second-order aperture aberration $(x|\alpha^2)_{z2}$ of the MC. Therefore, for currents >100 pA, the beam diameter is limited by both the Gauss image and the chromatic

aberration. This discussion with regard to the results shown in Fig. 4-3 clearly determines the beam diameter dependencies on the probe currents based on the effects of the use of the MC.

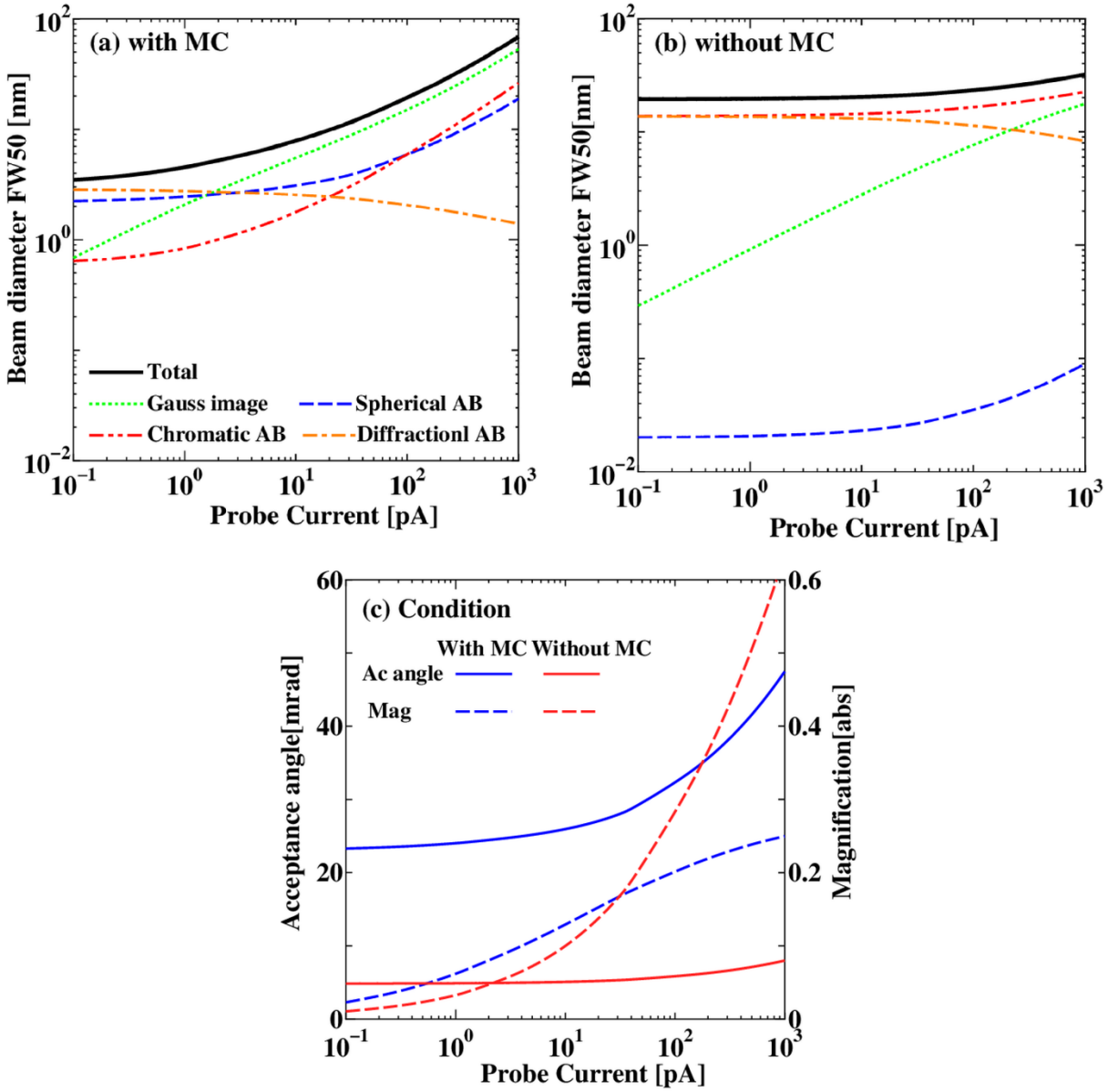


Fig. 4-3 Beam diameter dependence on the probe current when operating (a) with and (b) without the MC. The dependences of the optimum acceptance angle and the magnification are shown in (c).

Next, we evaluate the SEM performance for various landing energies. Figure 4-4 shows the beam diameter dependence on the probe current with or without the MC, for landing energies of 10, 100, 1000, and 5000 eV. The graph clearly shows the prominent effect of the MC at lower landing energies, at which the chromatic aberrations have a greater influence on the beam diameter. In addition, the effective current range of the MC expands at lower

energies. Conversely, at a higher energy of 5 keV, the MC is shown to have only a minor effect in the practical current region. Table 4-1 summarizes the beam diameters for the various landing energies at a probe current of 1 pA. The results in this section demonstrate that the MC is effective at extra-low energy levels of <1 keV.

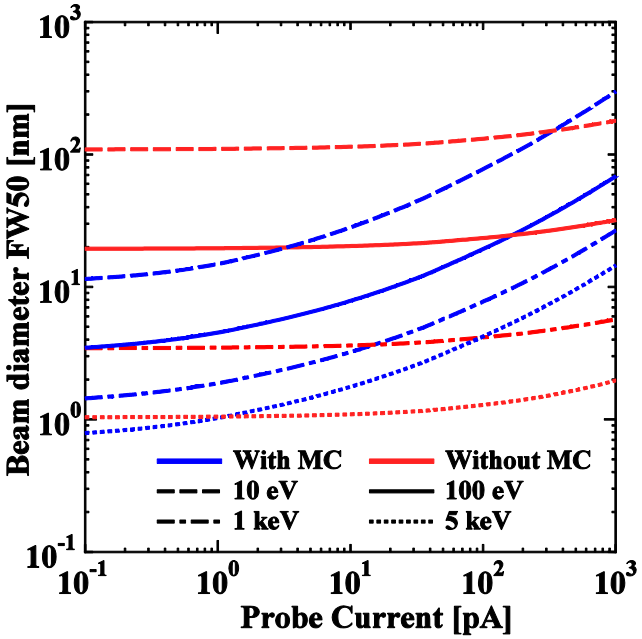


Fig. 4-4 Beam diameter dependence on the probe current with and without the MC for various beam energies.

Table 4-1 SEM performance with and without the MC.

| Landing energy | Beam diameter FW50 | |
|---|---|---|
| | With MC | Without MC |
| (eV) | (nm) | (nm) |
| 10 | 14.9 | 110. |
| 100 | 4.4 | 19.7 |
| 1000 | 1.9 | 3.5 |
| 5000 | 1.0 | 1.0 |

### 4-4-2 SEM performance for various source parameters

The SEM performance that was discussed in the previous section represents only one solution for one source condition. During the SEM design process, the types of electron sources and the related parameters can be selected for specific microscope applications. In previous studies, MCs were used together with a Schottky emitter (SE) made of ZrO/W (100) or a cold field emitter (CFE) made of W (310). Here, we estimate the SEM performance when using the MC for various source parameters. Table 4-2 summarizes the three conditions that are compared here.

Condition No. 1 is for the CFE, and condition Nos. 2 and 3 are for the SEs. The data for Nos. 1 and 2 are cited from Schwind et al. [5] and those for No. 3 are cited from Sakawa et al. [6]. The CFE used in condition No. 1 has the advantages of a smaller virtual source size and a smaller energy spread but also has the disadvantage of a smaller angular current density when compared with that of the SEs. Condition No. 2 is a typical SE condition and corresponds to the simulation conditions used in the previous sections. Condition No. 3 is for a different SE with a very large tip radius of 4.2 μm, which is eight times larger than that of the conventional SE shown in condition No. 2. This large tip radius results in a reduced energy spread with an angular current density that is identical to that of No. 2 because of the reduced Boersch effect in the vicinity of the emitter surface. Based on the work of Swanson et al. [7], we have also estimated an extractor voltage and a virtual source size for condition No. 3, as shown in Table 4-2, which Sakawa et al. [6] did not show in their article. The main shortcoming of condition No. 3 is the large virtual source size that is caused by the large tip radius.

Table 4-2 Source conditions.

| No. | Emitter type | Tip radius $a$ (nm) | Extraction voltage $V_{ext}$ (V) | Angular current density $I'$ (μA/sr) | Energy spread $\delta E_0$ (eV) | Virtual source diameter $d_0$ (nm) | Ref. |
|---|---|---|---|---|---|---|---|
| 1 | CFE | 175 | 4300 | 62 | 0.375 | 4 | 6 |
| 2 | SE | 550 | 5459 | 500 | 0.833 | 28 | 6 |
| 3 | SE | 4200 | 14833* | 500 | 0.430 | 130* | 8 |

* Estimated values

Figure 4-5 shows the dependences of the beam diameter and the energy spread on the probe current for the three emitters described in Table 4-2. The graph is calculated for the SEM operating with the MC at a beam energy of 100 eV. The beam diameters are calculated in a similar manner to that used previously. In addition, the energy resolutions are derived using Eq. (3-8b). At the probe current of 1 pA, the CFE in condition No. 1 and the SE in condition No. 2 show equivalent performances with beam diameters of better than 5 nm and energy resolutions of approximately 10 meV. For currents of less than 1 pA, the energy resolution performance of No. 1 is better than that of No. 2 because the CFE has a smaller energy spread and a smaller virtual source size. With regard to the beam diameters, the curve of No. 1 coincides with that of No. 2 because the beam diameters are mainly determined by the diffraction aberration and the spherical aberration, which are both largely independent of the source parameters. In the middle current region, which ranges from 1 pA to 140 pA, No. 2 shows superior performance. The beam diameter

ranges from 4 nm to 23 nm and the energy resolution ranges from 10 to 60 meV. Consideration of the results when operating without the MC shown in Fig. 4-3 indicates that No. 2 should be operated in this current range.

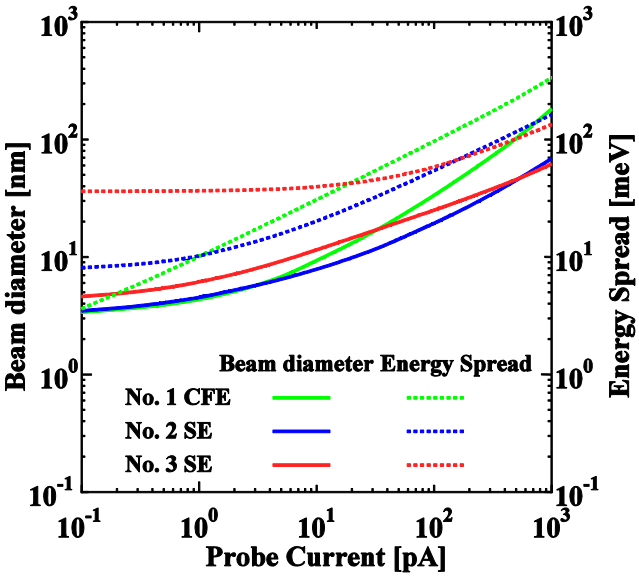


Fig. 4-5 Beam diameter and energy spread dependences on probe current with the MC for different emitters.

In the high-current region, No. 3 shows better performance. Its energy resolution is superior for currents >140 pA, and its beam diameter is the smallest for current levels >300 pA. This is attributed to the smaller energy spread of No. 3 when compared with that of No. 2 at an identical angular current density. However, under low probe current conditions, the energy resolution of No.3 of 36.5 meV is much worse than that of the other two conditions because its large virtual source size leads to larger slit sizes on the energy-selection plane $Z_2$. The beam diameter of No. 3 is 6.1 nm, which is slightly larger than those for the other two conditions. This is achieved by high demagnification (i.e., smaller $M$), which suppresses the increase in the beam diameter caused by the virtual source size. Condition No. 3 thus has an advantage when the required energy resolution is in the 60–150 meV range, assuming that the MCs are complex and expensive units and that a CFE operating without the MC has an FWHM energy spread of 375 meV. To summarize these results, the most suitable emitter conditions for the MC are as follows. For lower currents of up to 1 pA, condition No. 1 is favorable. For mid-range currents of between 1 pA and 140 pA, condition No. 2 is superior. At higher currents ranging from 140 pA to 1 nA, condition No. 3 is the most desirable. These evaluations of SEM performance under various source conditions are important for the development of SEMs that are suited to their target applications.

### 4-4-3 Features of and perspectives on the MC for application to SEM

In this section, we discuss the features of the MC by comparison with those of MCs that were used in previous studies. The proposed MC can achieve high-energy resolution of 10 meV because of its large energy dispersion $D_\kappa$, as shown in Eq. (3-8a). The MC can also improve SEM spatial resolution, particularly at extra-low energies, as discussed in the previous sections. It should be noted at this point that the SEM optics is assumed to offer high performance with the spherical aberration coefficient $C_s$ and the chromatic aberration coefficient $C_c$ both being 1 mm. This MC enables further improvement of the SEM performance at low energies. In addition, when combined with a high-resolution energy analyzer similar to that used in the HREELS instruments [8], the MC could resolve phonon signals using electron probes with small beam sizes of 5 nm and low energies of 100 eV. Conversely, the large energy dispersion $D_\kappa$ of the MC results in a relatively large aberration, which causes the beam performance to deteriorate under higher current conditions.

The proposed MC has the additional advantage of a simple mechanical configuration without the use of multipole optics. The simple structure of this MC reduces or eliminates most difficulties in the required machining and assembly processes. The structure also brings high levels of robustness and stability, which are particularly necessary for industrial applications such as quality control during semiconductor manufacturing. In addition, the structure enables easy and cost-effective production of the MC. Another viewpoint that must be considered is that this MC uses purely electrostatic optics, from which the electrodes generate lower levels of outgas than magnetic components such as coils. Therefore, an electron gun chamber that includes this MC can achieve ultra-high vacuum (UHV) conditions much more easily than magnetic-type MCs. In addition, because of the small hysteresis effect of electrostatic optics, rapid responses and good reproducibility can be realized. These features allow SEM operators to turn the MC on and off rapidly. In addition, this MC uses linear optics, which simplifies the process of alignment of the MC with the other SEM optics. Furthermore, this MC can be installed within the diameter of the SEM column, which enhances the mechanical stiffness of the column. Furthermore, the conventional optics can be used simply by turning the MC off and changing the aperture position if higher beam currents are required. These merits are important for SEM applications because the users frequently change the operating conditions and prefer simplicity when performing their daily operations.

## 4-5 Summary and conclusions

In this chapter, we investigate applications of the MC to an SEM at extra-low energies of less than 1 keV. Assuming the use of ideal and high-performance SEM optics with $C_s$ and $C_c$ values of 1 mm, FW50 beam diameters are calculated at the positions of specimens. Use of the MC improves the beam diameter dramatically to 4.4 nm, as compared to the diameter of 19.7 nm for the SEM without the MC, at a landing energy of 100 eV and a probe current of 1 pA. The chromatic aberration contribution becomes negligible because of the MC. The beneficial effects of the MC for the beam diameter become more prominent at lower landing energies ranging down to 10 eV. In addition, the effective current ranges of the MC expand at lower energies. We also surveyed the SEM performance under various emitter conditions, finding the optimum current ranges for the SEM with the sources. From the quantitative estimation done here, we can conclude that this MC can effectively improve the SEM performance in extra-low energy regions.

## Reference

[1] L. Reimer, "Scanning Electron Microscopy: Physics of Image Formation and Microanalysis", 2nd ed., (Springer-Verlag, Heidelberg, 1998).

[2] K. Tsuno, J. Electron Microsc. 48 (6) (1999) 801.

[3] J.E. Barth, P. Kruit, Optik 101 (3) (1996) 101.

[4] J.E. Barth, M. D. Nykerk, Nucl. Instrum. Meth. A 427 (1999) 86.

[5] G.A. Schwind, G. Magera, L.W. Swanson, J. Vac. Sci. Technol. B 24 (6) (2006) 2897.

[6] S. Sakawa, K. Tsunoda, Y. Terui, Surf. Interface Anal. 35 (2003) 11.

[7] L.W. Swanson, G.A. Schwind, "*Handbook of charged particle optics"*, 2nd ed., edited by J. Orloff, (CRC Press, Boca Raton, 2009), Chap. 1, 1.

[8] H. Ibach, D.L. Mills, "*Electron Energy Loss Spectroscopy and Surface Vibrations"*, (Academic Press, New York, 1982).

# Chapter 5 Experimental Evaluation of the Electron Optics with an Offset Cylindrical Lens

## 5-1 Introduction

Based on theoretical studies in the previous chapters, a prototype of the MC has been manufactured in a test bench. In two successive chapters, chapters 5 and 6, evaluation results of the prototype will be presented. First, common topics of the two chapters, the entire evaluation system of the prototype of the MC and two evaluation methods for energy resolutions of the MC, will be described. In this chapter, the first half of the MC optics, which mainly determines the energy resolving performance, will be evaluated. The electron optics includes an offset cylindrical lens (CL) and an additional transfer lens (TL). This optics can serve as an energy analyzer (EA). Energy resolutions will be examined by comparing total energy distributions (TEDs) of Schottky emitters (SEs) in experiment and theory based on a previous study by Mook et al. [1]. The accuracy and stability of a total measurement system and the optical conditions of the optics will be evaluated. In addition, it is shown that the optics can measure TEDs of SEs in various operational conditions.

## 5-2 Prototype of the MC in a test bench

Based on the theoretical studies in the previous chapters, a prototype of the MC with offset CLs has been manufactured in a test bench. Figure 5-1 shows a schematic of the MC prototype including configurations of the optics, the main trajectories, and electronics. The evaluation system includes an SE, the MC, a retarding field energy analyzer (RFA), and a detector. The MC satisfies the middle plane symmetry in its optical configuration and each half of the MC contains a CL and a TL. An energy selection aperture (ES-AP) on the middle plane filters zero-loss beams from energy-dispersed beams.

On the left side of Fig. 5-1, blue and yellow arrows show parts of components utilized for evaluations in chapter 5 and 6, respectively. In chapter 5, the first half of the MC, which mainly determines the energy resolving performance, is evaluated. In chapter 6, the entire MC is evaluated with the RFA on the downside.

The SE consists of a tip, a filament loop, and a suppressor. A current source supplies the current $I_{FIL}$ through the filament loop, and heats the tip to 1800 K. The electrical potential of the tip, which is close to the ground (GND) level, is given mainly by the bipolar acceleration voltage $V_{ACC}$.

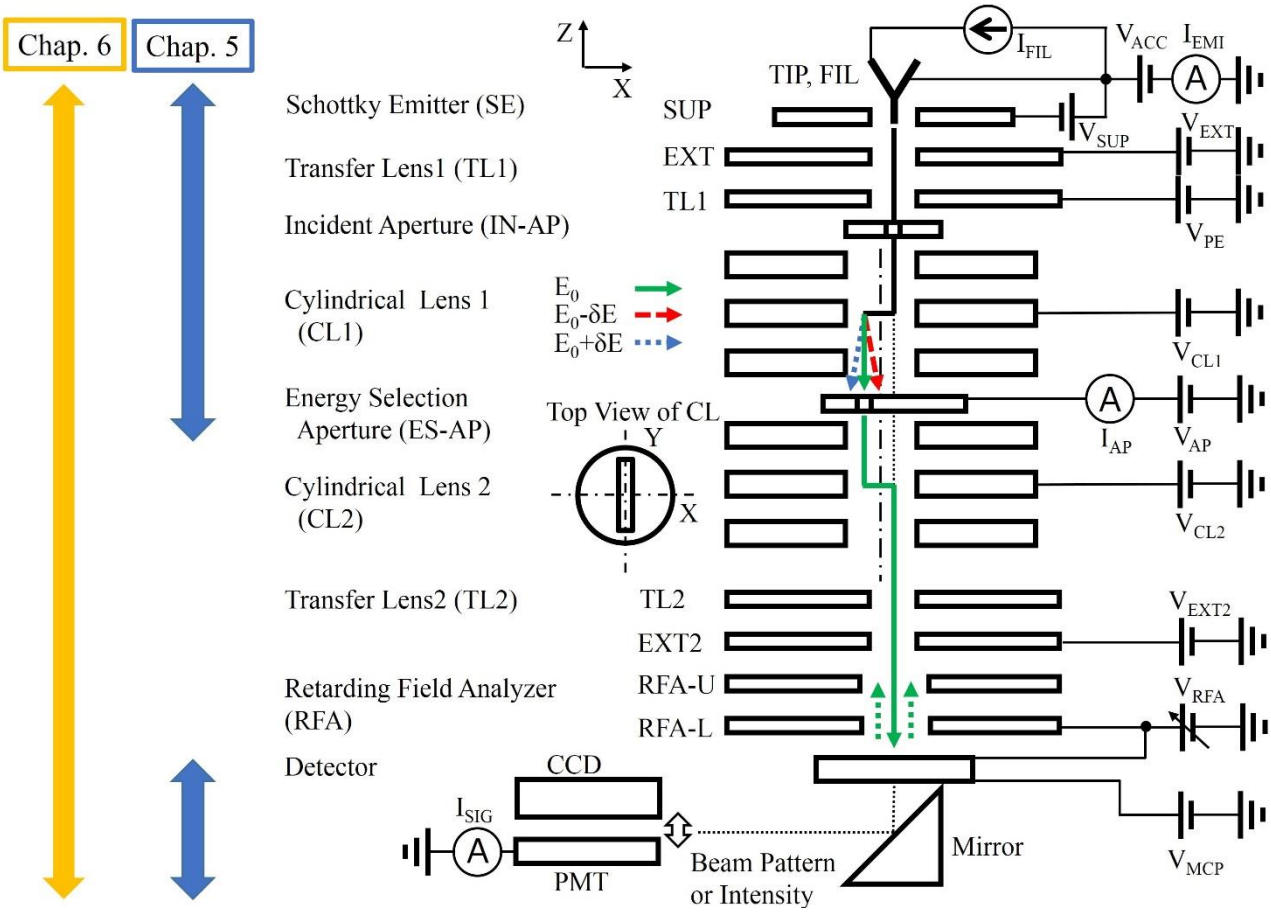


Fig. 5-1 Schematic of the MC prototype in the test bench.

A voltage drop, caused by the current through the filament loop, slightly influences the tip potential. Emission currents $I_{EMI}$ from the tip are measured by an ammeter between the voltage source of $V_{ACC}$ and the GND. The suppressor with a negative voltage $V_{SUP}$ to the tip suppresses unnecessary electron beams (EBs) from the shank of the tip or the filament loop. The position of the SE can be adjusted by an XY stage. The EBs are extracted from the tip into the vacuum by a high voltage $V_{EXT}$ to an extractor (EXT) electrode. The EBs exhibit TEDs through this emission process. Here, we evaluate two types of SEs; SE No. 1 (Model: 174) and SE No. 2 (Model: module C2), which are from Denka Company (Tokyo, Japan). The tip radiuses of SE No. 1 and No. 2 are 0.41 and 0.54 μm, respectively. SE No. 2 has an additional extractor electrode (not shown in the figure) in front of the tip, which provides a higher extraction field compared to SE No. 1.

The TL1 is located on the downstream side of the SE, where the potential difference between EXT and TL1 electrodes forms a bi-potential lens, which collimates or focuses the EBs from the source. The circular openings of these electrodes make an axially symmetric lens, which exhibits an equivalent lens effect in any azimuthal direction.

The positive voltage $V_{PE}$ to the TL1 electrode is lower than $V_{EXT}$, decelerates EBs, and determines the pass energy (PE) of EBs inside the optics. The PE is given by

$$PE = e\,(V_{PE} - V_{ACC}). \quad (5\text{-}1)$$

Here, $e$ denotes the elementary charge. A fixed incident aperture (IN-AP) is located near the back-focal plane of the TL, which confines the regions of the EBs entering into the optics. In the evaluations, two types of the IN-AP with diameters of 200 and 30 μm are adopted.

The CL1 and CL2 are symmetrically arranged with the middle plane. Each CL consists of three electrodes with rectangular openings and the center is offset to the optical axis. The CLs can generate deflection and focusing actions in the X direction, but almost no optical action in the Y direction. The main rays are deflected by the CL1, pass through the EA-AP located at the symmetric plane, and are deflected back to the original axis by the CL2. The energy-dispersed rays are filtered out by the EA-AP and monochromatic beams are achieved, which are shown as colored arrows in Fig. 5-1. The first half of the MC with a combination of the CL and ES-AP can serve as an energy-filter to the EBs with an initial energy distribution. The width of the opening of the ES-AP is 12.5 μm in the X direction. The position of the ES-AP is controlled with high accuracy by a piezo-stage (SL-06, SmarAct, Oldenburg, Germany).

The TL2 are located at the position that satisfies the midplane symmetry of the MC optics. If the TL2 is excited with setting $V_{EXT2}$ at the identical voltage to $V_{EXT}$, the EBs can be focused on the image plane. However, in this study, the TL2 is mainly turned off with setting $V_{EXT2}$ at the same voltage as $V_{PE}$ because it is necessary to observe beam profiles in sufficient sizes at the detector plane. In this case, the EBs exit out of the MC with collimated trajectories.

The RFA is located at the downside of the MC optics. In the next chapter (Chapter 6), energy spreads of EBs are measured with the RFA, which consists of two electrodes of RFA-U and L. The potential difference between $V_{PE}$ and $V_{RFA}$ forms a high-pass energy filter when $V_{RFA}$ is set as a similar level with $V_{ACC}$. If the RFA is turned off with setting $V_{RFA}$ at the same voltage as $V_{PE}$, EBs can pass through the RFA without any disturbance.

After passing through the RFA, the EBs are detected by a detector assembly (BOS-18, Beam Imaging Solutions, Longmont, CO, USA) with a micro-channel plate (MCP) and a phosphor screen (SCR). The double-stacked type of the MCP is adopted because of its high-gain. The MCP multiplies the incident EBs by a voltage $V_{MCP}$, and the EBs collide into the SCR after acceleration with a voltage $V_{SCR}$, generate photons, and form an image of the

beam profile. This image is reflected 90 degrees by a mirror at the bottom side of the detector and observed from outside through a viewing port. A CCD camera (ORCA-R2, Hamamatsu Photonics, Hamamatsu, Japan) captures and records these images of the beam patterns as digital data. In another setup, a photomultiplier tube (H10721-110, Hamamatsu Photonics, Hamamatsu, Japan) converts the total signal intensity of the EBs into current outputs $I_{SIG}$, and an ampere-meter records the signals.

Figure 5-2 shows pictures of the MC prototype including a main unit on the left side and electronics on the right side. The main unit constitutes of a UHV chamber, a supporting table, vibration isolators, and an ion pump. The MC optics is installed inside the UHV chamber that is evacuated by the ion pump. After baking at 200 °C for three days, a base pressure of $1.3 \times 10^{-8}$ Pa is achieved, which is a sufficient vacuum level for proper operation of the emitters.

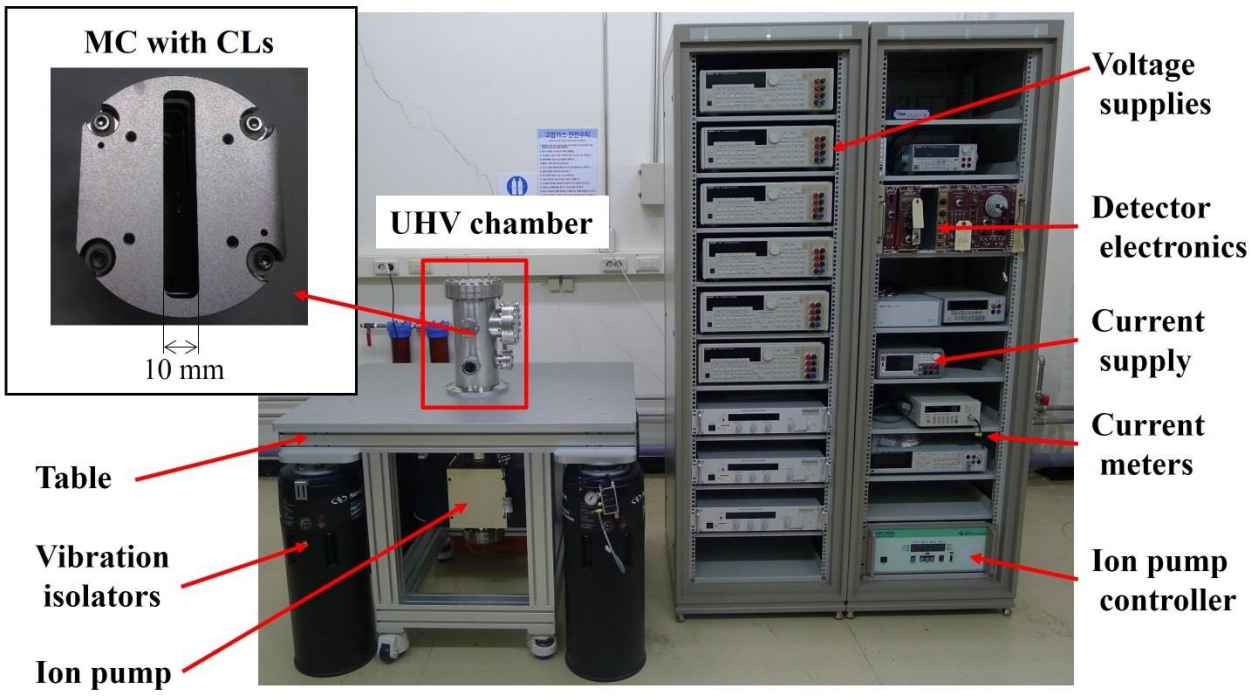


Fig. 5-2 Pictures of the MC prototype in the test bench.

The inset of Fig. 5-2 shows a picture of the MC unit with offset CLs. The CL electrodes are of circular shape with diameters of 70 mm, and both sides are chamfered. The width of the rectangular openings is 10 mm in the X direction. The mechanical parts are machined and assembled with a high mechanical accuracy at several micrometers. The CL electrodes are stacked with ceramic spacers for insulation and fixed with four screws at the corners. The

material for these electrodes is SUS304. The optics is based on the concept of a modular design, which means that optical components such as the CLs are integrated into the single unit. The inset also shows that the lens system is in a linear layout.

The electrical system on the right side of Fig. 5-2 constitutes of voltage supplies, detector electronics, a current supply, current meters, and an ion pump controller. The power supplies for the optics were carefully chosen with as low noise as possible. Some of the electronics are described as follow; for $V_{PE}$, $V_{CL1}$, and $V_{CL2}$, high voltage supplies (6166, ADCMT, Tokyo, Japan) are adopted, where the specified ripple noise in RMS is 1 mV from 0.1 Hz to 10 kHz in the output range of 1 kV. For measuring the PMT output signal $I_{SIG}$, a current meter (5450, ADCMT) is used, which has an additional voltage output used for $V_{RFA}$.

The electrical system of the MC prototype equips three scanning modes to generate energy spectra; ACC, CL, and RFA scan modes. The ACC and CL scan modes are used in chapter 5 and the RFA scan mode is used in chapter 6. In the ACC scan mode, the voltage $V_{ACC}$ is scanned and a constant voltage $V_{CL}$ is applied to the CL to generate the energy-filtering effect. The change in $V_{ACC}$ corresponds to the change in the mean pass energy of the EBs into the optics based on Eq. (5-1). By measuring the signal intensity $I_{SIG}$ through scanning $V_{ACC}$, the energy spectra are generated. This mode will be adopted for the evaluation of energy resolutions with acquired TEDs of SEs. In the CL scan mode, where the voltage $V_{CL}$ is scanned and the specified voltage $V_{ACC}$ is applied to the tip. The change in $V_{CL}$ corresponds to the change in excitation of the energy filter with the CL, in which EBs with different energy conditions can pass through the ES-AP. This CL scan also generates energy spectra, but a calibration of $V_{CL}$ to the energy is necessary. By setting different offset voltages of $V_{ACC}$, energy spectra with different mean pass energies are obtained based on Eq. (5-1). This mode will be adopted for the evaluation of the accuracy and stability of the total system. The two modes will be used in this chapter. In the RFA scan mode, scanning the voltage $V_{RFA}$ with measuring the output signals $I_{SIG}$ of the detector gives integrated forms of energy spreads of the EBs. This mode will be adopted for the evaluation of energy widths narrowed by the MC in chapter 6.

## 5-3 Two evaluation methods of energy resolutions of the MC

An energy resolution of the MC is one of the most important evaluation factors. In this study, two evaluation methods are adopted in chapter 5 and 6. Fig. 5-3 explains the methods. The MC has the energy filtering capability and generates EBs with the narrowed energy spread $\delta_{MC}$, which corresponds to the energy resolution of the MC.

As method No. 1 adopted in chapter 5, energy resolutions are evaluated through comparing energy distributions of the SE between experiment and theory. Scanning a mean energy level of the emitter through measuring the total output signal of the energy-filtered EBs gives an energy distribution, which is a convolution form of the intrinsic energy distribution of the SE and the energy resolution of the MC. The intrinsic energy distribution can be estimated from the theory of electron emission process of the emitter. Therefore, a comparison of energy distributions between experiment and theory gives the energy resolution. In the evaluation, the power-means method is adopted to estimate the energy resolution. In method No. 1, the MC is considered to be an EA, which gives energy distribution of the SE.

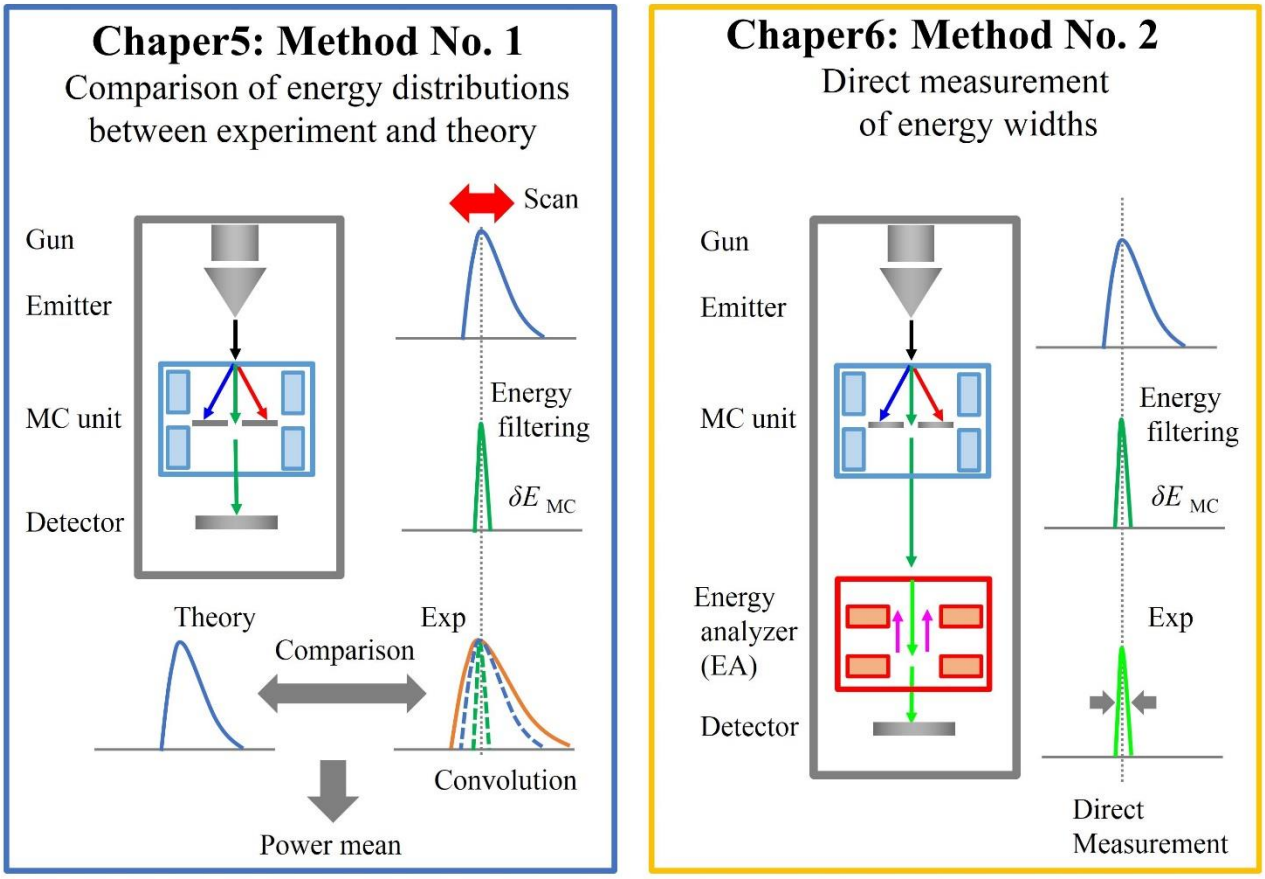


Fig. 5-3 Two evaluation methods of energy resolutions of the MC.

As method No. 2 adopted in chapter 6, the energy resolution of the MC is directly evaluated. Energy widths narrowed by the MC are measured with the additional EA at the downside. The difference of two energy widths, which is measured with and without the MC, clearly shows the effect of the MC. The RFA is adopted as the EA and

the optical configuration is explained in Fig. 5-1 in the previous section.

## 5-4 Theoretical energy distributions of Schottky emitters and estimation method of energy resolutions

In this chapter, energy resolutions of the MC are estimated with method No. 1 in Fig. 5-3. In this section, the method is explained in detail. Young and Kuyatt [2] showed that the measured TEDs were given by the convolutions of native energy spreads of the emitters and the energy resolutions of EAs. The performances of MCs [1] and EAs [3, 4] were evaluated by comparing the TEDs obtained from theory and experiment.

First, the TED of SEs obtained from theory will be briefly described. For SEs, electrons inside the metals of the tips are emitted into the vacuum through two processes. Some of the electrons overcome the Schottky barrier with thermal excitation, and the others pass through the barrier by the tunneling effect. Therefore, the TED of SE consists of the thermal emissions on the higher energy side and the field emissions on the lower side. The TED is described as a deviation of the current density *J* with an energy *E*. From textbooks [5, 6] and previous articles [3, 7], an analytical expression of the TED for the extended Schottky regime is given by

$$dJ/dE = 4\pi me\kappa \ln[1 + exp(E/\kappa)]/h^3\{1 + \exp[(E + V_m)/k_BT]\}, \quad (5\text{-}2a)$$

where

$$V_m = W - \sqrt{e^3F/4\pi\varepsilon_0}, \quad (5\text{-}2b)$$

$$\kappa = \left(\hbar/\pi\sqrt{m}\right)(4\pi\varepsilon_0 eF^3)^{1/4}, \quad (5\text{-}2c)$$

$$F = \beta V_{EXT}, \quad (5\text{-}2d)$$

$$q = \kappa/K_BT. \quad (5\text{-}2e)$$

Here, we adopted the notation reported by Fransen et al. [3]. The physical constants are as follows: *m* is the electron

mass, $e$ is the elementary charge, $h$ and $\hbar$ are the Planck constant and its reduced value, $k_B$ is the Boltzmann constant, and $\varepsilon_0$ is the permittivity of vacuum. The parameters depending on the emitter and its operating conditions are as follows: $T$ is the temperature, $W$ is the work function, $\beta$ is the field factor, and $F$ is the electric field at the surface of the emitter. The value of $\beta$ can be derived from a gradient of the Schottky plot based on the relationship between $I_{EMI}$ and $V_{EXT}$. The parameter $q$ indicates the proportion of the tunneling current to the total current. With Eq. (5-2), an intrinsic energy spread $dE_{INT}$ can be derived. Two expressions exist to describe the energy spread; the full width at half-maximum (FWHM), which refers to the full width of the TED between the two points where the signals are half of the maximum. As another expression, FW50 represents the full width of the TED that contains 50% of the total current [8].

For the energy spread $dE_{EXP}$ from experimental measurements of TEDs, one needs to consider two additional contributions as well as $dE_{INT}$. One factor is the energy resolution of the MC or EA, which is expressed as $dE_{RES}$. The other factor is the increase through stochastic Coulomb interactions of electrons, which is known as the Boersch effect. This term is expressed as $dE_{BOE}$. Then, the experimental energy spread $dE_{EXP}$ is given by

$$dE_{EXP} = (dE_{INT}{}^{\gamma} + dE_{BOE}{}^{\gamma} + dE_{RES}{}^{\gamma})^{1/\gamma}. \quad (5\text{-}3)$$

Based on the assumption that $dE$ is the FWHM and $\gamma$ is 2, Sakawa et al. [9] compared the measured value of $dE_{EXP}$ with the quadratic addition of $dE_{INT}$ and $dE_{BOE}$. Using the same assumption, Sakakibara et al. [10] derived the energy resolution $dE_{RES}$ of an EA. Both studies assumed that the distributions were Gaussian. If $dE$ is expressed in the form of the FW50, Eq. (5-3) is established with an effective $\gamma$ independent of the shape of the respective distribution [8]. Swanson et al. [5, 7] found $\gamma$ of 1.56 in the SE regime using a fitting method. The authors also show that the energy spread $dE_{BOE}$ by the Boersch effect is a function of the angular current $I'$ and $\beta$. At small current conditions, $dE_{BOE}$ decays to zero and this term can be neglected in Eq. (5-3). Therefore, by applying the measured $dE_{EXP}$ at small current conditions and the theoretical intrinsic energy spread $dE_{INT}$ into Eq. (5-3), we can estimate the energy resolutions, $dE_{RES}$, of the optics at the FWHM or the FW50.

## 5-5 Results and discussion

### 5-5-1 Optical actions of the offset CL and the TL

In this section, we evaluate the offset CL and the TL, which are important optical components for the MC optics, by observation of the beam profiles at the detector. Here, the ES-AP was not installed, which enabled us to observe the beam profiles in a wide field of view without limitation. In addition, we adopted the IN-AP with a large diameter of 200 μm to show the optical action of the components more clearly. The evaluation was for SE No. 1 with the following conditions; $V_{EXT}$ was 3.1 kV, $V_{SUP}$ was −210 V, and $I_{FIL}$ was 2.36 A, where the temperature was approximately 1800 K.

Figure 5-4 shows the beam profile dependence on the excitation of the offset CL, which represents its optical action. The CL was highly excited as $V_{CL}$ was decreased from +540 V to −80 V. The EBs were collimated in advance by the TL by setting $V_{PE}$ at +540 V. Initially, the CL was turned off by setting $V_{CL}$ at the identical voltage of +540 V. As $V_{CL}$ was changed from +540 V to 0 V, the EBs were deflected into the –X direction (downward in Fig. 5-4). This corresponds to the direction of the offset of the CL, which means the direction of the center axis of the CL from the optical axis. The beam profile was enlarged at 0 V because the beam was not focused on the detector plane. The direction of deflection of the EBs changed at −50 V, and then EB moved back to the +X direction (upward) from −50 V to −60 V. The negative polarity of $V_{CL}$ means that the voltage of CL was lower than that of the emitter, which suggests that the CL was highly excited. At $V_{CL}$ of −69.5 V, the beam position was close to the initial position, and the beam size reached a minimum. The optics operates around this condition. At $V_{CL}$ of −80 V, the beam position moved to the upper side compared to the initial position, which means that the beam was deflected across the optical axis twice. The beam width became large again.

The results in Fig. 5-4 confirm that the offset CL serves not only as the lens but also as the deflector in the X direction, which can generate the energy dispersion. In the opposite Y direction, which is the horizontal direction in Fig. 5-4, the beam position and size did not change as the excitation of the CL was varied. This result means that the CL exhibited either a very weak or no lens action in the Y direction, where the rectangular openings of the CL electrodes have longer sides. The ray-trace simulation for charged particles supports these results. We note that the beam profiles showed striped patterns because of the grid, which was located in front of the detector.

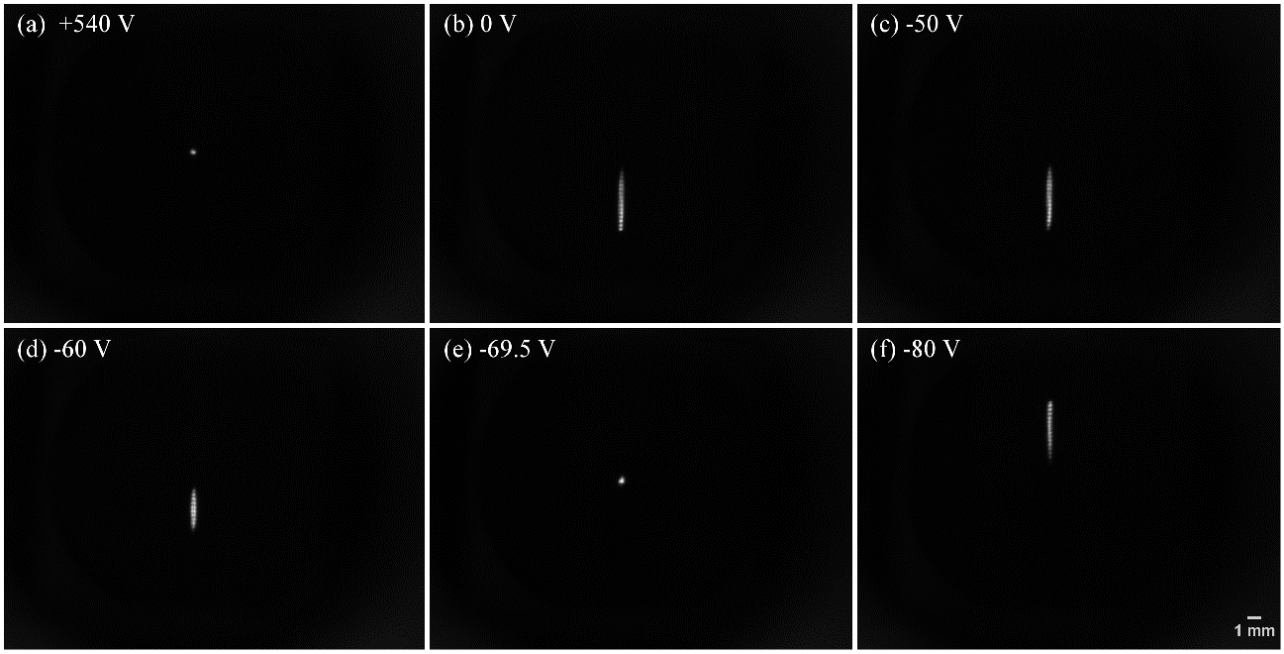


Fig. 5-4 Beam profile dependence on the excitation of the offset CL through changing $V_{CL}$ from +540 V to −80 V.

Next, the evaluation results on the TL is discussed. Adoption of the TL on the upstream side of the CL is a novel feature of the optics. The TL is a bi-potential lens with a deceleration mode. Figure 5-5 shows the beam profile dependence on the excitation of the TL.

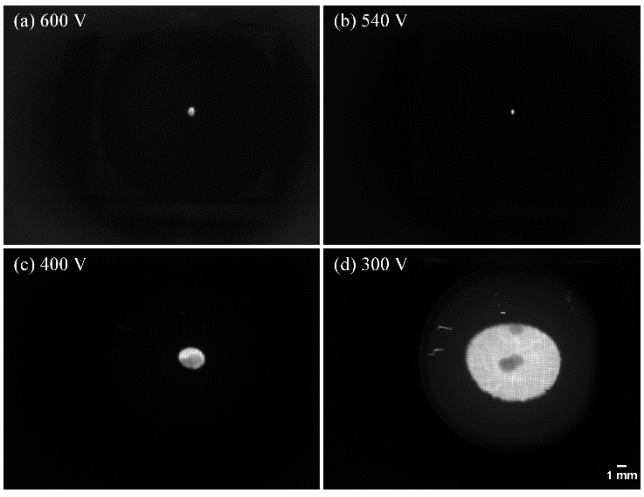


Fig. 5-5 Beam profile dependence on the excitation of the TL with decreasing $V_{PE}$ from 600 V to 300 V.

The EB entered the TL with a beam energy of 3.1 keV. As the TL was excited highly by decreasing $V_{PE}$, an optical mode of the EBs changed as follows: the EBs were divergent at 600 V, collimated at 540 V, and then converged.

Further changing $V_{PE}$ from 400 V to 300 V, the crossover position of the EB moved to the upstream side and the beam region was enlarged on the detector plane. The edges of the beam patterns were limited in part by the IN-AP.

The beam patterns showed symmetric distributions and the center positions remained constant for various $V_{PE}$. This suggests that the TL is the axially symmetric lens and the center of the TL is coincident with the optical axis. The ray-trace simulation for the charged particles supports these results. The large beam size condition at $V_{PE}$ of 300 V can be used just after installing the ES-AP, where a projected slit pattern of the ES-AP results in an easy adjustment. This optical component mainly operates in the collimated mode with $V_{PE}$ of 540 V for $V_{EXT}$ of 3.1 kV. The EBs are decelerated to 17% of the initial energy, which improves the energy resolution through increasing the energy dispersion. The collimation effect of the TL reduces the angular distribution of the incident EBs and suppresses the divergence of EBs in the Y direction, where the CL exhibits no focusing action. These further improve the energy resolution. We note that the dark circular regions on the beam patterns at $V_{PE}$ of 300 and 400 V were attributed to contamination on the grid and the several bright patterns in the outer regions were dark emissions from scratches on the SCR.

### 5-5-2 Energy resolutions

In this section, the energy resolving performance of the optics is evaluated. Here, we estimate the energy resolution of the optics by comparing the experimental and theoretical energy spreads of the SE. Mook et al. [1] adopted a similar method for evaluation of their MC.

Figure 5-6 shows a measured TED in a dotted plot. The TED was acquired for SE No. 1 at $V_{EXT}$ of 3.1 kV and $I_{FIL}$ of 2.26 A. The temperature corresponded to approximately 1700 K. In this condition, the emission current $I_{EMI}$ was 3.9 nA, which was much lower than conventional conditions of SEs. We adopted this condition of the SE so that the emission current was as small as possible to measure the TED. This allowed the additional contribution, $dE_{BOE}$, of the Boersch effect to the TED to be neglected. In the experimental set up of the optics, the diameter of the IN-AP was 30 μm and the width of the ES-AP was 12.5 μm in the X direction. The TED in Fig. 5-6 was acquired with the ACC scan mode, which means that the horizontal axis of the ACC voltage corresponded to the beam energy. The vertical axis was the normalized signal. Measurement conditions of the TED were as follows: the ACC voltage step was 20 meV, the step time was 2 sec, the number of steps in the scan was 300, and the total measuring time of the spectrum was 10 min.

The characteristics of the TED in Fig. 5-6 were expressed by four energy spread parameters; FWHM, FW50,

rising edge (RE), and falling edge (FE). FWHM and FW50 were described in section 5-3. Table 5-1 summarizes the FWHM and FW50 for the TED in Fig. 5-6. The RE refers to the energy width for the signals from 25 to 75% on the low-energy side of the TED. The FE is defined similarly on the high-energy side. In Fig. 5-6, RE and FE were 78 and 281 meV, respectively. The large difference between RE and FE meant that the TED was highly asymmetric. This trend was consistent with a previous study by Kim et al. [4]. The authors showed an asymmetric TED for an SE in a low current condition using an HSA with a theoretical energy resolution of 55 meV. As shown in Fig. 5-6, the optics can similarly resolve the sharp RE at the low energy side of the TED with the HSA.

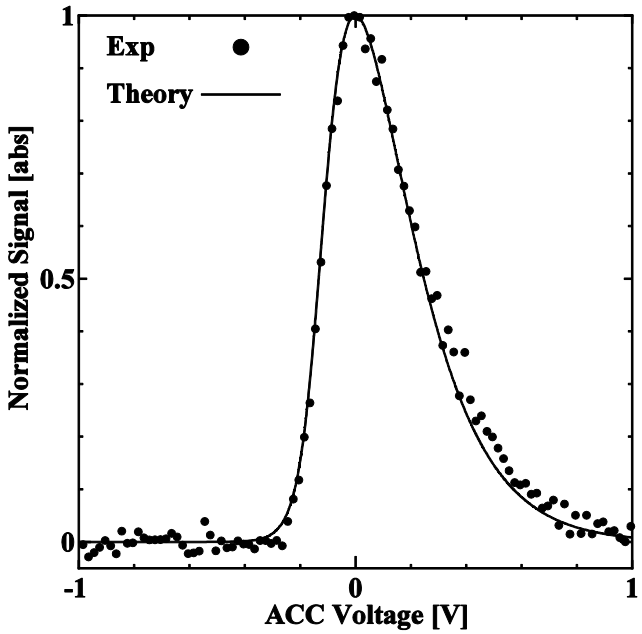


Fig. 5-6 Total energy distribution for SE No. 1 at 1700 K from experiment and theory.

Table 5-1 FWHM and FW50 energy spread from experiment and theory.

| | | FWHM<br>meV | FW50<br>meV |
|---|---|---|---|
| Experiment | $dE_{EXP}$ | 386 | 285 |
| Theory | $dE_{INT}$ | 380 | 262 |

Next, we derive the theoretical TED based on Eq. (5-2). Fig. 5-6 shows the TED obtained from theory by the solid line. Here, $T$ and $V_{EXT}$ were adopted from the experimental conditions, and the work function $W$ was 2.9 eV based on the reference [5]. The tip field factor $\beta$ was $9.9 \times 10^4$, which was determined by the gradient of the measured Schottky plot. Fig. 5-6 shows that the two plots with experiment and theory are coincident. Table 5-1 summarizes

the theoretical $dE_{INT}$ in the forms of the FWHM and FW50. We derived the energy resolution $dE_{RES}$ of the optics using the results in Table 5-1 based on Eq. (5-3). We confirmed that $dE_{BOE}$ was negligible from the empirical equation of previous studies [5, 7]. With the assumption that $dE$ is the FWHM and $\gamma$ is 2, the energy resolution $dE_{RES\_FWHM}$ is 88 meV. With the assumption that $dE$ is the FW50 and $\gamma$ is 1.652, the energy resolution $dE_{RES\_FW50}$ is 75 meV.

To verify the validity of the above results, we estimated the energy resolution of the MC by charged particle simulation. The chapters 2 and 3 have described the method and results in detail. Similarly, we executed a simulation with optical geometry and conditions in the current experimental setup. The energy resolution in FWHM is given by

$$dE_{RES\_FWHM\_Sim} = x/D_{\kappa}. \tag{5-4}$$

Here, $x$ is the larger of the beam diameter and the slit width of the ES-AP and $D_{\kappa}$ is the energy dispersion at the energy selection plane. We notice that Eq. (5-4) gives an energy resolution in FWHM. In the previous chapters, the energy resolution was defined as double the value at which beams were completely separated. Based on the simulation, the energy dispersion $D_{\kappa}$ was 147 μm/eV and the beam diameter was 1.3 μm at the beam energy of 540 eV. In the current experimental setup, the slit width of the ES-AP was 12.5 μm, which is a dominant factor for $x$. Based on Eq. (5-4), the energy resolution was 85 meV from the charged particle simulation. This was consistent with the experimentally estimated value of 88 meV, which confirms the evaluation result.

In the previous chapters, the energy dispersion $D_{\kappa}$ was 23.5 μm/eV for a beam energy of 4 keV. In the current condition, the dispersion was 6.3 times larger. This is attributed to the optical geometry using the TL, which is a bi-potential lens located upstream of the CL. Adoption of the TL enables a reduction of the beam energy and increases the energy dispersion, which results in an improvement of the energy resolution. In the current experimental setup, the slit width was a limiting factor of the energy resolution. If the slit could be optimized so that its width is identical to the beam diameter, the expected energy resolution is 9.6 meV from Eq. (5-4). This result means that there is sufficient room for further improvement.

### 5-5-3 Accuracy and stability of the entire system

In this section, the performance of the entire measuring system is evaluated. Figure 5-7 shows the TED measurements in the CL scan mode with various ACC offset voltages. By setting different voltages of $V_{ACC}$ in fine steps, the energy spectra with various mean pass energies are available based on Eq. (5-1). Here, SE No. 1 was

adopted with $V_{EXT}$ of 3.1 kV and $I_{FIL}$ of 2.36 A, where the temperature was approximately 1800 K. Fig. 5-7(a) shows three TED spectra with energy variations of 0 and ± 3 meV. The CL* voltage in the horizontal axis is the converted value through subtraction of the reference voltage of −71.5 V from $V_{CL}$ and inversion of the polarity. This provides the proper expression as the polarity of the energy, which means that the higher energy is shown on the right side. The inserted figure shows the magnified plots around signal levels of 50%. Dots and lines represent measured data and linear fittings, respectively. The three plots shifted according to the energy deviations without overlap, which meant that this system exhibits a sensitivity to detect an energy difference of 3 meV. In a similar way, TEDs were measured under seven conditions with energy variations of 0, and ± 1, 3, 5 meV. In each condition, TEDs were acquired five times, and the CL* voltage was estimated at 50% of the signal levels for each spectrum. Changes of the CL* voltages were calculated by the subtraction of a reference from measured values. Here, the referenced CL* voltage was −0.135 V at the energy variation of 0 meV. Fig. 5-7(b) shows the dependence of the CL* voltage at 50% of the signal on the energy variations. Here, dots and error bars represent the average values and standard deviations (±$\delta$), respectively, for five spectra in each condition.

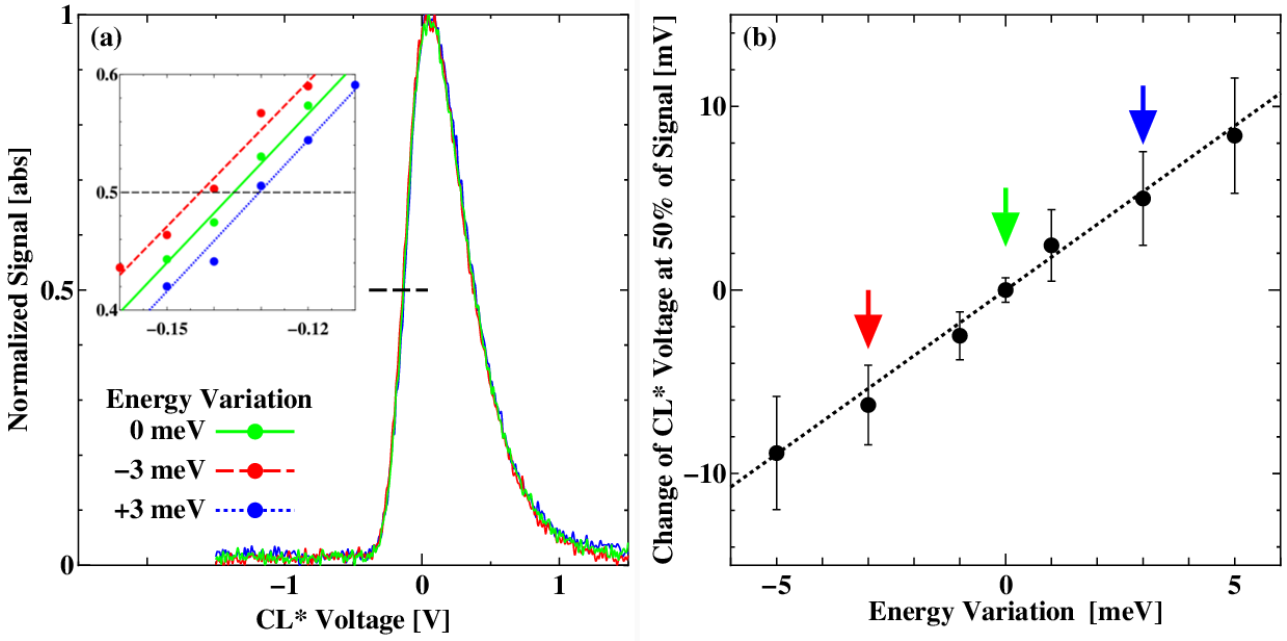


Fig. 5-7 TED measurement by the CL scan mode with various ACC offset voltages. (a) TED with energy variations of 0, and ± 3 meV. (b) Dependence of the CL* voltage at 50% of the signal on the energy variation. Arrows indicate the conditions corresponding to (a).

By consideration of the errors, Fig. 5-7(b) shows that the accuracy of the measurement was better than 3 meV. One TED measurement took 7.5 minutes and one condition needed approximately 38 min for the five measurements. Thus, the total evaluation period was 4.4 hours. The results in Fig. 5-7(b) also represent the stability of the measurement for the period. Therefore, this system has a very high performance in accuracy and stability. We clearly noticed that this result did not mean an evaluation of the energy resolution. However, this result implied the high potential of the measuring system with the new optics.

### 5-5-4 Operational conditions

Easy operation is an important factor for practical usage and application as an MC or EA. In this section, we will evaluate the operational conditions of the optics. By changing $V_{EXT}$ under fixed positions of the emitter and the ES-AP, two optical parameters, $V_{PE}$ and $V_{CL}$, were adjusted to achieve maximum signals on the measurement of TEDs. Figure 5-8 shows the dependence of $V_{PE}$ and $V_{CL}$ on $V_{EXT}$. These operational conditions of the optics showed a linear relationship. For their linear fittings, the multiple correlation factors, R2 values, were better than 99.999%. Table 5-2 summarizes the averages and errors of three ratios from the measured values of $V_{PE}$ and $V_{CL}$ for four $V_{EXT}$. Table 5-2 shows that a linear relationship was established with very high accuracy, where the errors were approximately 0.1%. This is because the optics adopted a pure electrostatic lens system without the use of a magnetic system, which usually exhibits hysteresis and nonlinear effects. In addition, the optics consists of mechanical components with high accuracy and electronics with high repeatability. In a practical application of the optics to the MC for EMs, the optimum setting of $V_{EXT}$ is different for each emitter because of the variation in the production process of the suppliers. In addition, the application of the EMs determines the condition. For example, EB inspection tools require higher beam currents to achieve high throughputs, where the higher $V_{EXT}$ condition is necessary. After the decision or adjustment of $V_{EXT}$, operators can use the MC through setting the operation conditions based on the ratios provided in Table 5-2. This MC can be used easily without a complicated adjustment procedure. MCs in previous studies adopted complicated aberration correctors and required complicated tuning procedures. The optics in this study have no difficulty in beam alignment because there are only two optical parameters, $V_{PE}$ and $V_{CL}$, and the relationship is well established. This is an advantage of the new optics with a simple structure. The MC/EA using the optics is suitable for practical application.

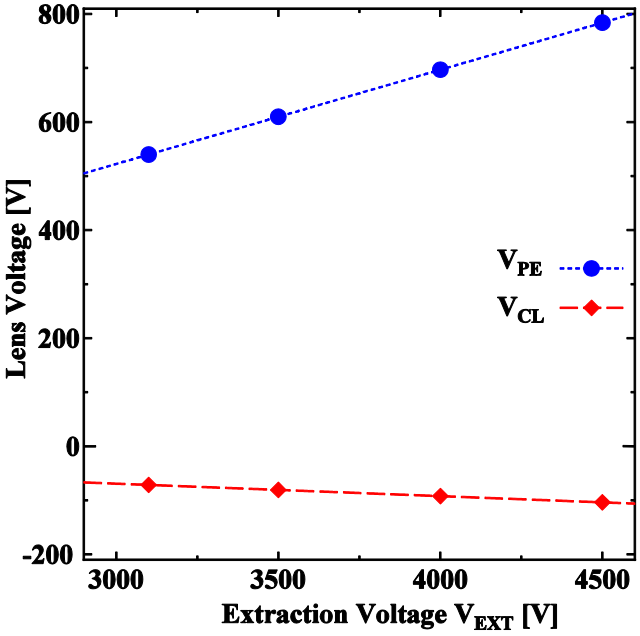


Fig. 5-8 PE and CL voltage dependences on extraction voltage.

Table 5-2 Operational conditions of the MC in voltage ratios.

| | PE/EXT | CL/EXT | CL/PE |
|---|---|---|---|
| AVG | 0.1742 | −0.0231 | −0.1323 |
| Error % | 0.05 | 0.12 | −0.10 |

### 5-5-5 Energy analysis for Schottky emitters in various conditions

In this section, we will show the application of the MC/EA to SEs in various conditions through measuring the TEDs. Figure 5-9 shows the TEDs for SE No. 1 and 2, where the extraction electric fields were different because of the geometries of these EXT electrodes. The measurements shown in Fig. 5-9 were obtained in the ACC scan mode, where the horizontal axis of the ACC voltage corresponds to the beam energy. The two peak positions were adjusted through a slight shift in the horizontal axis. For the operation conditions of both emitters, $V_{EXT}$ was 3.1 kV, and $I_{FIL}$ was set to achieve emitter temperatures of 1800 K. Table 5-3 summarizes the three energy spread parameters, that is, FWHM, RE, and FE, together with the emission current $I_{EMI}$. These parameters were averaged values of five measurements of the TED. The emission current of SE No. 2 was approximately 3000 times higher than that of SE No. 1. From Table 5-3, the FWHM of SE No. 2 was larger than that of SE No. 1. Fig. 5-9 reveals that this difference was mainly on the low energy side, where the TED for SE No. 1 increased sharply compared to that of SE No. 2.

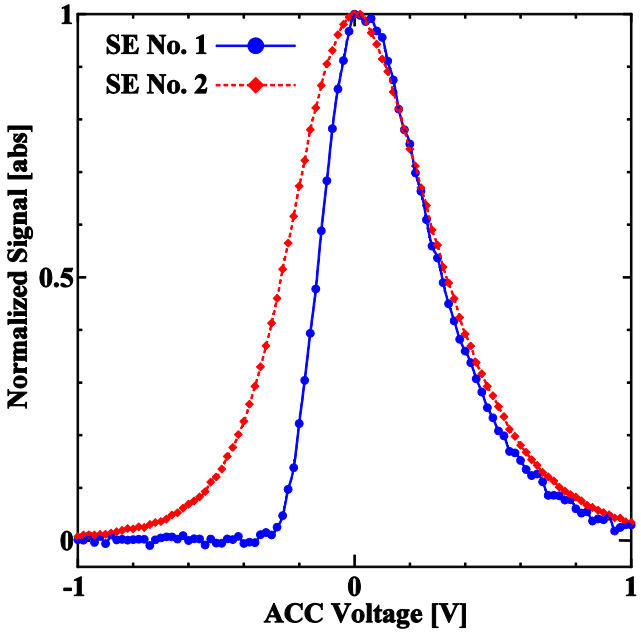


Fig. 5-9 Total energy distributions for SE No. 1 and 2.

Table 5-3 Energy spread parameters and emission currents for SE No. 1 and 2.

| Emitter | FWHM meV | RE meV | FE meV | $I_{EMI}$ μA |
|---|---|---|---|---|
| SE No. 1 | 449 | 108 | 287 | 0.047 |
| SE No. 2 | 599 | 217 | 325 | 144 |

For SE No. 1 with the lower EXT field, the TED was asymmetric. For SE No. 2 with the higher EXT field, the TED became more symmetric. The difference between RE and FE in Table 5-3 represents the degree of asymmetry of the TED for the two emitters more specifically. This result can be explained as follows; in the emission process of SEs, a higher EXT field narrows the width of the Schottky barrier at the interface between the emitter and vacuum, which increases the numbers of electrons tunneling through into the vacuum. Therefore, the RE of the TED in the low energy side becomes broad for the higher field condition. The parameter $q$ in Eq. (5-2e) shows the ratio of the tunneling process into the total emission. The estimated values of $q$ are 0.21 and 0.34 for No. 1 and 2, respectively, which shows the larger contribution of the tunneling process in SE No.2 than No 1. The result is consistent with prior studies of TEDs for SEs with various EXT fields using HSAs [3, 4]. The operational condition of SE No. 2 was considered as conventional conditions in their application to EMs. The FWHM was consistent with the widely accepted values of 600 meV for SEs, which guaranteed the results of the energy analysis with this optics.

Figure 5-10 shows energy spreads dependences on emission currents for SE No. 1 and 2. Here, the TEDs were

measured five times in each condition and averaged values of energy spreads in the FWHM were plotted in Fig. 5-9. The data of SE No. 2 in the highest current and SE No. 1 correspond to TEDs in Fig. 5-9. Here, both emitters operated at the temperatures of approximately 1800 K. The additional energy spreads of SE No. 2 were measured through changing the $I_{FIL}$ with temperature steps of 100 K. At the lowest $I_{EMI}$ of 0.2 μA, the FWHM was 481 meV. The energy spread increased monotonically as the $I_{EMI}$ increased, and then the inclination became smaller. This trend is consistent with a previous study of Sakawa et al. [9], considering differences in evaluation conditions, i.e. radiuses of emitters. This optics can detect the differences of 5-6 meV in energy spreads. These results show that the optics has sufficient performance in energy analysis of emitters in various operating conditions.

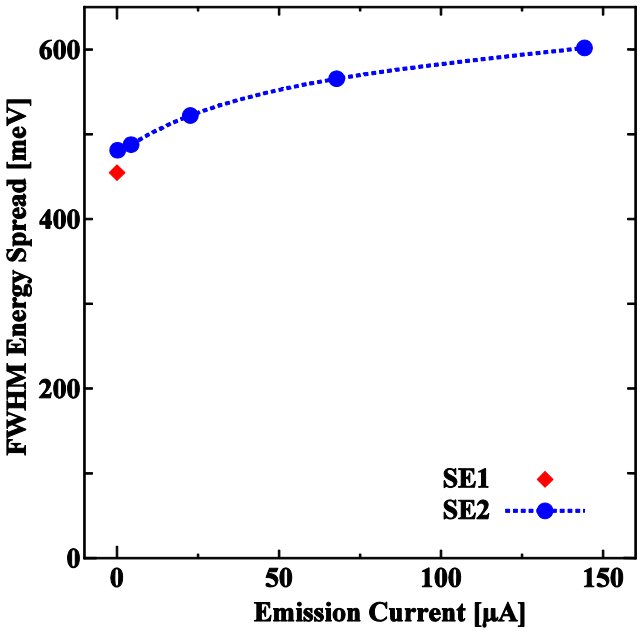


Fig. 5-10 Energy spreads dependences on emission currents for SE No. 1 and 2.

### 5-5-6 Features of the optics for the MC and EA

The MC using the optics in this study has the advantages of simple and robust structures compared to previous MCs; The Wien filter MCs [1, 11, 12] adopt multi-poles with electro-magnetic pieces, which are separated in azimuthal directions. The precise alignment of each piece is necessary. The electrostatic Omega MC [13] needs toroidal electrodes with different curvatures in the horizontal and vertical planes, which require a high level of machining techniques in three dimensions. The magnetic Alfa MC [14] has to control over 30 aberration corrector units, which requires a large number of electronics and sophisticated alignment procedures. The MC in this study is

a much simpler design because of the CLs, which are assemblies of flat electrodes with center openings. The alignment of CL electrodes is much easier than that of separated pieces of multipoles, and the machining of the flat electrodes of the CLs is easier than that of toroidal electrodes. The MCs with complicated aberration correctors need complicated correction procedures supported by software. We have no difficulty with beam alignment because there are only two optical parameters, $V_{PE}$ and $V_{CL}$, and their relationship is well established. This leads to another advantage of simple electronics with a small number of voltage sources. Through the evaluation, we can easily acquire TEDs just by setting specified voltages for the optics once the ES-AP position has been adjusted properly. The repeatability of the setting is excellent. The MC can be switched ON and OFF rapidly without hysteresis. These are attributed to the pure electrostatic optics. The magnetic optics exhibits hysteresis effects and the inhomogeneous magnetization of the magnetic poles. These are advantages of this MC compared to the previously reported MCs. In addition, the MC operates under the UHV condition of $1.3\times10^{-8}$ Pa. The SE with the MC keeps its operation for the period of over a half year without problems. We intentionally exchanged the emitter because we wished to evaluate another one. Therefore, the total lifetime of the SE is expected to be much longer. These results ensure the practical application of the MC for EMs in the future.

This optics can be applied to the EA. The offset CL of the optics is based on a similar operation principle as the EAs reported by Möllenstedt [15], which were used for TEM-EELS with high energy conditions. The energy resolutions were limited to several eV as Cundy et al. [16] reported. The vacuum conditions were also limited to a high vacuum. In this study, we showed that the offset CL could operate with the lower energy of 3.1 keV and better vacuum condition of $1.3\times10^{-8}$ Pa. The energy resolutions showed the much better value of 88 meV. In addition, we proved the combination of the TL with the CL results showed the following advantages. The EBs are collimated by the TL with the bi-potential lens, where a deceleration effect improves the energy resolution through increasing the energy dispersion. The collimation effect can suppress the divergence of EBs in the Y direction, where the CL has no focusing action. Furthermore, it can reduce the angular distribution of the incident EBs, which further improves the energy resolution, which is suggested from a previous study with simulation [17]. Our EA shows an advance and novelty compared to the previous studies on the Möllenstedt EAs.

In this study, we mainly showed the measurement results on TEDs from SEs. The EA could also be used for surface analysis similar to conventional methods if the target samples are located at the position of the emitter and additional EBs, ultraviolet, or x-ray sources are adopted. This EA can be used in a similar way with HSAs, which are the standard types used in surface science. Compared to HSAs, the compact size and linear optics of the EA provide

the benefits of easy integration into measurement instruments, which frequently have complicated designs that required installation of as many components as possible. Compared to RFAs, which are frequently adopted because of their simple structures, this EA has the advantage of being a band-pass filter type. RFAs are of high-pass filter types, which require differentiation of the signals to obtain the energy spectrum. This could amplify the noise and fluctuations of signals, which causes difficulties in analyzing small peaks or fine structures in the spectrum. Our EA of a band-pass filter type has no such difficulties related to differentiation and can provide more reliable data. This EA has the combined advantages of HSAs and RFAs.

## 5-6 Conclusion

The prototype of the MC has been manufactured in the test bench with a high mechanical accuracy at the micrometer level and has been combined with electronics with low noise and high stability. In this chapter, the first half of the MC, which mainly determines the energy resolving performance, was evaluated. The optics includes the offset CL and the TL. The optics can serve also as an EA. Through comparing TEDs from the experiment and theory, the energy resolution $dE$ is estimated to be 88 meV in FWHM and 75 meV in FW50 for the beam energy $E_0$ of 3.1 keV. The ratio $dE/E_0$, which is the index of performance, reaches $2.7 \times 10^{-5}$. Charged particle simulation results in an energy resolution of 85 meV in FWHM, which supports the experimental result. This also reveals that the limiting factor for the resolution is the width of the ES-AP, which suggests the possibility of further improvement down to 9.6 meV. As a total measurement system, the accuracy and stability are better than 3 meV. The optical conditions show a linear dependence with high accuracy. The energy resolving performance is sufficient to distinguish the variation of TEDs for different operational conditions of the SEs. The MC with the optics has the advantage of a simple and robust structure with the use of the CLs, compared to previous MCs that required complicated designs. The MC has high potential and is suitable for practical applications. The advantages of the EA using this optics are band-pass filtering type, linear optics, compact size, and easy integration into analytical systems.

## Reference

[1] H. Mook, P. Kruit, Ultramicroscopy 81 (2000) 129.

[2] R.D. Young, C.E. Kuyatt, Rev. Sci. Instrum. 39 (1968) 1477.

[3] M.J. Fransen, J.S. Faber, T.L. van Rooy, P.C. Tiemeijer, P. Kruit, J. Vac. Sci. Technol. B 16 (1998) 2063.

[4] H.S. Kim, M.L. Yu, E. Kratschmer, B.W. Hussey, M.G.R. Thomson, T.H.P. Chang, J. Vac. Sci. Technol. B 13 (1995) 2468.

[5] L.W. Swanson, G.A. Schwind, "*Handbook of Charged Particle Optics*", 2nd ed., edited by J. Orloff, (CRC Press, Boca Raton, 2008), Chap.1, 1.

[6] P.W. Hawkes, E. Kasper, "Principles of Electron Optics. Vol.2: Applied Geometrical Optics", (Academic Press, London, 1989).

[7] G.A. Schwind, G. Magera, L.W. Swanson, J. Vac. Sci. Technol. B 24 (2006) 2897.

[8] J. Barth, M. Nykerk, Nucl. Instruments Methods Phys. Res. A 427 (1999) 86.

[9] S. Sakawa, K. Tsunoda, Y. Terui, Surf. Interface Anal. 35 (2003) 11.

[10] H. Sakakibara, S. Nagai, K. Hata, T. Iwata, M. Okada, H. Mimura, Surf. Interface Anal. 44 (2012) 699.

[11] P.C. Tiemeijer, Ultramicroscopy 78 (1999) 53.

[12] M. Mukai, J.S. Kim, K. Omoto, H. Sawada, A. Kimura, A. Ikeda, J. Zhou, T. Kaneyama, N.P. Young, J.H. Warner, P.D. Nellist, A.I. Kirkland, Ultramicroscopy 140 (2014) 37.

[13] H. Rose, Ultramicroscopy 78 (1999) 13.

[14] O.L. Krivanek, J.P. Ursin, N.J. Bacon, G.J. Corbin, N. Dellby, P. Hrncirik, M.F. Murfitt, C.S. Own, Z.S. Szilagyi, Philos. Trans. A. Math. Phys. Eng. Sci. 367 (2009) 3683.

[15] G. Möllenstedt, Optik (Stuttg) 5 (1949) 499.

[16] S.L. Cundy, A.J.F. Metherell, M.J. Whelan, J. Sci. Instrum. 43 (1966) 71.

[17] R. Tian, M. Fink, Rev. Sci. Instrum. 58 (1987) 958.

# Chapter 6 Experimental Evaluation of the Monochromator with Offset Cylindrical Lenses

## 6-1 Introduction

In this chapter, the entire monochromator (MC) optics with offset cylindrical lenses (CLs) will be evaluated. The test bench of the prototype of the MC includes an additional retarding field energy analyzer (RFA) on the downside. The performance of the MC will be experimentally evaluated through measuring energy distributions and observing beam profiles. These results will assure that this MC has a high potential for its application to EMs.

## 6-2 Method

In this chapter, the entire MC optics is evaluated. The experiment setup is explained in section 5-2. The energy resolution of the MC is evaluated with method No. 2 in Fig 5-3. The narrowed energy width of the EBs with the MC is directly measured by the additional EA of the RFA type at the downside. The RFA consists of two electrodes (RFA-U and L) as shown in Fig. 5-1. The potential difference between $V_{PE}$ and $V_{RFA}$ forms a high-pass energy filter when $V_{RFA}$ is defined as a similar level with $V_{ACC}$. The voltage $V_{RFA}$ specifies a threshold energy for the EBs; some parts of EBs, which has the higher energy than the threshold, can pass through and the others with lower energy are repelled back to the upward. Fig. 5-1 describes this behavior of the main rays with dotted lines around the RFA. Scanning the voltage $V_{RFA}$ through measuring output signals $I_{SIG}$ of the detector gives integrated forms of energy spreads of the EBs and the numerical derivation process provides actual energy spectra.

## 6-3 Results and discussion

In this section, evaluation results on the MC prototype in the test bench are reported. First, the effect of two stages of the CLs was evaluated, which is an important feature of the optics of the MC. Beam profiles were observed at the detector with different conditions of the CLs. Here, the ES-AP was not installed, which enabled us to observe the beam profiles without limitation of the field of view. In addition, we adopted the IN-AP with a large diameter of 200 μm to show the optical action of the components more clearly. The evaluation adopts SE No. 1 with the following conditions; the voltage $V_{EXT}$ was 3.1 kV and the tip temperature was approximately 1800 K. The TL1 collimated the beam by setting $V_{PE}$ as 540 V. The CL was highly excited and adjusted so that the EBs were deflected back closer to

the optical axis. When CLs are turned on and off, the voltages $V_{CL}$ to CLs were −69.2 and 540 V, respectively. Detailed optical actions of the TL and CL have already been reported in chapter 5. Figure 6-1 shows beam profiles at the detector.

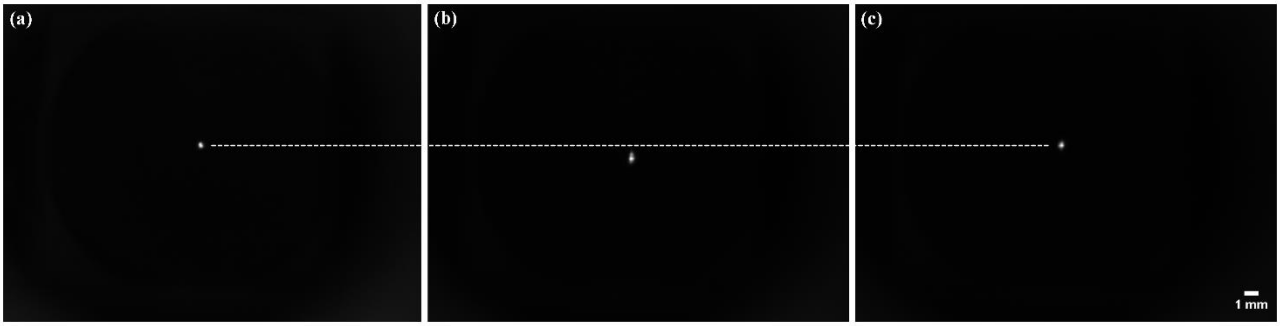


Fig. 6-1 Effects of two stages of CLs. Beam profiles are shown when (a) CL1 and 2 are turned off, (b) CL1 is on and CL2 is off, and (c) CL1 and 2 are on. The ES-AP is not installed.

In Fig. 6-1, the vertical and horizontal directions correspond to the X and Y directions in Figs. 2-1 and 5-1, respectively. In Fig. 6-1a, both of the CL1 and CL2 were turned off. The EBs took free motions and passed through the optics. This beam spot defines the reference position, which is shown as a white dot line. In Fig. 6-1b, the CL1 was turned on and the CL2 was off. The beam spot was located close to the reference but shifted on the downside. The direction corresponds to the opposite direction to the offset of the CLs. EBs were deflected once by the CL1 and the beam positions were shifted from the optical axis. In Fig. 6-1c, both of the CL1 and the CL2 were turned. The beam position was coincident with the reference. The EBs were deflected twice by the two CLs and moved back to the original axis. The two stages of the CLs realize the coincidence of the beam positions at the exit, which enable to switch ON/OFF of the MC without changing gun positions and aligning the beams to optics in the downside. This result is important for the MC considering its application to EMs because two operational modes, that is, a high-resolution mode with the MC and a high current mode without the MC, are available.

Next, the monochromatizing performance of the MC is evaluated. Here, the ES-AP with a width of 12.5 μm and the IN-AP with a diameter of 30 μm were installed. Positions of the ES-AP were adjusted to achieve the highest signals for each condition. The SE No. 2 was used with $V_{EXT}$ of 3.1 kV and the emission current $I_{EMI}$ of 176 μA. The MC was turned on when $V_{CL1}$ were −66.5 V and $V_{CL2}$ were −65.0 V. Under these conditions, energy distributions were measured with the RFA. Figure 6-2a and b show original and differential signals, respectively, when the MC

was turned on or off. In Fig. 6-2, both signals in the vertical axis were normalized and their peak positions were adjusted to be zero in the horizontal energy axis. The RFA provided the original signals as integrated forms of energy distributions in Fig. 6-2a. Therefore, the differential signals, which were acquired by a numerical method after smoothing the data, gave the energy distributions in Fig. 6-2b. When the case that the MC is turned on, Fig. 6-2a shows steeper decay and Fig. 6-2b does a narrower width. The results confirm that this new MC can reduce energy spreads of the EBs. In Fig. 6-2b, the data plot of the MC ON revels small peaks around the zero level in the lower energy side. These features were not reproducible for repeated measurements. It was caused by emphasized fluctuations or noises of the signals with the differentiation. Table 6-1 summarizes FWHM energy spreads. Here, the energy spectra were acquired five times and averaged (AVG) values and standard deviations (SD) were derived.

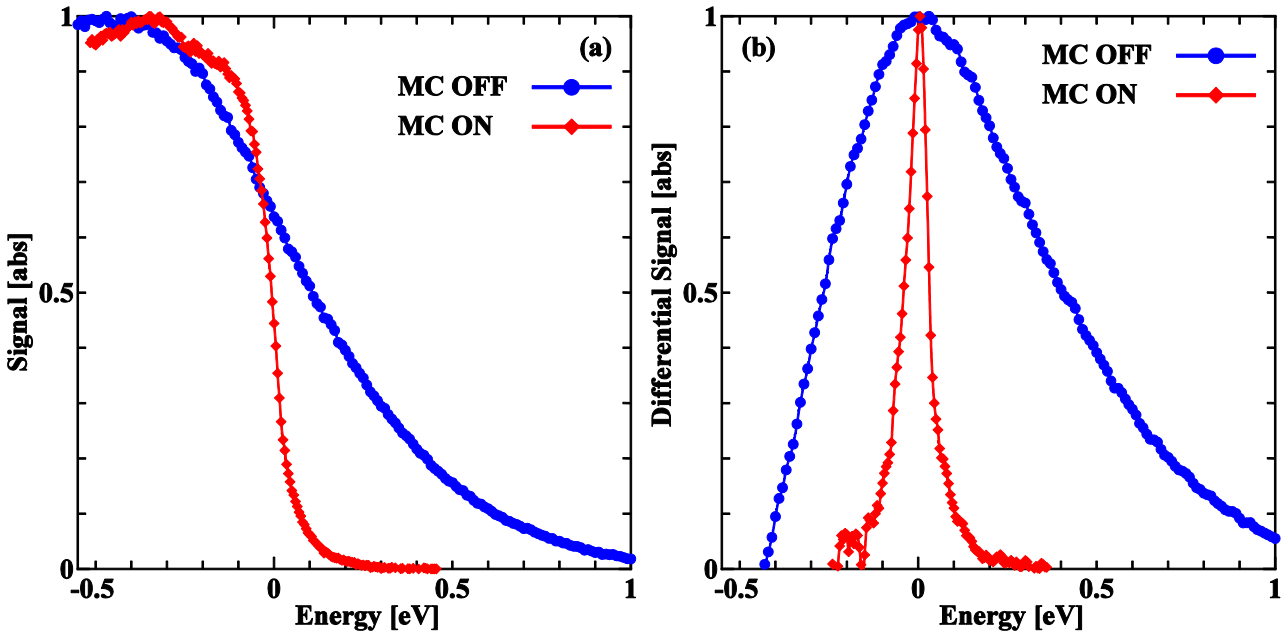


Fig. 6-2 (a) Original and (b) differential signals dependences on the beam energy when the MC is turned on or off.

Table 6-1 Energy spreads when the MC is ON and OFF.

| | Energy spread [meV] | |
|---|---|---|
| | AVG | SD |
| MC OFF | 676 | 13 |
| MC ON | 73 | 1 |

Table 6-1 shows that this MC achieves the FWHM energy resolution of 73 meV, which corresponds to 10% of the

native energy spread of the SE. The small values of the SD confirm high accuracy of the measurements. In chapter 5, the energy resolution of the MC was 88 meV, which was estimated by comparing energy distributions of the SE in the experiment and theory. In addition, the charged particle simulation provided the energy resolution of 85 meV. Both values are equivalent with the results in Table 6-1, which enhance the credibility on the measurement of the energy-resolving performance of the MC.

The exit current was larger than 100 pA for the condition of the MC ON at the experiments in Fig. 6-2 and Table 6-1, which were obtained with measuring the absorbed currents $I_{AP}$. The exiting current is sufficient to obtain microscopy images if the MC is integrated into EMs in future. The charged particle simulation suggests that the ES-AP with the width of 12.5 μm was a limiting factor of the energy resolution in the current experimental setup. If the slit could be reduced, the expected energy resolution of 9.6 meV can be achieved. This narrower slit could reduce the exiting current. However, considering that the measured value of the current is sufficiently high in this experiment, further improvement of the energy resolution is promising.

Next, beam profiles with the MCs are evaluated. This is important in applications of this MC to EMs. Figure 6-3 shows beam profiles when the MC is turned on or off. The images were obtained under the same condition as that of Fig. 6-2.

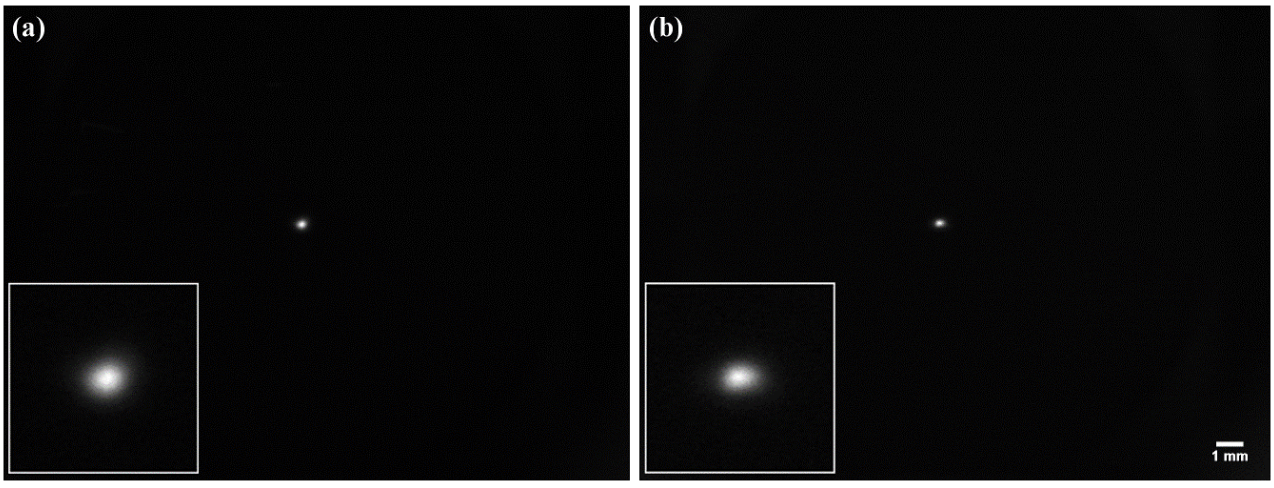


Fig. 6-3 Beam profiles for the MC (a) OFF and (b) ON.

Comparing Fig. 6-3a and b, two beam positions are coincident. In Fig. 6-3b, the beam profile with the MC ON shows a sufficiently symmetric shape and its slight distortion could be corrected with stigmators of the EMs. The beam size of the MC ON is equal to or smaller than that of MC OFF. These results suggest that the MC can achieve stigmatic

focusing with a unit magnification. In addition, the aberration of the MC is suppressed in lower levels. This is attributed to the symmetric geometry of the MC optics with respect to the middle plane. In chapter 2 and 3, theoretical studies with charged particle simulation show that the symmetry on the optics and main rays and the asymmetry on the paraxial rays can cancel the second order aperture aberration on the exit plane. This MC can achieve favorable beam profiles at the same beam positions in both cases where the MC is turned on or off. This guarantees high possibility of applications of the MC to EMs.

## 6-4 Future perspectives

In this section, future perspectives of the MC and its applications are discussed. In this study, the new MC with offset CLs has been developed, which corresponds to a feasibility study of the MC in a unit evaluation. In future, the MC will be integrated into electron microscopes. Figure 6-4 represents schematics of this study and future perspectives.

First, there is a plan to integrate the MC into an SEM. The MC achieved the energy spread of 73 meV with the SE. This is much better than typical energy spreads of 300 meV for cold field emitters (CFEs) [1]. The improvement in the beam performance at low energy conditions is expected for the SEM with adoption of the MC. In addition, SEs are much more stable and take a longer lifetime than CFEs. Daily routine operations such as flushing, adjustments of the EXT voltage, and calibration of the optics, are mandatory for CFEs [1]. This is not necessary for SEs. Operators would be freed from these daily operations and can focus on their works. The SEM with the MC can have such advantages. In semiconductor production, CD-SEMs, mask SEMs, and defect-review SEMs have become indispensable tools. The progress of nanoelectronic devices continuously requires the improvement of SEM performance at low energies. Additionally, these applications require high levels of robustness and stability for the equipment. The SEM with the MC is suitable for the industrial application field.

Next, the author has another idea of an instrument for academic research. Monochromatic EBs with lower energies is very useful for surface analysis of phonon or vibration spectroscopy similarly with HREELS instruments [2]. Recently, scanning near-field optical microscopy (SNOM) with a function of Fourier-transform infrared spectroscopy (FTIR) achieved real space imaging of surface phonon polaritons in h-BN [3] and measured the molecular vibration spectra of polymethyl methacrylate (PMMA) [4] with a spatial resolution of several tens of nm. The MC-STEM with high energy EBs at 60 keV was also able to reveal the phonon and vibration signals of specimens

[5-7]. However, considering the cross-sections of the phonon excitations and the knock-on beam damage, electron beams at extra-low energy levels of approximately 100 eV are favorable. For such applications, the author has a plan to develop a surface electron microscope with analytical functions, which integrates the MC and a high-resolution EA into an SEM in a UHV condition. The schematic on the right side of Fig. 6-4 presents the surface microscope. The microscope enables to study specimen surface with phonon and vibration spectroscopy in nanometer scales.

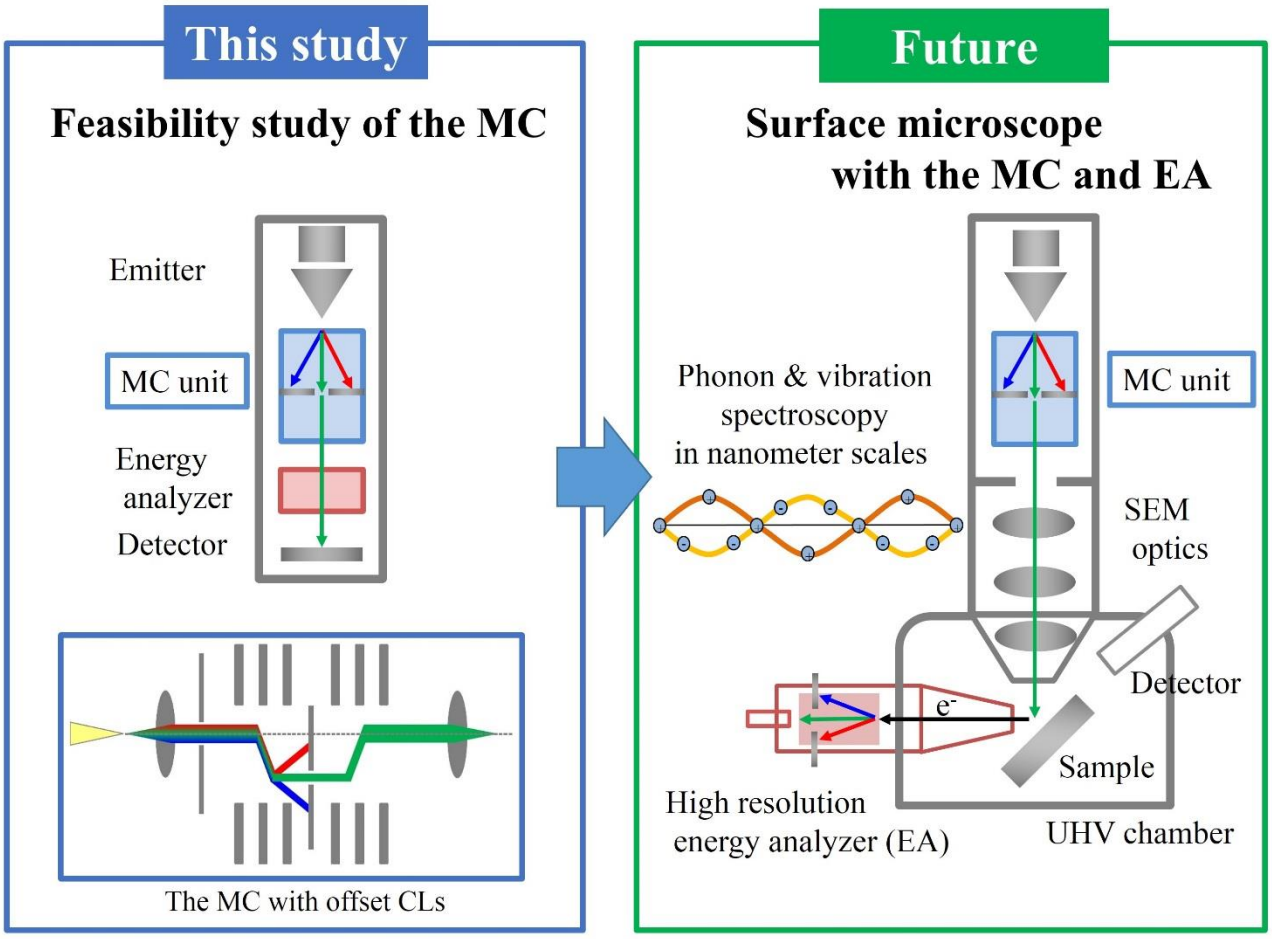


Fig. 6-4 Future perspectives.

A measurement with HREELS revealed edge phonon states of graphene nano-ribbons [8]. However, the signals were almost buried under other peaks. With the surface microscope, direct observation of the edge phonon states at specific positions would be possible. Similarly with the study with FTIR-SNOM [3], mapping of surface phonon polaritons of h-BN films would also be realized. This result could bring new knowledge on surface physics and nanoscience. In addition, gas-solid interactions are also an interesting research theme. Many studies with

HREELS reveal physics on absorption of the gases on solid surfaces [2]. Catalysis based on Au nanoparticles show size dependences on their activities in nanometer scale [9]. With the surface microscope, these nanoparticles can directly be observed with the microscope function and measure gas-adoption process with vibration spectroscopy. This would be useful to research and development of new catalytic agents. Furthermore, observation of bio and organic materials is an interesting theme. This is similar to studies using optical methods such as IR or Raman microscopy. However, higher spatial resolutions of nanometer levels are expected with the new surface microscope. In future, the author expects that new knowledge and insight could be acquired from phonon and vibration spectroscopy in nanoscale using the new surface microscope.

## 6-5 Conclusion

In this chapter, the entire MC optics including two CLs was evaluated. The test bench of the prototype of the MC includes the RFA on the downside. The performance of the MC was experimentally evaluated through measuring energy distributions and observing beam profiles. The MC achieves the energy resolution of 73 meV, which corresponds to 10 % of the original energy spread of the SE. The exit beam current is sufficiently large for its application to EMs. By comparing two conditions with and without the MC, the beams remain in the same positions and keep equivalent sizes and sufficient symmetry. These favorable results are achieved by the symmetric optical layout of the MC based on theoretical studies in the previous chapters. The evaluation results confirm that this MC has the high possibility on the application to EMs. This MC has another advantage in the simple structure, which results in high stability, robustness, and cost efficiency. Finally, future perspectives of the MC and its applications are discussed.

## Reference

[1] A.E. Vladár, M.T. Postek, "*Handbook of Charged Particle Optics"*, 2nd ed., edited by J. Orloff, (CRC Press, Boca Raton, 2009), Chap. 9, 437.

[2] H. Ibach, D.L. Mills, "*Electron Energy Loss Spectroscopy and Surface Vibrations*", (Academic Press, New York, 1982).

[3] S. Dai, Z. Fei, Q. Ma, A. S. Rodin, M. Wagner, A. S. McLeod, M. K. Liu, W. Gannett, W. Regan, K. Watanabe, T. Taniguchi, M. Thiemens, G. Dominguez, A. H. Castro Neto, A. Zettl, F. Keilmann, P.

Jarillo-Herrero, M. M. Fogler, and D. N. Basov, Science 343 (6175) (2014) 1125.

[4] F. Huth, A. Govyadinov, S. Amarie, W. Nuansing, F. Keilmann, and R. Hillenbrand, Nano Lett. 12 (8) (2012) 3973.

[5] O.L. Krivanek, T.C. Lovejoy, N. Dellby, T. Aoki, R.W. Carpenter, P. Rez, E. Soignard, J. Zhu, P.E. Batson, M.J. Lagos, R.F. Egerton, P. Crozier, Nature 514 (2014) 209.

[6] P. Rez, T. Aoki, K. March, D. Gur, O.L. Krivanek, N. Dellby, T.C. Lovejoy, S.G. Wolf, H. Cohen, Nat. Commun. 7 (2016) 10945.

[7] M.J. Lagos, A. Trügler, U. Hohenester, P.E. Batson, Nature 543 (2017) 529.

[8] T. Tanaka, A. Tajima, R. Moriizumi, M. Hosoda, R. Ohno, E. Rokuta, C. Oshima, S. Otani, Solid State Commun. 123 (2002) 33.

[9] M. Haruta, Chem. Rec. 3 (2003) 75.

# Conclusion

This doctoral dissertation summarizes the series of studies on the development of the new monochromator (MC) using offset cylindrical lenses (CLs) for electron microscopes (EMs) from theory to experimental evaluations. The summary of each chapter is described as follows:

In chapter 1, the background and main subject of this study were described. One of the recent trends of EMs is the observation in low energy conditions. For SEM, low energy conditions of several 100 eV were proposed for inspection of semiconductor devices with reduced interaction volumes of EBs inside the specimens. For (S)TEM, low energy conditions of 20-60 keV become essential for observation of light elements materials such as graphene without know-on damages on the specimens. The trend of low energy observation prompt advanced EMs to adopt MCs for improvement of spatial resolutions by reducing the influence of chromatic aberration. Furthermore, MCs can improve energy resolution in EELS and opened up new study fields. Therefore, the MCs are significant optical components for the advanced EMs. The technologies of MCs were explained through reviewing previous studies. MCs in previous studies achieved a high-performance level, but required complicated structures. Therefore, the main theme of this study is a development of a new MC with high performance and simple structure. SEM is considered as the application of the MC in this study because of the importance of industrial application. Considering that energy resolutions of MCs for SEM is 150 meV and that for LEEM is 100 meV in previous studies, the target of this study was specified as an energy resolution better than 100 meV. The main theme and objectives of this study were clarified.

In chapter 2, an optical axis and the first-order matrix expressions for a single offset CL are derived from various ray trace simulations. Based on the matrix expressions, a new MC with multiple offset CLs was constituted. The MC shows line focus and energy dispersions on the middle plane and takes a stigmatic and non-dispersive image of the emitter with unit magnification on the exit plane. The energy resolving performance and the mechanical tolerance of the MC were estimated.

In chapter 3, the aberration coefficients of the MC were derived up to the third order by applying a regression analysis to these trajectories. It is evident from the results that the second-order aperture aberration and lateral energy

dispersion are cancelled on the exit image plane. This is attributed to the symmetric optics and the optical axis, and to symmetric and asymmetric first-order trajectories. Based on the aberration coefficients, the dependencies of the MC performance, such as the beam width, energy resolution, and brightness, on the beam current were clarified. The energy resolution is limited by the second-order aperture aberration on the midplane, and the brightness is limited by the third-order aperture aberration on the exit plane. The MC performance was estimated for various source conditions, such as the types of emitters, the extraction voltages, and the tip radiuses. The optimum conditions of the MC are clarified for these conditions. The quantified characteristics are essential for the practical design of the MC and its application to microscopes.

In chapter 4, applications of the MC to an SEM at extra-low energies of less than 1 keV were investigated. Assuming the use of ideal and high-performance SEM optics with Cs and Cc values of 1 mm, FW50 beam diameters were calculated at the positions of specimens. Use of the MC improves dramatically the beam diameter to 4.4 nm, as compared to the diameter of 19.7 nm for the SEM without the MC, at a landing energy of 100 eV and a probe current of 1 pA. The contribution of the chromatic aberration becomes negligible because of the MC. The beneficial effects of the MC for the beam diameter become more prominent at lower landing energies ranging down to 10 eV. In addition, the effective current ranges of the MC expand at lower energies. Additionally, the SEM performance was surveyed under various emitter conditions, finding the optimum current ranges for the SEM with the sources. From the estimation, the author concludes that this MC can effectively improve the SEM performance in extra-low energy regions.

In two chapters, chapter 5 and 6, experimental evaluation results of the MC optics are presented. The MC prototype was designed in detail based on the theoretical studies. Then, the MC prototype has been manufactured in the test bench with a high mechanical accuracy at the micrometer level and been combined with electronics with low noise and high stability. The energy resolution of the MC prototype, which is one of the most important factors, is evaluated with two methods in chapter 5 and 6.

In chapter 5, the first half of the MC optics, which mainly determines the energy resolving performance, was evaluated. The electron optics includes the offset CL and the TL. The optics can serve also as an EA. Through comparing TEDs from the experiment and theory, the energy resolution $dE$ is estimated to be 88 meV in FWHM and

75 meV in FW50 for the beam energy $E_0$ of 3.1 keV. The ratio $dE/E_0$, which was the index of performance, reached $2.7 \times 10^{-5}$. Charged particle simulation showed an energy resolution of 85 meV in FWHM, which supported the experimental result. As a total measurement system, the accuracy and stability were better than 3 meV. The optical conditions showed a linear dependence with high accuracy. The energy resolving performance was sufficient to distinguish the variation of TEDs for different operational conditions of the SEs. The MC with the optics had the advantage of a simple and robust structure with the use of the CLs, compared to previous MCs that required complicated designs. The MC has high potential and is suitable for practical applications.

In chapter 6, the entire MC optics including two offset CLs was evaluated. The test bench of the prototype of the MC has included the RFA on the downside. The MC achieved the energy resolution of 73 meV, which corresponded to 10 % of the original energy spread of the SE. The exit beam current was sufficiently large for its application to EMs. By comparing two conditions with and without the MC, the beams remained in the same positions and kept equivalent sizes and sufficient symmetry. These favorable results are achieved by the symmetric optical layout of the MC based on theoretical studies. The evaluation results confirmed that this MC had the high possibility of the application to EMs.

As a summary of this study, the author has developed the new MC with high performance and simple structure through theory and experiment. The MC is based on the novel and original optics with CLs in offset layout. In the study, the application of this MC to SEM is mainly discussed. The measured energy resolution of the MC in this study is 73 meV, which is better than those of MCs for SEM and LEEM in previous studies. This MC shows preferable beam profiles and sizes, which is essential for its integration to EMs. The entire measuring system shows very high accuracy and stability better than 3 meV. The simple design of this MC reduces difficulties in the manufacturing of MCs in previous studies. This also realizes the MC with the minimized quantity of control units and easy calibration procedures. These are important, especially for industrial application. The evaluation results confirm that this MC has the high potential and possibility of the application to EMs. This study is related to charged particle optics (CPO), which is a branch of applied physics. The author believes that this study contributes to progress in CPO through revealing the MC optics with originality and novelty.

Finally, future perspectives of this study will be briefly described. The author has a plan to integrate the MC into an SEM to improve its performance at low enegy conditions. This would be beneficial for industrial applications.

The author also has another plan to develop a surface microscope combining this MC and a high-resolution energy analyzer. This could be useful for studies on the localized status of phonons and absorption process of the gases on solid surfaces and be applicable to the observation of bio and organic materials with high special resolutions. In future, the author expects that new knowledge and insight on physics related with phonon and vibration spectroscopy in nanoscale could be acquired using this instrument.

Historically, innovative instruments including CPO have achieved quantum leaps for science and technologies in various academic and industrial fields. Through the series of studies on instrumentation, the author hopes to contribute to progress in science and technologies.

# Acknowledgments

This doctoral dissertation is based on my research under the supervision of Professor Yoshizo Takai, Department of Material and Life Science, Graduate School of Engineering, Osaka University. I would like to express my gratitude to Prof. Takai for his support and encouragement to summarize this dissertation. The discussions with Prof. Takai are very informative and instructive especially on the evaluation of the MC.

I would like to deliver my gratefulness to Professor Heiji Watanabe and Professor Yasuo Kanematsu of Osaka University for the worthy comments and valuable guidance by reviewing the manuscript of this dissertation. It is very helpful to improve the quality of this dissertation through revising the manuscript based on their comments.

I would like to offer my special thanks to Dr. Boklae Cho of Korea Research Institute of Standards and Science (KRISS), who invited me to be a researcher there. Dr. Cho gave me great opportunity to begin successive studies on the MC even though it was expected to be very risky and difficult at the initial stage. Without his support, the studies in this dissertation would not have been possible.

I appreciate Drs. In-Yong Park and Sang Jung Ahn, the center heads of KRISS, for their understanding and supporting this project as a part of the center main project in KRISS.

I acknowledge Mr. Jyuhang Kim of KRISS for his technical support on the mechanical design of the MC. Based on my assembling drawings of the MC, Mr. Kim has completed the mechanical design. It was very helpful to materialize and construct the MC.

I would like to appreciate Professor Chuhei Oshima of Waseda University, who suggested and commented on applications of the MC to various research on the phonon or vibration spectroscopy. I had valuable experiences through learning surface science including various instruments such as energy analyzers while I studied at Prof. Oshima's laboratory as an undergraduate and master course student of Waseda University from 1999 to 2002. These experiences formed my background knowledge on the instrumentation.

I would like to express my grateful memory of Professor Takeo Ichinokawa of Waseda University, who deceased in 2015. He suggested an initial idea on an imaging energy filter using CLs when I studied at Waseda University in 2000. Prof. Ichinokawa gave me an opportunity to begin studying the charged particle optics. After completing the master degree, I decided to choose my career as a professional in this field.

I appreciate Drs. Tatsuya Adachi and Anto Yasaka of (former) SII Nanotechnologies, Inc. for their kind

support for my research activities after I left the company.

Finally, I would like to recognize my wife, son, and parents for their understanding during my studies.

# Publication list

## Original Articles with Peer Review

[1] "A new monochromator with multiple offset cylindrical lenses"
Takashi Ogawa and Boklae Cho
Nucl. Instrum. Methods A 772 (1) (2015) 5-13.

[2] "A new monochromator with multiple offset cylindrical lenses 2: Aberration analysis and its applications"
Takashi Ogawa and Boklae Cho
Nucl. Instrum. Methods A 800 (11) (2015) 18-28.

[3] "Low-energy scanning electron microscope using a monochromator with double-offset cylindrical lenses"
Takashi Ogawa, Boklae Cho, and Sang Jung Ahn
J. Vac. Sci. Technol. B 33 (6) (2015) 06FJ01.

[4] "Electron Optics with an offset cylindrical lens: Application to a monochromator or energy analyzer"
Takashi Ogawa and Yoshizo Takai
J. Vac. Sci. Technol. B 36 (3) (2018) 032902.

[5] "Evaluation of a monochromator with offset cylindrical lenses"
Takashi Ogawa et al. (in preparation).

---

[Supplemental publication]

[6] "Adsorption and desorption of benzene on Si (111)-7 × 7 studied by scanning tunneling microscopy"
Toyosei Kawasaki, Daisuke Sakai, Hiroshi Kishimoto, Ade Asneil Akbar, Takashi Ogawa, and Chuhei Oshima
Surf. Int. Anal. 31 (2) (2001) 126-130.

[7] "Double atomic layers of graphene/monolayer h-BN on Ni (111) studied by scanning tunneling microscopy and scanning tunneling spectroscopy"
Toyosei Kawasaki, Takashi Ichimura, Hiroshi Kishimoto, Ade Asneil Akbar, Takashi Ogawa, and Chuhei Oshima
Surf. Rev. Lett. 9 (3-4) (2002) 1459-1464.

[8] "Low-temperature field emission system for development of ultracoherent electron beams"
Boklae Cho, Takashi Ogawa, Takashi Ichimura, Takeo Ichinokawa, Takaaki Amakusa, and Chuhei Oshima
Rev. Sci. Instrum. 75 (10) (2004) 3091-3096.

[9] "Graphene-supporting films and low-voltage STEM in SEM toward imaging nano bio materials without staining: Observation of insulin amyloid fibrils"
Takashi Ogawa, Geun Won Gang, Minh Thu Thieu, Hyuksang Kwon, Sang Jung Ahn, Tai Wan Ha, and Boklae Cho
Micron 96 (2017) 65-71.

## Presentations at International Conferences

[1] "A Novel Monochromator with Double Cylindrical Lenses"

Takashi Ogawa, Boklae Cho, and Sang Jung Ahn
Microsc. Microanal. 21 (S4) (2015) 112-117.
Proc. of 9th International Conference on Charged Particle Optics (2014, Czech).

[2] "Fabrication of Nano-Slits for a Monochromator with Double Offset Cylindrical Lenses"
Takashi Ogawa, Geun Won Gang, In-Yong Park, Jyuhang Kim, Sang Jung Ahn, and Boklae Cho
Proc. of 15th Recent Trends in Charged Particle Optics and Surface Physics Instrumentation (2016, Czech) 42-43.

[3] "A New Monochromator for Electron Microscopy and Fabrication of Nano-Slits"
Takashi Ogawa, Geun Won Gang, In-Yong Park, Jyuhang Kim, Sang Jung Ahn, and Boklae Cho
Abstract of the 8th Japan-Korea Vacuum Nanoelectronics Symposium (2016, Japan) 24-25.

[4] "Development of a New Monochromator with Offset Cylindrical Lenses"
Takashi Ogawa
Abstract of the 9th Japan-Korea Vacuum Nanoelectronics Symposium (2017, Korea) 32-33.

## Presentations at Domestic Conferences

[1] "A Novel Monochromator with Double Cylindrical Lenses"
Takashi Ogawa and Boklae Cho
Proc. of the 71st Annual Meeting of the Japanese Society of Microscopy (2015, Japan) 168.

## Awards

[1] Excellence Award, Emergence Researcher 2015, Excellent Research Category, (No. 16-2-20), National Research Council of Science and Technology (NST) of Republic of Korea.

## Patents, granted

[1] US9425022, "Monochromator and Charged Particle Apparatus Including the Same"
Takashi Ogawa, Boklae Cho, Sang Jung Ahn, In-Young Park, and Cheolsu Han.

[2] JP5913682, "Monochromator and Charged Particle Apparatus Including the Same"
Takashi Ogawa, Boklae Cho, Sang Jung Ahn, In-Young Park, and Cheolsu Han.

[3] KR10-1633978, "Monochromator and Charged Particle Apparatus Including the Same"
Takashi Ogawa, Boklae Cho, Sang Jung Ahn, In-Young Park, and Cheolsu Han.

[4] KR10-1815850, "Monochromator and Charged Particle Beam Apparatus Comprising the same"
Takashi Ogawa, Kim Jyuhang, and In-Young Park.

[5] KR10-1773861, "Electron Beam Apparatus Comprising Monochromator"
Takashi Ogawa and Kim Jyuhang.

[6] KR10-1787379, "Production Method of Monochromator"
Takashi Ogawa and Kim Jyuhang.